UNIVERSITY OF CALIFORNIA
RIVERSIDE

# Hydraulic Fracturing in Transversely Isotropic Elastic Solids

A Dissertation submitted in partial satisfaction
of the requirements for the degree of

Doctor of Philosophy

in

Mechanical Engineering

by

Boshen Li

September 2023

Dissertation Committee:
Dr. Guanshui Xu, Chairperson
Dr. Bhargav Rallabandi
Dr. Kambiz Vafai

The Dissertation of Boshen Li is approved:

_____

_____

_____

Committee Chairperson

University of California, Riverside

# Acknowledgment

First of all, I would like to express my sincere gratitude to my research advisor, Professor Guanshui Xu, for his consistent guidance and encouragement during my PhD career. He not only provides continued support on my research project, but also helps me to build up my future career. His effort and enthusiasm for the research inspired me to become an outstanding scientist and engineer. I would also like to thank my dissertation committee, Professor Kambiz Vafai and Professor Bhargav Rallabandi for the time they spent reviewing my dissertation and serving as my committee members.

Furthermore, my thanks also go to my groupmates: Jun Du and Tianxiang Huang. In this long journey, we stood with each other and developed a close friendship which is the most valuable treasure in my life.

Last but not least, I am really grateful to my mother Xiaoming Wang and my father Wei Li. Your caring and love is the motivation for me to get through all the darkness. With your standing behind, I gain the confidence to complete my study and to achieve more goals in future.

ABSTRACT OF THE DISSERTATION

Hydraulic Fracturing in Transversely Isotropic Elastic Solids

by

Boshen Li

Doctor of Philosophy, Graduate Program in Mechanical Engineering
University of California, Riverside, September 2023
Dr. Guanshui Xu, Chairperson

Hydraulic fracturing (HF) is a widely employed technique for stimulating low-permeable underground reservoirs to enhance hydrocarbon production. Current HF models for the design of industrial HF treatments commonly assume fractures grow in an isotropic elastic solid. However, most sedimentary rocks, such as shales and mudstones, are made of fine-scale layers that should be treated as transversely isotropic (TI) solids. The impact of such anisotropy on HF treatments has not been fully addressed in current HF models for practical applications.

In this thesis, we focus on the study of vertical planar three-dimensional hydraulic fractures (PL3D) propagating perpendicular to the isotropic planes of various TI solids. The PL3D model is constructed based on the displacement discontinuity method (DDM) for fractures and the finite volume method (FVM) for fluid flow within fractures. The formula of the

stress field of a dislocation segment in a general anisotropic elastic solid is incorporated into DDM. As a consequence, we find the horizontal extension of fracture is greater than the vertical extension in TI solids. This elongation is more obvious for a solid with stronger anisotropy. The fracture energy is another important factor that can also have a significant impact on fracture geometry. These effects, influenced by various elastic parameters, are delineated and presented in quantitative detail. Finally, we demonstrate that approximate methods may be used to address the transversely isotropic effects in isotropic models for computational efficiency.

# Contents

# List of Figures

# List of Tables

# Chapter 1

## Introduction

### 1.1 Hydraulic fracturing

Hydraulic fracturing (HF) [1], commonly known as fracking, is a method of extracting oil and gas from shale and other unconventional reservoirs by injecting a high-pressure mixture of water, sand, and chemicals into the rock formation to create fractures or cracks (Figure 1.1). Hydraulic fracturing can both increase production rates and increase the total amount of gas that can be recovered from a given volume of shale. Pump pressure causes the rock to fracture, and water carries sand ("proppant") [2] into the hydraulic fracture to prop it open allowing the flow of gas.

The history of the fracturing can be traced to the 1860s, when liquid nitroglycerin (NG) was used to stimulate shallow, hard rock wells in Pennsylvania, New York, Kentucky, and West Virginia. In the 1950s, the first hydraulic fracturing was performed in Kansas by Stanolind Oil [3]. At the early stage, the HF project contains the traditional set of exploration and production practices where vertical drilling to strike oil reservoirs in high

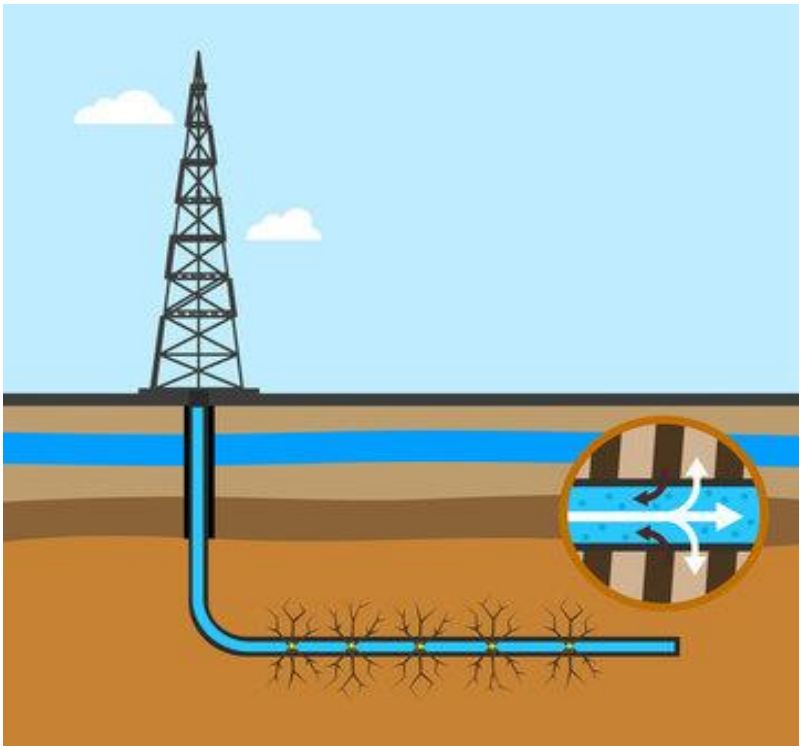

Figure 1.1: Schematics of the hydraulic fracturing project.
(Picture taken from gasbrasmg.com.br)

porosity formations at the depth of 4 to 5 kms underground (conventional reservoirs). It is the so-called conventional hydraulic fracturing technology which is still the dominant way in the petroleum industry nowadays providing almost all the petroleum sold in the global markets. In the mid 1990's, unconventional reservoirs [4-5] such as natural gas from coal and tight gas sands and carbonates were becoming more important as a supply of natural gas in North America. The transition towards unconventional gas reservoirs had begun and the importance of hydraulic fracturing was beginning to be realized by industry. The unconventional hydraulic fracturing [5-6] (Figure 1.1) was a major advancement in petroleum science and technology, as it expressed an innovative paradigm of production.

The technological breakthroughs were first realized in the Barnett shale gas play located in the Fort Worth Basin in Texas. With the application of horizontal drilling [7], this new technology has been developed to enable economic gas production from these "ultra" tight reservoirs which display a low rate of porosity and permeability compared with the conventional reservoirs. Also, the size of the fracture treatment as well as the number of treatments per well have steadily increased as a result of shale gas development. The development of unconventional hydraulic fracturing has allowed numerous unconventional reservoirs to yield increasing volumes of oil and gas. This achievement has enabled significant natural gas resources to be added to the country's energy base and extend the potential supply by over 100 years.

Over the past 50 years, there have been significant advances in hydraulic fracturing technology. Different types of fracture treatments have been developed ranging from packer [8] and pumping equipment to variations in treatment fluids and proppants [1]. Each natural reservoir is unique due to the variability in geology and geomechanics. As a result, there will be different types of hydraulic fracturing treatments used depending on what results are needed in the end and what the parameters of the zone are. In general, hydraulic fracturing still remains a relatively young technology in continuous improvement.

## 1.2 Transversely isotropic formations

Generally speaking, the rock formations exist in nature with various mechanical properties. In engineering projects, the rock mass is commonly considered as a continuous, homogeneous, isotropic medium. However, the real rock we explore in hydraulic fracturing

always exhibits more uncertainties such as anisotropy, heterogeneity and nonlinearity. Thus, more detailed treatment should be taken into consideration to capture the impact of the rock formations in this engineering application.

Figure 1.2: Shale Sedimentary rock in Finnmark, Norway. Width of sample 9 cm. (Picture downloaded from Sandatlas)

Transverse isotropy is a very common property in the sedimentary rocks which can be found in a variety of geological formations such as shale, sandstone and limestone. It is a direct result of the deposition and compaction processes [9] and occurs over a wide range of scales (metric to sub-metric). These rock materials are characterized by the presence of an intrinsic lamination in horizontal direction (Figure 1.2). Transversely isotropic rock in underground reservoirs exhibits a directional variation in its physical properties such as elasticity, conductivity and strength vertically [10]. Thus, the axis of material symmetry is

in vertical direction while the horizontal plane is considered as an isotropy plane (Figure 1.3). The anisotropic properties of sedimentary rocks can have significant implications for various geological and engineering applications. For example, in oil and gas exploration, the anisotropic properties of transversely isotropic rocks can affect the propagation of the fracture, flow of oil and gas through the rock and the effectiveness of hydraulic fracturing operations. Therefore, understanding the anisotropic properties of transversely isotropic rocks is important for accurately predicting their behavior and optimizing various geological and engineering applications [11].

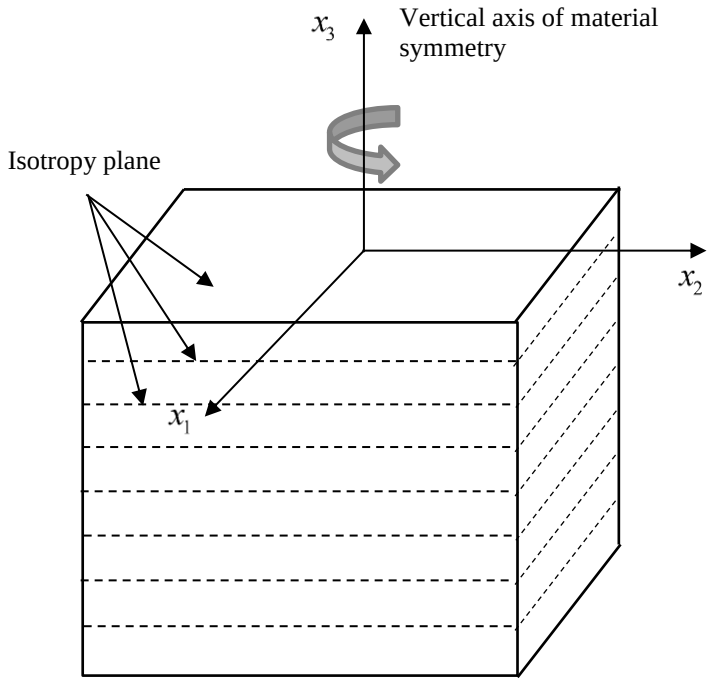


Figure 1.3: Schematics of the transversely isotropic formation

## 1.3 Modeling of the hydraulic fracturing

As hydraulic fracturing becomes an essential stimulation technique for oil and gas production, there has been great interest in understanding how hydraulic fractures grow in certain conditions. The modeling of hydraulic fracturing involves simulating and predicting the behavior of the fracture process using mathematical and computational models. These models can help engineers and scientists understand how fractures propagate, interact with the rock formation, and influence fluid flow within the reservoir.

The development of the first simplified theoretical HF model started in the 1950s. The ground-breaking paper in this area is proposed by Perkins and Kerns [12] using Sneddon's classic crack solution [13]. Later, Nordgren [14] improved this model by adding the fluid loss and formulated the PKN model (Figure 1.4a). The PKN model is applicable to long fracture of limited height and elliptical vertical cross-section. Another classic HF model was invented by Khristianovic and Zheltov [15], and by Greertsma and de Klerk [16] independently in 1955 and 1969, respectively. This is the so-called KGD model which is applicable to the fracture that has much longer fracture height than the length (Figure 1.4b). The radial or penny-shaped model with constant fluid pressure was solved by Sneddon [17]. This model is used for the circular fracture in homogenous reservoir conditions where fluid injection region is practically a point source and fracture plane is perpendicular to the minimum confining stress. These three classic HF models (PKN, KGD and penny-shaped) were used frequently in the 1990s. But they have been largely replaced by pseudo-3D model (P3D) and planar 3D model (PL3D) nowadays.

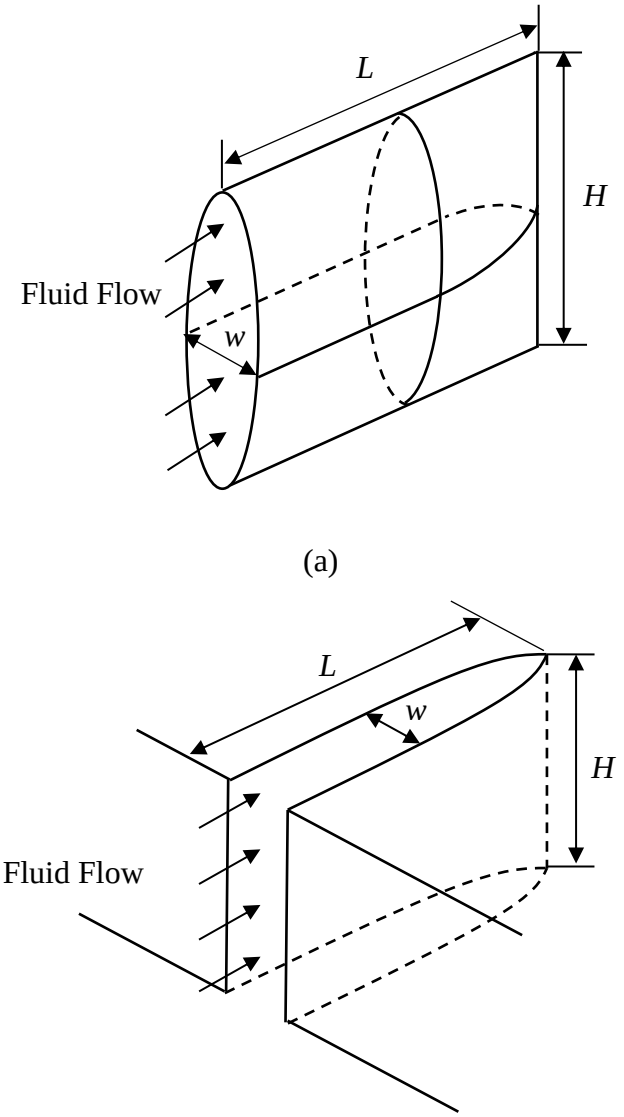


Figure 1.4: Schematic of KGD and PKN fracture geometries

P3D models were developed from PKN model in 1980s by allowing the fracture height to vary in time and space to capture the behavior of the multiple layers. It was built on the basic assumption that the reservoir elastic properties are homogeneous and averaged over all layers containing the fracture height. There are two categories: cell-based and lumped

models [18]. In lumped model, the fracture consists of two half-elliptical shapes connected at the middle (Figure. 1.5). The fracture lengths for both ellipses are calculated at each time step. In the cell-based approach, the fracture length is sub-divided into a series of PKN-like cells, each with its own computed height (Figure 1.6). P3D models have become popular owing to their pre-fracture design and post-fracture analysis coupled with efficiency in computation and time requirements.

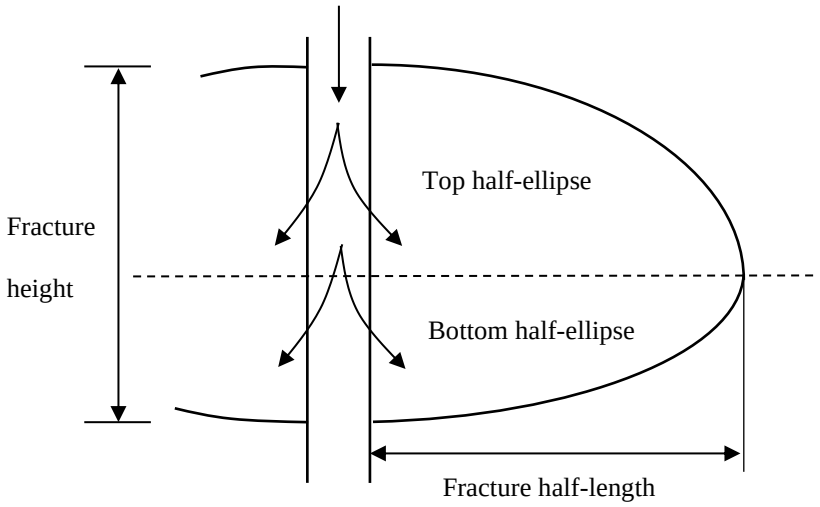


Figure 1.5: Schematics of pseudo 3D lumped elliptical model

The 1980-2000 period saw the development of planar 3D models [19-20]. These models solve the full 3D elastic rock deformation problem coupled with a 2D viscous fluid flow equation. (a more detailed solution is given in **Chapter 3**). Although these generations of PL3D provide the most comprehensive capabilities for hydraulic analysis and design, they require excessive central processing unit resources and lack the ease of operation required for practical use.

To describe the fracture twist, Carter et al. [21] proposed a fully 3D model. The fully 3D model is time-consuming even with today's powerful computational resources. Xu et al. [22] developed a nonplanar multi-fracture simulator, called "FrackOptima," in which the multi-fracture is assumed vertical 3D. The commercial application of fully 3D model is still unreported since the computational burden is extremely heavy and the unresolved physical questions about the propagation of fully 3D fractures.

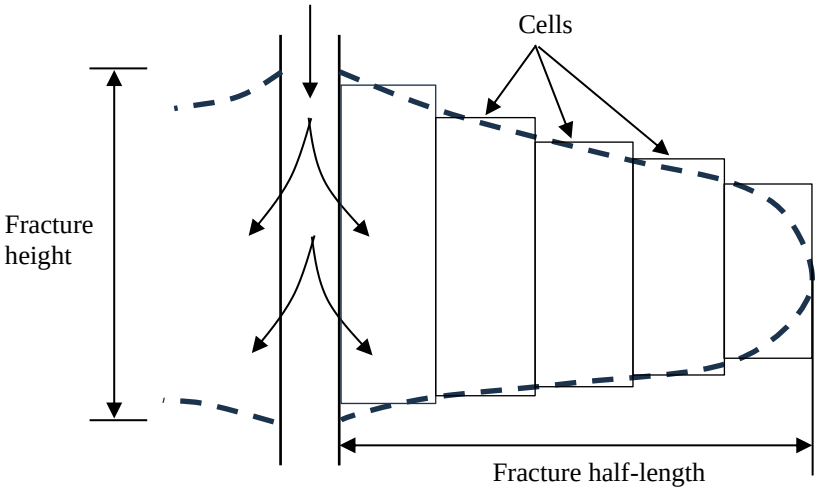


Figure 1.6: Schematics of pseudo 3D cell-based model

# Chapter 2

## Elasticity and dislocation theory

### 2.1 Anisotropic material

Anisotropic materials are substances that exhibit different physical properties when measured along different axes or directions. In most crystalline materials, the elastic properties are dependent on specific directions as a result of unique atomic arrangement. Under the most general conditions, the constitutive relation of a crystal undergoing elastic deformation can be expressed in the form:

$$\sigma_{ij} = C_{ijkl}\varepsilon_{kl} \tag{2.1}$$

In Eq. (2.1), the fourth-order elastic tensor $C_{ijkl}$ has 81 independent components. However, most of these components are redundant, as is shown in the following arguments. For general anisotropic materials, both stress and strain tensors are symmetric

$$\sigma_{ij} = \sigma_{ji}; \quad \varepsilon_{ij} = \varepsilon_{ji} \tag{2.2}$$

Hence one can write

$$C_{ijkl} = C_{jikl} = C_{ijlk} \tag{2.3}$$

This symmetry leaves only 36 independent components of $C_{ijkl}$. Moreover, assuming that there exists a strain energy from which the stress can be derived as

$$\sigma_{ij} = \frac{\partial U}{\partial \varepsilon_{ij}} \tag{2.4}$$

Combining this with Eq, (2.1), we can get

$$C_{ijkl} = \frac{\partial^2 U}{\partial \varepsilon_{ij} \partial \varepsilon_{kl}} = \frac{\partial^2 U}{\partial \varepsilon_{kl} \partial \varepsilon_{ij}} = C_{klji} \tag{2.5}$$

We can conclude that the index symmetry of $C_{ijkl} = C_{klij}$ results in only 21 independent components. This most general condition is applicable to *triclinic material*. Serval special cases will be outlined next. Let us adopt a simpler notation here

$$\{\sigma\}^T = [\sigma_1, \sigma_2, \sigma_3, \sigma_4, \sigma_5, \sigma_6] = [\sigma_{11}, \sigma_{22}, \sigma_{33}, \sigma_{23}, \sigma_{13}, \sigma_{12}] \tag{2.6}$$

$$\{\varepsilon\}^T = [\varepsilon_1, \varepsilon_2, \varepsilon_3, \varepsilon_4, \varepsilon_5, \varepsilon_6] = [\varepsilon_{11}, \varepsilon_{22}, \varepsilon_{33}, 2\varepsilon_{23}, 2\varepsilon_{13}, 2\varepsilon_{12}] \tag{2.7}$$

The general constitutive elasticity relationship $\sigma_{ij} = C_{ijkl}\varepsilon_{kl}$ can be rewritten as

$$\begin{Bmatrix} \sigma_1 \\ \sigma_2 \\ \sigma_3 \\ \sigma_4 \\ \sigma_5 \\ \sigma_6 \end{Bmatrix} = \begin{bmatrix} C_{11} & C_{12} & C_{13} & C_{14} & C_{15} & C_{16} \\ C_{21} & C_{22} & C_{23} & C_{24} & C_{25} & C_{26} \\ C_{31} & C_{32} & C_{33} & C_{34} & C_{35} & C_{36} \\ C_{41} & C_{42} & C_{43} & C_{44} & C_{45} & C_{46} \\ C_{51} & C_{52} & C_{53} & C_{54} & C_{55} & C_{56} \\ C_{61} & C_{62} & C_{63} & C_{64} & C_{65} & C_{66} \end{bmatrix} \begin{Bmatrix} \varepsilon_1 \\ \varepsilon_2 \\ \varepsilon_3 \\ \varepsilon_4 \\ \varepsilon_5 \\ \varepsilon_6 \end{Bmatrix} \tag{2.8}$$

In the following, we discuss the special cases of symmetry that are usually encountered in anisotropic materials:

**Orthotropic Materials**

If three mutually orthogonal planes of symmetry exist, the material is said to be orthotropic, which leaves 9 independent components of $C_{ijkl}$ . Wood is a common example of orthotropic materials. Thus,

$$C = \begin{bmatrix} C_{11} & C_{12} & C_{13} & 0 & 0 & 0 \\ C_{12} & C_{22} & C_{23} & 0 & 0 & 0 \\ C_{13} & C_{23} & C_{33} & 0 & 0 & 0 \\ 0 & 0 & 0 & C_{44} & 0 & 0 \\ 0 & 0 & 0 & 0 & C_{55} & 0 \\ 0 & 0 & 0 & 0 & 0 & C_{66} \end{bmatrix} \tag{2.9}$$

**Transversely Isotropic Materials**

If an orthotropic solid exhibits symmetry with respect to arbitrary rotations about one of the axes, it is then called transversely isotropic, which reduces independent components of $C_{ijkl}$ to only 5. For example, let $x_3$ be the symmetric axis and plane $(x_1 - x_2)$ as the isotropic plane (Figure 1.3):

$$C = \begin{bmatrix} C_{11} & C_{12} & C_{13} & 0 & 0 & 0 \\ C_{12} & C_{11} & C_{13} & 0 & 0 & 0 \\ C_{13} & C_{13} & C_{33} & 0 & 0 & 0 \\ 0 & 0 & 0 & C_{44} & 0 & 0 \\ 0 & 0 & 0 & 0 & C_{44} & 0 \\ 0 & 0 & 0 & 0 & 0 & C_{66} \end{bmatrix} \tag{2.10}$$

with $C_{66} = \frac{1}{2}(C_{11} - C_{12})$. Also, for certain special materials, the anisotropic coefficients may be expressed in terms of engineering coefficients such as Young's moduli, shear

moduli and Poisson's ratio. For example, transversely isotropic materials are characterized by five material coefficients: horizontal and vertical Young's moduli and Poisson's ratios $E_1, E_3, \nu_1, \nu_3$ and vertical shear modulus $G_3$. where subscripts stand for the direction of each parameter. The relationships between them and elastic constants are [23].

$$C_{11} = \frac{\left(1 - n\,\nu_3^2\right) E_1}{AB} \qquad C_{12} = \frac{\left(\nu_1 + n\,\nu_3^2\right) E_1}{AB} \qquad C_{13} = \frac{\nu_3 E_1}{B}$$

$$C_{33} = \frac{\left(1 - \nu_1\right) E_3}{B} \qquad C_{44} = G_3 \tag{2.11}$$

$$A = 1 + \nu_1 \qquad B = 1 - \nu_1 - 2n\,\nu_3 \qquad n = E_1 / E_3$$

We introduce elastic constants for some TI materials [24] in Table 2.1. the anisotropy for the direct compression along $x_1$ and $x_3$ is computed using the ratio $C_{11}/C_{33}$ which varies from 1 for isotropic material.

Table 2.1: Example of elastic coefficients $C_{ij}$ for TI rocks (in GPa)

| Material | $C_{11}$ | $C_{33}$ | $C_{12}$ | $C_{13}$ | $C_{44}$ | $C_{11}/C_{33}$ |
|---|---|---|---|---|---|---|
| Stripa granite (isotropic) | 73.17 | 73.17 | 19.45 | 19.45 | 26.9 | 1 |
| Olkiluoto mica gneiss | 89.74 | 65.87 | 22.22 | 23.51 | 24 | 1.36 |
| Gas-saturated Shaly Coal | 22.08 | 10.91 | 8.36 | 1.25 | 3.71 | 2.02 |
| Woodford53 shale | 28 | 17.3 | 7.5 | 8.3 | 5.6 | 1.62 |
| Opalinius Clay | 57.65 | 28.8 | 54.61 | 38.7 | 0.9 | 2 |
| Yeocheon schist | 91.44 | 27.61 | 33.76 | 20.03 | 13.7 | 3.31 |
| Calcareous mudstone | 90.4 | 35.13 | 51.57 | 39.85 | 6.49 | 2.57 |
| Callovo-Oxfordian argillite | 20.5 | 13.11 | 8.16 | 4.87 | 5.22 | 1.56 |
| Jurassic shale | 39.42 | 27.09 | 15.65 | 16.52 | 6.9 | 1.45 |
| Slate Del Carmen | 35.4 | 26.4 | 0.41 | 1.03 | 21.2 | 1.34 |

**Cubic Materials**

Cubic materials have similar symmetry about three mutually orthogonal planes and thus only 3 independent components of $C_{ijkl}$ are needed. Therefore, for materials of cubic symmetry, we have:

$$C = \begin{bmatrix} C_{11} & C_{12} & C_{12} & 0 & 0 & 0 \\ C_{12} & C_{11} & C_{12} & 0 & 0 & 0 \\ C_{12} & C_{12} & C_{11} & 0 & 0 & 0 \\ 0 & 0 & 0 & C_{44} & 0 & 0 \\ 0 & 0 & 0 & 0 & C_{44} & 0 \\ 0 & 0 & 0 & 0 & 0 & C_{44} \end{bmatrix} \tag{2.11}$$

**Isotropic Materials**

A material with point symmetry or an infinite number of material symmetry planes is said to be isotropic, which leaves only 2 independent components of $C_{ijkl}$. In this case, we have

$$C = \begin{bmatrix} C_{11} & C_{12} & C_{12} & 0 & 0 & 0 \\ C_{12} & C_{11} & C_{12} & 0 & 0 & 0 \\ C_{12} & C_{12} & C_{11} & 0 & 0 & 0 \\ 0 & 0 & 0 & C_{44} & 0 & 0 \\ 0 & 0 & 0 & 0 & C_{44} & 0 \\ 0 & 0 & 0 & 0 & 0 & C_{44} \end{bmatrix} \tag{2.12}$$

with $C_{44} = \frac{1}{2}\left(C_{11} - C_{12}\right)$ and the elasticity tensor can be expressed by two constants

$$C_{ijkl} = \lambda \delta_{ij} \delta_{kl} + G\left(\delta_{ik}\delta_{jl} + \delta_{il}\delta_{jk}\right) \tag{2.13}$$

where $\lambda$ is Lame modulus, $G$ is the shear modulus and $\delta_{ij}$ is the Kronecker operator.

## 2.2 Restrictions on the elastic moduli

The strain energy density per unit volume $U$ for a linear elastic material under a general state of stress is equal to:

$$U = \frac{1}{2}\sum_{i,j=1}^{3}\sigma_{ij}\varepsilon_{ij} = \frac{1}{2}\left(\sigma_{11}\varepsilon_{11} + \sigma_{22}\varepsilon_{22} + \sigma_{33}\varepsilon_{33} + 2\sigma_{12}\varepsilon_{12} + 2\sigma_{13}\varepsilon_{13} + 2\sigma_{23}\varepsilon_{23}\right) \quad (2.14)$$

Since each of the stress and strain matrices are symmetric, they can be represented as vector.

$$U = \frac{1}{2}\left(\varepsilon^T \cdot \sigma\right) = \frac{1}{2}\left(\varepsilon^T \cdot C\varepsilon\right) \quad (2.15)$$

We can use two physical restrictions on the materials to impose mathematical restrictions on the entries of the matrix $C$. These two restrictions are that the material is stable and deformable. Stability means that whenever a state of strain is applied, energy is stored in the material. Stability is also equivalent to the statement that material deformation increases in the direction of increasing stress. The equivalent mathematical restriction on  is

$$U = \frac{1}{2}\left(\varepsilon^T \cdot C\varepsilon\right) > 0 \quad (2.16)$$

Since $C$ is symmetric, the $C$ has to be positive definite. This implies that all its eigenvalues have to be positive. This argument will be used to find restrictions on the values of the elastic moduli mentioned above.

### 2.2.1 Restrictions on the elastic moduli of isotropic material

The three distinct eigenvalues of the matrix $C$ for isotropic material are

$$\frac{1-2\nu}{E};\quad \frac{1+\nu}{E};\quad \frac{2(1+\nu)}{E} \tag{2.17}$$

For this to be positive, the following inequalities have to be satisfied [25]

$$E>0;\qquad -1<\nu<\frac{1}{2} \tag{2.18}$$

### 2.2.2 Restrictions on the elastic moduli of transversely isotropic material

For transversely isotropic material with the $x_3$ as the axis of material symmetry and plane ( $x_1-x_2$ ) as the isotropy plane, the positive definiteness of $C$ implies the following inequalities [25]:

$$E_1>0;\quad E_3>0;\quad G_{13}>0;\quad -1<\nu_{12}<1 \tag{2.19}$$

$$-\sqrt{\frac{E_3}{E_1}}<\nu_{13}<\sqrt{\frac{E_3}{E_1}} \tag{2.20}$$

$$-\sqrt{\frac{E_3(1-\nu_{12})}{2E_1}}<\nu_{13}<\sqrt{\frac{E_3(1-\nu_{12})}{2E_1}} \tag{2.21}$$

## 2.3 Transformation of stress, strain and elastic constant

The elastic stiffness matrix $C$ are usually specified in a basis with coordinate axes aligned with symmetry planes in the material. Since the fracture always propagates in the plane normal to the minimum in-situ stress, the fracture plane is not in the plane of the material

symmetry. It is necessary to understand the transformation of coordinate axes for solving some anisotropic problems.

Consider two orthogonal coordinate systems $(x_1, x_2, x_3)$ and $(x_1', x_2', x_3')$ with a common origin. The transformation between two coordinate systems is given as

$$x_i' = T_{ij} x_j \tag{2.22}$$

where $T_{ij}$ is the direction cosine between the $x_i'$ and $x_j$ axes.

$$T = \begin{bmatrix} \cos(x_1', x_1) & \cos(x_1', x_2) & \cos(x_1', x_3) \\ \cos(x_2', x_1) & \cos(x_2', x_2) & \cos(x_2', x_3) \\ \cos(x_3', x_1) & \cos(x_3', x_2) & \cos(x_3', x_3) \end{bmatrix} \tag{2.23}$$

$T$ is a unitary orthogonal matrix; In practice, it can be computed in terms of the angle between two coordinates. It is straightforward to show that displacement, stress, strain and elasticity tensors transform as

$$u_i' = T_{ij} u_j, \quad \sigma_{ij}' = T_{ik} T_{jl} \sigma_{kl}, \quad \varepsilon_{ij}' = T_{ik} T_{jl} \varepsilon_{kl}, \quad C_{ijkl}' = T_{ip} T_{jq} T_{kr} T_{ls} C_{pqrs} \tag{2.24}$$

Also, the transformation of the elastic stiffness matrix $C$ is given by Bond [26].

$$C' = M_i C M_i^T \tag{2.25}$$

$M_i$ is the 6x6 transformation matrix, subscript $i$ stands for the rotational axis.

$$M_1 = \begin{bmatrix} 1 & 0 & 0 & 0 & 0 & 0 \\ 0 & c^2 & s^2 & 2cs & 0 & 0 \\ 0 & s^2 & c^2 & -2cs & 0 & 0 \\ 0 & -cs & cs & c^2 - s^2 & 0 & 0 \\ 0 & 0 & 0 & 0 & c & -s \\ 0 & 0 & 0 & 0 & s & c \end{bmatrix} \qquad M_2 = \begin{bmatrix} c^2 & 0 & s^2 & 0 & 2cs & 0 \\ 0 & 1 & 0 & 0 & 0 & 0 \\ s^2 & 0 & c^2 & 0 & -2cs & 0 \\ 0 & 0 & 0 & c & 0 & -s \\ -cs & 0 & cs & 0 & c^2 - s^2 & 0 \\ 0 & 0 & 0 & s & 0 & c \end{bmatrix}$$

$$M_3 = \begin{bmatrix} c^2 & s^2 & 0 & 0 & 0 & 2cs \\ s^2 & c^2 & 0 & 0 & 0 & -2cs \\ 0 & 0 & 1 & 0 & 0 & 0 \\ 0 & 0 & 0 & c & s & 0 \\ 0 & 0 & 0 & -s & c & 0 \\ -cs & cs & 0 & 0 & 0 & c^2 - s^2 \end{bmatrix} \tag{2.26}$$

where $s = \sin\theta$ and $c = \cos\theta$ . $\theta$ is the rotational angle measured counterclockwise about the rotational axes.

## 2.4 Dislocation in continuous elastic media

In this section, we will explain some basic definitions and formulas for general curved dislocations. Understanding of the mathematical formalisms of these equations is essential in dislocation theory: the Burger formula for displacement produced by an infinitesimal dislocation element; The Peach-Koehler formula for the stress by such an element; The Blin formula for the interaction energy between two such elements [27]. This knowledge can give us insight of the numerical model we construct in **Chapter 3**. Much of the theory to be presented is generally valid for anisotropic media.

### 2.4.1 Displacements caused by curved dislocation

The derivation of the displacements associated with a dislocation loop of arbitrary shape can be explained by the conservation of the energy in elastic field. Consider a material of infinite extent and suppose that a closed dislocation loop ***C*** of Burger vector ***b*** is created. (Figure 2.1). The creation of the dislocation produces some displacement $\boldsymbol{u}(\boldsymbol{r})$ at ***r***. if a point force ***F*** acts at ***r*** while the dislocation is created, it does work

$$W = \boldsymbol{F} \cdot \boldsymbol{u}(\boldsymbol{r}) = F_m u_m(\boldsymbol{r}) \tag{2.27}$$

Where $u_m$ and $F_m$ are the components of ***u*** and ***F***, respectively. It equals to the work decreased for the creation of loop *C*

$$W = F_m u_m(\boldsymbol{r}) = -\int_A b_i \sigma_{ij} dA_j \tag{2.28}$$

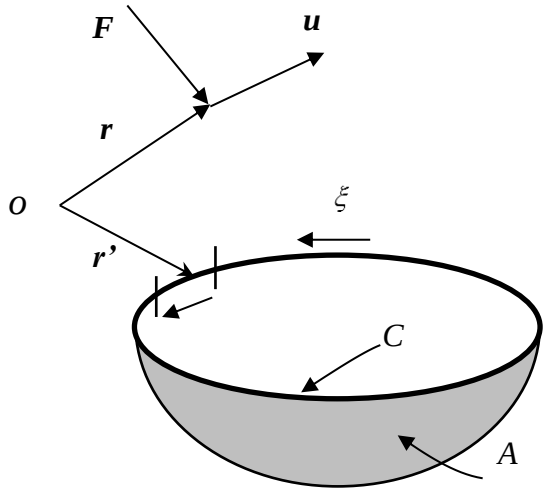


Figure 2.1: A point force ***F*** within an elastic continuum containing a closed dislocation loop

By definition, the Green function $\boldsymbol{G}$ determines the displacement at $\boldsymbol{r'}$ caused by a point force $\boldsymbol{F}$ applied at $\boldsymbol{r}$ as

$$\boldsymbol{u}(\boldsymbol{r'}) = \boldsymbol{G}(\boldsymbol{r'} - \boldsymbol{r}) \cdot \boldsymbol{F} \tag{2.29}$$

From the constitutive relations, the stress field of the point force $\boldsymbol{F}$ can be expressed by Green function as

$$\sigma_{ij}(\boldsymbol{r'}) = C_{ijkl}\left(\frac{\partial}{\partial x_l} G_{km}\right) F_m \tag{2.30}$$

$\boldsymbol{G}$ is symmetric, $G_{km} = G_{mk}$ and invariant with respect to change of sign

$$\boldsymbol{R} = \boldsymbol{r'} - \boldsymbol{r}; \quad \boldsymbol{G}(\boldsymbol{R}) = \boldsymbol{G}(-\boldsymbol{R}) \tag{2.31}$$

Incorporate Eq. (2.30) into Eq. (2.28), the displacement field $\boldsymbol{u}(\boldsymbol{r})$ of a loop $C$ is

$$u_m(\boldsymbol{r}) = -\int_A dA_j b_i C_{ijkl} \frac{\partial}{\partial x'_l} G_{mk}(\boldsymbol{R}) \tag{2.32}$$

This expression was first derived by Burgers. Eq. (2.32) indeed gives a discontinuity $\boldsymbol{b}$ in $\boldsymbol{u}$ across $\boldsymbol{A}$. The dislocation deformations should be continuous everywhere except on the dislocation line itself, suggesting that a line integral for the deformation should be possible. Starting from Eq. (2.32), Mura derived the line integral expression

$$\frac{\partial u_m(\boldsymbol{r})}{\partial x_s} = -\varepsilon_{jsn} b_i C_{ijkl} \oint_C \frac{\partial}{\partial x'_l} G_{mk}(\boldsymbol{R}) dx'_n \tag{2.33}$$

where $\varepsilon_{jsn}$ is the Einstein permutation operator. Eq. (2.32) and Eq. (2.33) are generally valid for an anisotropic material. If Green function $\boldsymbol{G}(\boldsymbol{R})$ is known, the displacement and strain fields of caused by a dislocation of any shape can in principle be calculated.

### 2.4.2 Stress field of curved dislocation in isotropic material

From Eq, (2.13), the relation between stress and strain in isotropic medium can be expressed as

$$\begin{aligned}
\sigma_{11} &= (\lambda + 2G)\varepsilon_{11} + \lambda\varepsilon_{22} + \lambda\varepsilon_{33} \\
\sigma_{22} &= \lambda\varepsilon_{11} + (\lambda + 2G)\varepsilon_{22} + \lambda\varepsilon_{33} \\
\sigma_{33} &= \lambda\varepsilon_{11} + \lambda\varepsilon_{22} + (\lambda + 2G)\varepsilon_{33} \\
\sigma_{23} &= 2G\varepsilon_{23} \\
\sigma_{31} &= 2G\varepsilon_{31} \\
\sigma_{12} &= 2G\varepsilon_{12}
\end{aligned} \tag{2.34}$$

With the use of Eq. (2.34), Eq. (2.32) becomes

$$u_m(\boldsymbol{r}) = -\lambda\int_A dA_j b_j \frac{\partial}{\partial x'_k} G_{mk}(\boldsymbol{R}) - G\int_A dA_j b_i \frac{\partial}{\partial x'_j} G_{mi}(\boldsymbol{R}) - G\int_A dA_j b_i \frac{\partial}{\partial x'_i} G_{mj}(\boldsymbol{R}) \tag{2.35}$$

The expression of the Green function in isotropic case is

$$G_{ij}(\boldsymbol{R}) = \frac{1}{8\pi G}\left(\delta_{ij}\nabla^2 R - \frac{\lambda + G}{\lambda + 2G}\frac{\partial^2 R}{\partial x_i \partial x_j}\right) \tag{2.36}$$

where $\dfrac{\lambda + G}{\lambda + 2G} = 1/2(1-\nu)$ and $\nu$ is the Poisson's ratio. Substituting Eq. (2.36) into Eq. (2.35), the displacement field is

$$\begin{aligned}
u_m(\boldsymbol{r}) = &-\frac{1}{8\pi}\int_A b_m \frac{\partial}{\partial x'_j}\nabla'^2 R dA_j - \frac{1}{8\pi}\int_A b_i \varepsilon_{mik}\nabla'^2 R dx'_k \\
&-\frac{1}{8\pi(1-\nu)}\oint_C b_i \varepsilon_{ijk}\frac{\partial^2 R}{\partial x'_m \partial x'_j} dx'_k
\end{aligned} \tag{2.37}$$

And the stresses for isotropic case can be obtained by differentiation of Eq. (2.37) and insertion of the result in Eq. (2.34)

$$\sigma_{\alpha\beta} = -\frac{G}{8\pi}\oint_C b_m \varepsilon_{im\alpha} \frac{\partial}{\partial x'_i} \nabla'^2 R dx'_\beta - \frac{G}{8\pi}\oint_C b_m \varepsilon_{im\beta} \frac{\partial}{\partial x'_i} \nabla'^2 R dx'_\alpha$$
$$-\frac{G}{4\pi(1-\nu)}\oint_C b_m \varepsilon_{imk} \left( \frac{\partial^3 R}{\partial x'_i \partial x'_\alpha \partial x'_\beta} - \delta_{\alpha\beta} \frac{\partial}{\partial x'_i} \nabla'^2 R \right) dx'_k \tag{2.38}$$

This equation was first derived by Peach and Koehler. Eq. (2.38) enables one to determine the stress field of an arbitrary curved dislocation in isotropic media by line integration.

### 2.4.3 Energy of interaction between two dislocation loops

If dislocation loop $C_1$ is created while loop $C_2$ is present, the stresses $\sigma_2$ originating from loop 2 do work $W_{12}$, where $W_{12}$ is the interaction energy between the two loops (Figure 2.2).

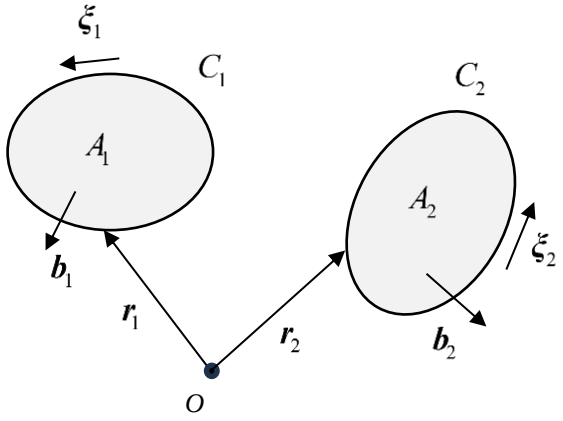


Figure 2.2: Two dislocation loops within the same elastic continuum

The work needed for the creation of loop $C_1$ is reduced by

$$W_{12} = \int_{A_1} (b_1)_\alpha (\sigma_2)_{\alpha\beta} \cdot d(A_1)_\beta \tag{2.39}$$

By means of Eq. (2.38) for $(\sigma_2)_{\alpha\beta}$ and further use of Stokes theorem to convert surface integral to line integral. We can get

$$W_{12} = \frac{G}{4\pi}\oint_{C_1}\oint_{C_2}\frac{(\boldsymbol{b_1}\times\boldsymbol{b_2})\cdot(d\boldsymbol{l_1}\times d\boldsymbol{l_2})}{R} + \frac{G}{4\pi}\oint_{C_1}\oint_{C_2}\frac{(\boldsymbol{b_1}\cdot d\boldsymbol{l_1})(\boldsymbol{b_2}\cdot d\boldsymbol{l_2})}{R} + \frac{G}{4\pi(1-\nu)}\oint_{C_1}\oint_{C_2}(\boldsymbol{b_1}\times d\boldsymbol{l_1})\cdot\boldsymbol{T}\cdot(\boldsymbol{b_2}\times d\boldsymbol{l_2}) \tag{2.40}$$

where $\boldsymbol{T}$ is a tensor with components $T_{ij} = \dfrac{\partial^2 R}{\partial x_i \partial x_j}$

The Eq. (2.40) is known as Blin's formula.

### 2.4.4 The stress field about a straight segment of dislocation in isotropic medium

For problems involving the stress field of a complex dislocation configuration, a useful approximation that greatly reduces the labor of calculation is to divide the arbitrary dislocation line into a sequence of straight dislocation segments and to add the stress fields of the individual segments (Figure 2.4).

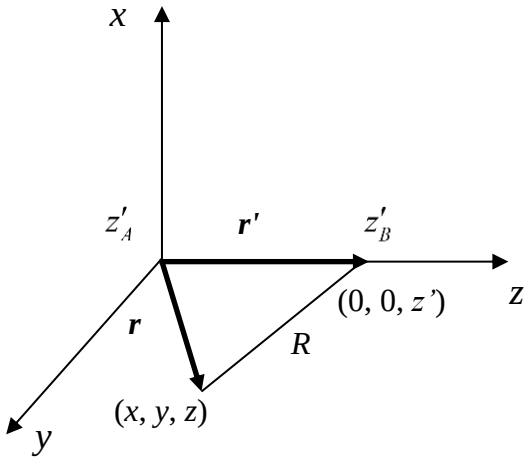


Figure 2.3: Coordinates for a stress dislocation segment

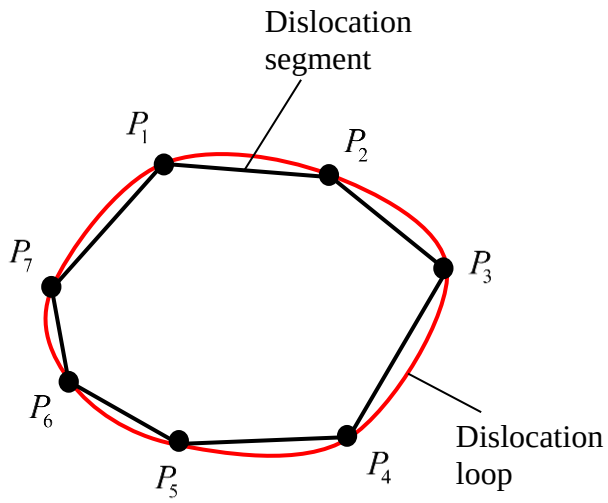


Figure 2.4: Arbitrary dislocation loop discretized into a finite number of straight dislocation segments

The coordinate system in Figure 2.3 is used to calculate the stress field of a straight dislocation segment. The ***r'*** coordinates are fixed on the dislocation line, $x' = y' = 0$ and $z' \neq 0$. We wish to determine the stresses at ***r***, with coordinates $x$, $y$ and $z$. we know $R^2 = x^2 + y^2 + (z - z')^2$.

The stress at ***r*** from a straight segment $z'_A z'_B$ is given by

$$\sigma_{ij} = \sigma_{ij}(z'_B) - \sigma_{ij}(z'_A) \tag{2.41}$$

The calculation of $\sigma_{ij}(z')$ can be obtained from Eq. (2.38), the stress components are

$$\frac{\sigma_{xx}}{\sigma_0} = b_x \frac{y}{R(R+\lambda)}\left[1 + \frac{x^2}{R^2} + \frac{x^2}{R(R+\lambda)}\right] + b_y \frac{x}{R(R+\lambda)}\left[1 - \frac{x^2}{R^2} - \frac{x^2}{R(R+\lambda)}\right]$$

$$\frac{\sigma_{yy}}{\sigma_0} = -b_x \frac{y}{R(R+\lambda)}\left[1 - \frac{y^2}{R^2} - \frac{y^2}{R(R+\lambda)}\right] - b_y \frac{x}{R(R+\lambda)}\left[1 + \frac{y^2}{R^2} + \frac{y^2}{R(R+\lambda)}\right]$$

$$\frac{\sigma_{zz}}{\sigma_0} = b_x\left[\frac{2\nu y}{R(R+\lambda)} + \frac{y\lambda}{R^3}\right] + b_y\left[-\frac{2\nu x}{R(R+\lambda)} - \frac{x\lambda}{R^3}\right]$$

$$\frac{\sigma_{xy}}{\sigma_0} = -b_x\frac{x}{R(R+\lambda)}\left[1-\frac{y^2}{R^2}-\frac{y^2}{R(R+\lambda)}\right] + b_y\frac{y}{R(R+\lambda)}\left[1-\frac{x^2}{R^2}-\frac{x^2}{R(R+\lambda)}\right] \quad (2.42)$$

$$\frac{\sigma_{xz}}{\sigma_0} = -b_x\frac{xy}{R^3} + b_y\left(-\frac{\nu}{R}+\frac{x^2}{R^3}\right) + b_z\frac{y(1-\nu)}{R(R+\lambda)}$$

$$\frac{\sigma_{yz}}{\sigma_0} = b_x\left(\frac{\nu}{R}-\frac{y^2}{R^3}\right) + b_y\frac{xy}{R^3} - b_z\frac{y(1-\nu)}{R(R+\lambda)}$$

where $\sigma_0 = G/4\pi(1-\nu)$ and $\lambda = z'-z$.

# Chapter 3

## Planar three-dimensional hydraulic fracture (PL3D)

### 3.1 Abstract

Planar 3D (PL3D) fracture is a well-known model in hydraulic fracturing simulation which has the advantage to denote arbitrary fracture shapes remaining in a plane. The mathematical formulations and theories of this model are well-established in spite of different fracture propagation criterions implemented to capture the moving fracture front. In this chapter, I present the foundations of the fluid driven PL3D fracture in isotropic material, which includes the explanation of the governing equations and numerical methods we use to solve this problem. In our model, the displacement discontinuity method [28] is used to solve rock deformation and lubrication theory [29] is implemented to determine the fluid pressure inside fracture. The crack tip asymptotic solution and energy release rate criterion [30] are used to capture the fracture front in each time step. This numerical model is validated by comparing with the asymptotic solutions derived by

Savitski and Detournay [31] for impermeable rock and the analytical solution for penny-shaped fracture with uniform internal fluid pressure.

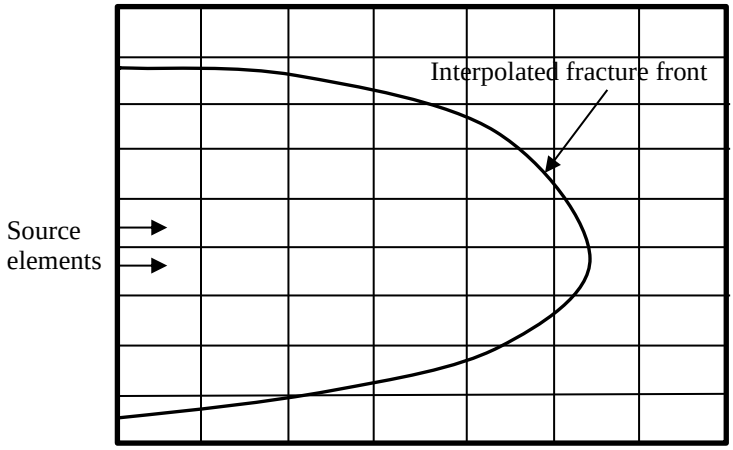


Figure 3.1: Schematic showing planar 3D fracture geometry based on fixed rectangular cells

## 3.2 Introduction

The classical facture models can be 2D, pseudo-3D (P3D), PL3D. The 2D models are PKN (Perkins-Ken-Nordgren) model [12] and KGD (Khristianovich-Geertsma-Daneshy) [15-16], suitable for a single fracture with constant height. Pseudo-3D models include lumped model and cell model which have more engineering applications on the fracture analysis owing to their efficiency in computation and time requirements. The need for PL3D models arose because there are specified types of fracture treatments that P3D models are not suitable to model. For example, when the layer confining stress varies non-monotonically as a function of depth, or when unconfined height growth occurs, P3D models tend to break down numerically. Planar 3D hydraulic fracture models were developed in the 1980s.

Some researchers, such as Advani [32], Barree et al [33] proposed a planar 3D (PL3D) model to simulate fracture propagation. These models assume that the fracture footprint and the coupled fluid flow equation are described by 2D mesh of cells, typically a moving triangular mesh or a fixed rectangular mesh (see Figure 3.1) [34, 35]. The PL3D model uses the full 3D elasticity equation to solve rock which can make this model more accurate but computationally far more expensive than P3D. Adachi et al. [36] generalized the methods of computer simulation in Planar 3D hydraulic fractures. Peirce [37] proposed an implicit level set algorithm to simulate planar 3D fracture by introducing tip analytical solutions. Then Dontsov and Peirce [38] derived a universal tip analytical solution and used it in the implicit level set algorithm [39]. From the analysis of the present fracture models mentioned above, the PL3D model is most useful and feasible considering its accuracy and efficiency. And it has been widely used in dealing with some complicated hydraulic fracturing problems.

In this chapter, we are going to describe the underlying mathematical formulations of HF growth. The explanation contains 1. The displacement discontinuity method is used for solving elasticity equation. 2. The finite volume method implemented in fluid equation inside the fracture. 3. The fracture growth condition. In the end, the numerical model is compared with the analytical solution used for penny-shaped fracture in isotropic material. The verification of this basic model is essential for the following study.

## 3.3 The displacement discontinuity method (DDM)

### 3.3.1 The displacement discontinuity over one-dimensional crack

Consider a tensile crack located at the region $x \in [-L, L]$ and $y = 0$ in an infinite isotropic elastic medium. It is subjected to an internal fluid pressure $p_f$ (Figure 3.2a). This line crack can be discretized by a great number of elements with constant displacement discontinuity proposed by Crouch [28] or a series of distribution of edge dislocation dipoles (see Figure 3.2b and Figure 3.2c).

The displacement discontinuity $D_i$ will be defined as the difference in displacement between the two sides of the segment as follow:

$$\begin{aligned} D_x &= u_x\left(x,0_-\right) - u_x\left(x,0_+\right) \\ D_y &= u_y\left(x,0_-\right) - u_y\left(x,0_+\right) \end{aligned} \tag{3.1}$$

The solution to this problem, known as Kelvin's solution [40], can be expressed in terms of a function:

$$\begin{aligned} f\left(x,y\right) = \frac{-1}{8\pi\left(1-\nu\right)}\Big\{ &\left(x+a\right)\ln\left[\left(x+a\right)^2 + y^2\right] - \left(x-a\right)\ln\left[\left(x-a\right)^2 + y^2\right] \\ &+ 2y\left[\arctan\frac{y}{x-a} - \arctan\frac{y}{x+a}\right]\Big\} \end{aligned} \tag{3.2}$$

where $\nu$ is the Poisson's ratio. The stress field of this constant displacement discontinuity is given based on the derivatives of the function *f*:

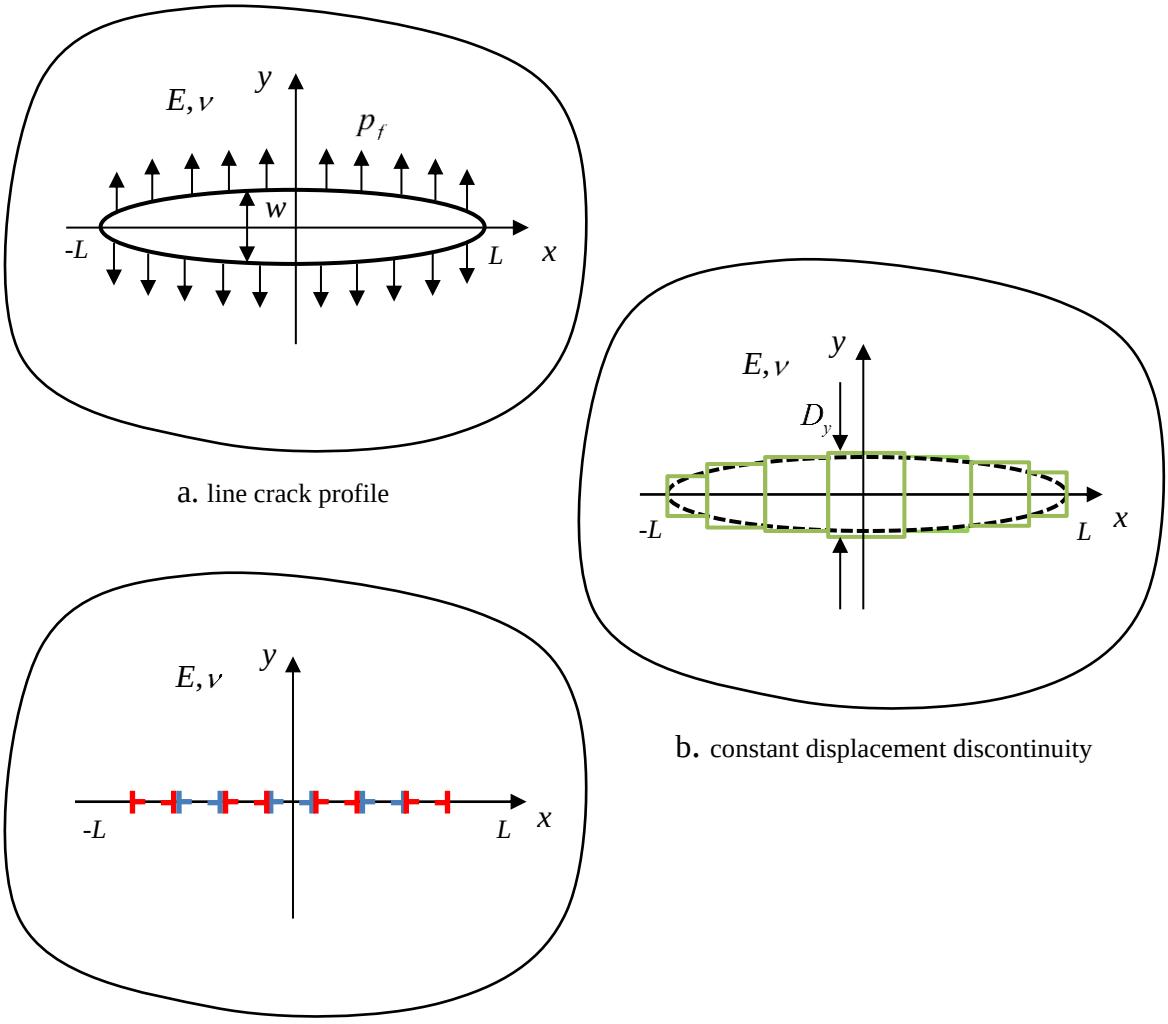


Figure 3.2: DDM and dislocation dipoles implemented on a line crack

$$\begin{cases} \sigma_{xx} = GD_x\left(2f_{,xy} + yf_{,xyy}\right) + 2GD_y\left(f_{,yy} + yf_{,yyy}\right) \\ \sigma_{yy} = GD_x\left(-yf_{,xyy}\right) + 2GD_y\left(f_{,yy} - yf_{,yyy}\right) \\ \sigma_{xy} = GD_x\left(f_{,xy} + yf_{,yyy}\right) + 2GD_y\left(-yf_{,xyy}\right) \end{cases} \tag{3.3}$$

function $f$ and its derivatives are obtained from Kelvin's solution:

$$
\begin{cases}
f_{,x} = \dfrac{1}{4\pi(1-\nu)}\left\{ ln\left[(x-a)^2+y^2\right]^{\frac{1}{2}} - ln\left[(x+a)^2+y^2\right]^{\frac{1}{2}} \right\} \\
f_{,y} = -\dfrac{1}{4\pi(1-\nu)}\left( arctan\dfrac{y}{x-a} - arctan\dfrac{y}{x+a} \right) \\
f_{,xy} = \dfrac{1}{4\pi(1-\nu)}\left[ \dfrac{y}{(x-a)^2+y^2} - \dfrac{y}{(x+a)^2+y^2} \right] \\
f_{,xx} = -f_{,yy} = \dfrac{1}{4\pi(1-\nu)}\left[ \dfrac{x-a}{(x-a)^2+y^2} - \dfrac{x+a}{(x+a)^2+y^2} \right] \\
f_{,xyy} = -f_{,xxx} = \dfrac{1}{4\pi(1-\nu)}\left\{ \dfrac{(x-a)^2-y^2}{\left[(x-a)^2+y^2\right]^2} - \dfrac{(x+a)^2-y^2}{\left[(x+a)^2+y^2\right]^2} \right\} \\
f_{,yyy} = -f_{,xxy} = \dfrac{2y}{4\pi(1-\nu)}\left\{ \dfrac{x-a}{\left[(x-a)^2+y^2\right]^2} - \dfrac{x+a}{\left[(x+a)^2+y^2\right]^2} \right\}
\end{cases}
\tag{3.4}
$$

The stress components on $y = 0$ are also obtained by substituting the Kelvin solutions into the stress equations

$$
\begin{aligned}
\sigma_{xx}(x,0) &= -\frac{G}{\pi(1-\nu)} D_y \frac{a}{x^2-a^2} \\
\sigma_{yy}(x,0) &= -\frac{G}{\pi(1-\nu)} D_y \frac{a}{x^2-a^2} \\
\sigma_{xy}(x,0) &= -\frac{G}{\pi(1-\nu)} D_x \frac{a}{x^2-a^2}
\end{aligned}
\tag{3.5}
$$

For the numerical solution of the crack problem, we divide the crack into *n* line segments. If discontinuity $D_y$ presents on the line segment of length $2a_j$ centered at the point $x = x_j$, $y = 0$, then the opening stress component can be written as

$$
\sigma_{yy}(x,0) = -\frac{G}{\pi(1-\nu)} D_{y,j} \frac{a_j}{(x-x_j)^2 - a_j^{\,2}}
\tag{3.6}
$$

The stress at the midpoint of *i*th element due to displacement discontinuity at the *j*th element can be expresses in below

$$\sigma_{yy}\left(x_i,0\right)=-\frac{G}{\pi\left(1-\nu\right)}D_{y,j}\frac{a_j}{\left(x_i-x_j\right)^2-a_j{}^2} \tag{3.7}$$

The stress at the midpoint of *i*th element due to displacement discontinuity over all elements can be written in a summation form:

$$\sigma_{yy,i}=-p=\sum_{j=1}^{N}A_{ij}D_{y,j} \tag{3.8}$$

The displacement discontinuity $D_y$ can be obtained by solving the system of *N* linear equations.

### 2.3.2 Implementation of the DDM with dislocation theory in planar 3D fracture

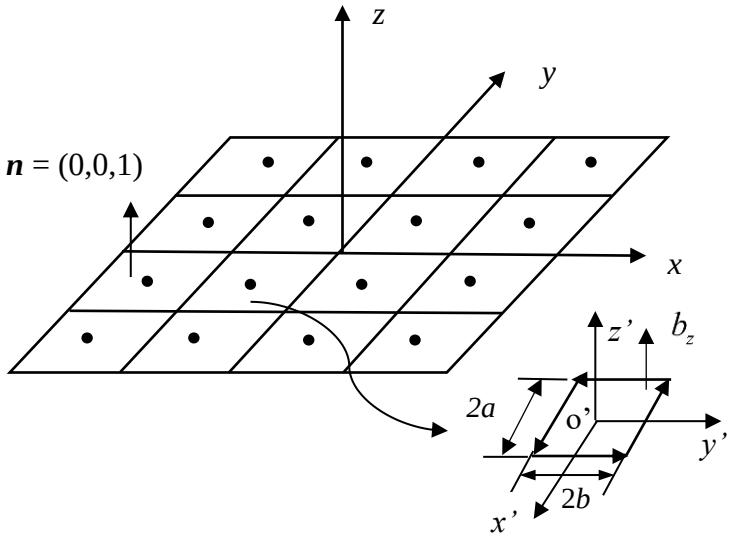


Figure 3.3: Schematics of the finite discretization of the planar 3D fracture using rectangular prismatic dislocation elements

The dislocation distributed technique [41] can be used for discretization of the fracture plane. As shown in Figure 3.3, the planar 3D fracture can be discretized by alignments of rectangular prismatic dislocation loops (mode I fracture) on the fracture plane. Each dislocation loop is composed of four linear dislocation segments. We order the sense of a rectangular dislocation loop in counterclockwise direction starting from the bottom segment and ending with the left segment. The stress field of a single dislocation loop is evaluated at the element center and can be obtained by adding the stress field generated by 4 segments. Therefore, we need to give our first insight into the stress field of a dislocation segment in isotropic medium.

The Peach-Koehler (PK) formula, Eq. (2.38), is an integral equation which enables us to determine the stress field of an arbitrarily curved dislocation in isotropic medium (Figure 2.1). It is formed by three line-integral terms along the dislocation line.

$$\begin{aligned}\sigma_{\alpha\beta} = &-\frac{G}{8\pi}\oint_C b_m \varepsilon_{im\alpha}\frac{\partial}{\partial x'_i}\nabla'^2 R dx'_\beta - \frac{G}{8\pi}\oint_C b_m \varepsilon_{im\beta}\frac{\partial}{\partial x'_i}\nabla'^2 R dx'_\alpha \\ &-\frac{G}{4\pi(1-\nu)}\oint_C b_m \varepsilon_{imk}\left(\frac{\partial^3 R}{\partial x'_i \partial x'_\alpha \partial x'_\beta} - \delta_{\alpha\beta}\frac{\partial}{\partial x'_i}\nabla'^2 R\right) dx'_k\end{aligned} \tag{3.9}$$

Where $b_i$ is the $i$th component of the Burgers vector, $\varepsilon_{imk}$ is the permutation symbol, $G$ is the shear modulus, and $\nu$ is the Poisson's ratio. The prime, used a superscript, indicates quantities belonging to a traced differential line segment $d\boldsymbol{I}'$ of the dislocation loop. The vector $\boldsymbol{R} = \boldsymbol{r}' - \boldsymbol{r}$, with magnitude $R = \sqrt{(x'-x)^2 + (y'-y)^2 + (z'-z)^2}$, is the difference vector between the position vector of dislocation segment $\boldsymbol{r}'$ and position vector $\boldsymbol{r}$ of a field point $P$.

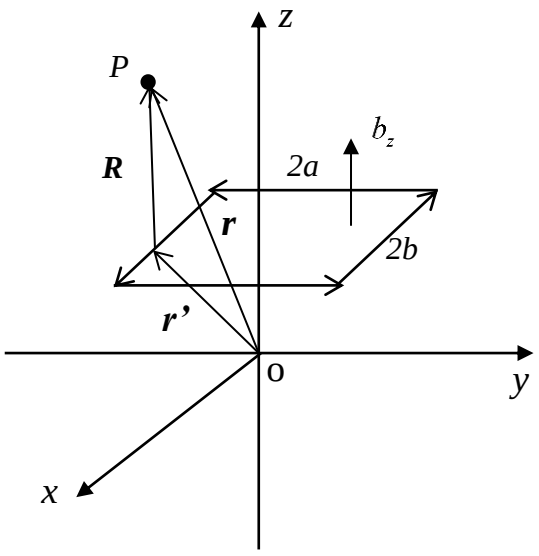


Figure 3.4: A rectangular dislocation loop in isotropic medium

For the detailed integration of PK equation on the rectangular dislocation loop, we can refer to the work by Verecký et al. [42]. Here we only show the stress field of a square prismatic dislocation loop ($a = b$) in $x$-$y$ plane ($z = 0$).

$$\begin{aligned}\sigma_{zz} &= b_z K(x,y) \\ &= \frac{Gb_z}{4\pi(1-\nu)} \\ &\times\left(\frac{\sqrt{(a-x)^2+(a-y)^2}}{(a-x)(a-y)}+\frac{\sqrt{(a+x)^2+(a-y)^2}}{(a+x)(a-y)}\right. \\ &\left.+\frac{\sqrt{(a-x)^2+(a+y)^2}}{(a-x)(a+y)}+\frac{\sqrt{(a+x)^2+(a+y)^2}}{(a+x)(a+y)}\right)\end{aligned} \tag{3.10}$$

Same as the one-dimensional case, using Eq. (3.10), the total stress field at element center can be written by the summation of the stress field of each dislocation element on the fracture plane

$$\sigma_{zz}=\sum_{j=1}^{N}b_z^j K\left(x_i-x_j,y_i-y_j\right)=\sum_{j=1}^{N}\frac{Gb_z^j}{4\pi\left(1-\nu\right)}$$
$$\times\left(\begin{array}{l}\dfrac{\sqrt{\left[a-\left(x_i-x_j\right)\right]^2+\left[a-\left(y_i-y_j\right)\right]^2}}{\left[a-\left(x_i-x_j\right)\right]\left[a-\left(y_i-y_j\right)\right]}+\dfrac{\sqrt{\left[a+\left(x_i-x_j\right)\right]^2+\left[a-\left(y_i-y_j\right)\right]^2}}{\left[a+\left(x_i-x_j\right)\right]\left[a-\left(y_i-y_j\right)\right]}\\+\dfrac{\sqrt{\left[a-\left(x_i-x_j\right)\right]^2+\left[a+\left(y_i-y_j\right)\right]^2}}{\left[a-\left(x_i-x_j\right)\right]\left[a+\left(y_i-y_j\right)\right]}+\dfrac{\sqrt{\left[a+\left(x_i-x_j\right)\right]^2+\left[a+\left(y_i-y_j\right)\right]^2}}{\left[a+\left(x_i-x_j\right)\right]\left[a+\left(y_i-y_j\right)\right]}\end{array}\right) \quad (3.11)$$

**Elasticity Equation**

Given the assumptions that the rock is homogeneous and linear elastic, the elasticity equation relating the displacement discontinuity components and induced stress fields in the solid can be condensed into following equation [36]

$$p_f-\sigma_h=\int_S w\left(x',y'\right)K\left(x-x',y-y'\right)dA' \quad (3.12)$$

Where the net pressure $p_f-\sigma_h$ controls the opening of the fracture. $p_f$ is the fluid pressure inside the fracture which is neither uniform nor constant during propagation and $\sigma_h$ is the minimum in-situ stress normal to the fracture surface. *K* is the kernal function contains all information about the medium. Especially, for isotropic material, assuming $w\left(x',y'\right)$ to be the piecewise constant, the *K* can be written as Eq. (3.11) and Eq. (3.12) can be expressed as

$$p_f^i - \sigma_h = \sum_{j=1}^{N} \frac{Gb_z^j}{4\pi(1-\nu)}$$

$$\left( \frac{\sqrt{\left[a-\left(x^i_{O'}-x^j_{O'}\right)\right]^2+\left[a-\left(y^i_{O'}-y^j_{O'}\right)\right]^2}}{\left[a-\left(x^i_{O'}-x^j_{O'}\right)\right]\left[a-\left(y^i_{O'}-y^j_{O'}\right)\right]} + \frac{\sqrt{\left[a+\left(x^i_{O'}-x^j_{O'}\right)\right]^2+\left[a-\left(y^i_{O'}-y^j_{O'}\right)\right]^2}}{\left[a+\left(x^i_{O'}-x^j_{O'}\right)\right]\left[a-\left(y^i_{O'}-y^j_{O'}\right)\right]} \right.$$
$$\left. + \frac{\sqrt{\left[a-\left(x^i_{O'}-x^j_{O'}\right)\right]^2+\left[a+\left(y^i_{O'}-y^j_{O'}\right)\right]^2}}{\left[a-\left(x^i_{O'}-x^j_{O'}\right)\right]\left[a+\left(y^i_{O'}-y^j_{O'}\right)\right]} + \frac{\sqrt{\left[a+\left(x^i_{O'}-x^j_{O'}\right)\right]^2+\left[a+\left(y^i_{O'}-y^j_{O'}\right)\right]^2}}{\left[a+\left(x^i_{O'}-x^j_{O'}\right)\right]\left[a+\left(y^i_{O'}-y^j_{O'}\right)\right]} \right) \quad (3.13)$$

## 3.4 Fluid flow inside the fracture

### 3.4.1 Lubrication Theory

In fluid dynamics, lubrication theory describes the fluid flow in a geometry where one dimension is significantly smaller than the others. The application of lubrication theory in hydraulic fracturing is extremely popular because the aperture of a hydraulic fracture is always much smaller than its length and height. With the *z*-axis as the fracture opening direction and following assumptions made in fluid flow (Figure 3.5):

1. Negligible body force and inertia force so that all the terms associated with $\rho$ and $g$ are zero
2. Newtonian fluid with laminar flow
3. Constant pressure and velocity through the thin film because the dimension in this direction is significantly smaller than the others

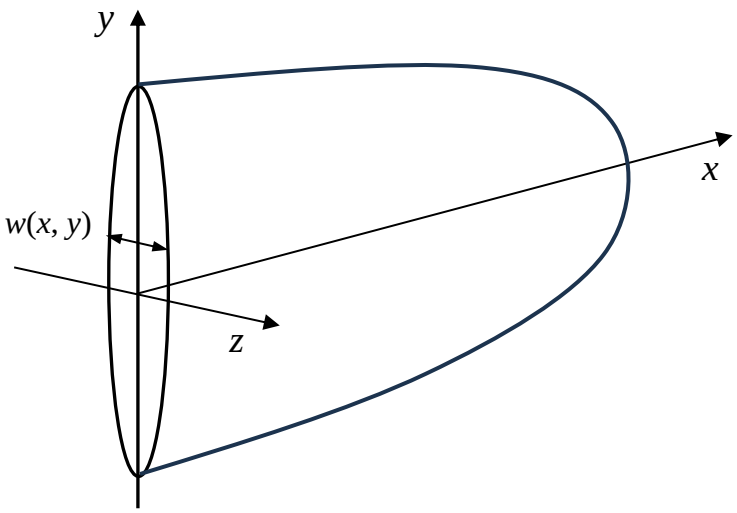


Figure 3.5: The schematics of a 3D hydraulic fracture

The flow flux inside the fracture can be expressed in Poiseuille's law [43]:

$$\boldsymbol{q} = \frac{w^3}{12\mu}\nabla p \tag{3.14}$$

Where $\nabla = (\partial/\partial x, \partial/\partial y)$ is the gradient operator, $\boldsymbol{q}$ is the flow rate, $w$ is the fracture width, $\mu$ is the viscosity of the fracturing fluid and $p$ is the fluid pressure.

The continuity equation [29] of the incompressible fluid flow can be written into

$$\frac{\partial w}{\partial t} + \nabla \cdot \boldsymbol{q} + v_L = Q(x, y)\delta(x, y) \tag{3.15}$$

where $\partial w/\partial t$ is the rate of the fracture volume change; $\nabla \cdot \boldsymbol{q}$ is the fluid net flow; $v_L$ denotes the velocity of the fluid leaking out of the two opposite faces of the fracture. $Q$ is the injection rate of the fracturing fluid.

The leak off fluid velocity $v_L$ is evaluated using Carter's Leakoff model [36]:

$$v_L = \frac{2C_L(x,y)}{\sqrt{t - t_0(x,y)}} \tag{3.16}$$

where $C_L$ is the Carter's leakoff coefficient which depends on the rock and properties of the fracturing fluid; $t_0$ is the time that the fracture gets exposed to the fluid.

### 3.4.2 Power-law fluids

Almost all the working fluids used in hydraulic fracturing behave in the manner of Power-law fluid. [43]

$$\tau = K'\dot{\gamma}^{n'} \tag{3.15}$$

where $\tau$ is the shear stress; $\dot{\gamma}$ is the shear rate; $K'$ is the consistency index and $n'$ is the flow behavior index. As $n' = 1$, the fluid is Newtonian fluid.

For one-dimensional laminar power-law fluid flow between two parallel plates along *x* and *y* directions, the flow flux is given by

$$q_x = -\frac{n'}{2+4n'}\left(\frac{w^{2n'+1}}{2K'}\right)^{1/n'}\left|\frac{\partial p}{\partial x}\right|^{1/n'-1}\frac{\partial p}{\partial x} \tag{3.16}$$

$$q_x = -\frac{n'}{2+4n'}\left(\frac{w^{2n'+1}}{2K'}\right)^{1/n'}\left|\frac{\partial p}{\partial y}\right|^{1/n'-1}\frac{\partial p}{\partial y} \tag{3.17}$$

where absolute value in pressure gradient is used to present the direction of the flow.

### 3.4.3 Finite Volume Method (FVM)

We begin our derivation of the finite volume equations for 2D geometry by considering integration of the diffusion equation on a Cartesian mesh. The governing equation is written as

$$\frac{\partial}{\partial x}\left(\lambda\frac{\partial \Phi}{\partial x}\right)+\frac{\partial}{\partial y}\left(\lambda\frac{\partial \Phi}{\partial y}\right)=-S_{\Phi} \tag{3.17}$$

Where $\lambda$ is a spatial dependent coefficient; $\Phi$ is a physical property

The computation domain is first split into a set of smaller control volumes or cells. A typical structured mesh is shown in Figure 3.6. All information is stored at cell centers, while fluxes are computed at cell faces. The cell centers are denoted by O, E, W, N and S, while the cell faces are denoted by *e*, *w*, *n* and *s*.

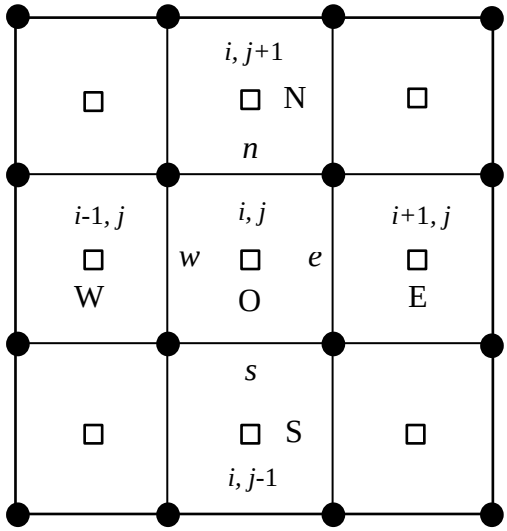


Figure 3.6: Schematics of finite volume grid

Next, we integrate Eq. (3.17) over the control volume O, shown in Figure 3.6. It yields

$$\int_s^n \int_w^e \frac{\partial}{\partial x}\left(\lambda \frac{\partial \Phi}{\partial x}\right) dxdy + \int_s^n \int_w^e \frac{\partial}{\partial y}\left(\lambda \frac{\partial \Phi}{\partial y}\right) dxdy = -\int_s^n \int_w^e S_\Phi dxdy \tag{3.18}$$

Where the face notations have been used to define the integration limits. To simplify Eq. (3.18), the order of the integration in the second term on the left- hand side is changed, and both terms on the left-hand side integrated once to yield

$$\int_s^n \left(\lambda \frac{\partial \Phi}{\partial y}\right)\Bigg|_w^e dy + \int_w^e \left(\lambda \frac{\partial \Phi}{\partial y}\right)\Bigg|_s^n dx = -\int_s^n \int_w^e S_\Phi dxdy \tag{3.19}$$

Using the definition of volume average and realizing that the quantities within square brackets represents average fluxes at individual faces of the cell, Eq. (3.19) may be further simplified to write as

$$\left[\left(\lambda \frac{\partial \Phi}{\partial x}\right)_e - \left(\lambda \frac{\partial \Phi}{\partial x}\right)_w\right]\Delta y + \left[\left(\lambda \frac{\partial \Phi}{\partial y}\right)_n - \left(\lambda \frac{\partial \Phi}{\partial y}\right)_s\right]\Delta x = -S_\Phi \Delta x \Delta y \tag{3.20}$$

In deriving Eq. (3.19) from (3.20), it has been assumed that the average flux at a face is equivalent to the value of the flux computed at the geometric center of the face. This assumption is commensurate with the assumption that the volume average of a variable is same as the value of the variable evaluated at the geometric centroid.

The first derivative appearing in Eq. (3.20) may be approximated using the Taylor series expansion-based procedure and coefficient $\lambda$ can be evaluated by linear interpolation between two adjacent nodes. Thus, the Eq. (3.20) can be written as

$$\left(\frac{\lambda_E+\lambda_O}{2}\right)\left(\frac{\Phi_E-\Phi_O}{\Delta x}\right)\Delta y-\left(\frac{\lambda_O+\lambda_W}{2}\right)\left(\frac{\Phi_O-\Phi_W}{\Delta x}\right)\Delta y$$
$$+\left(\frac{\lambda_N+\lambda_O}{2}\right)\left(\frac{\Phi_N-\Phi_O}{\Delta y}\right)\Delta x-\left(\frac{\lambda_O+\lambda_S}{2}\right)\left(\frac{\Phi_O-\Phi_S}{\Delta y}\right)\Delta x=-S_\Phi\Delta x\Delta y \tag{3.21}$$

Eq. (3.21) is valid only for the interior cells and its range of validity excludes the cells adjacent to the boundaries. This is because the central difference method cannot be used for the cells at the boundaries. The derivation of these flux terms requires application of the boundary conditions.

### 3.4.4 Implementation of FVM in planar 3D hydraulic fracture

The fluid flow inside the fracture follows lubrication theory [29]. Under the assumption of an incompressible power-law fluid and an impermeable surrounding formation (no leakoff), the width averaged fluid mass conservation equation reduces to the following form from Eq. (3.15):

$$\frac{\partial w}{\partial t}+\nabla\cdot\boldsymbol{q}=Q_0\delta(x,y) \tag{3.22}$$

$Q_0$ denotes the constant injection rate. The fluid flux $\boldsymbol{q}$ is related to the fluid pressure gradient and fracture opening via the Poiseuille's law from Eq. (3.15) and Eq. (3.16).

Following the FVM mentioned in **Section 3.4.3** and using the forward-Euler schemes for time integration, in any element not on boundary, the Eq. (3.22) can be rewritten as

$$\left(q_x\big|_e-q_x\big|_w\right)\Delta y+\left(q_y\big|_n-q_y\big|_s\right)\Delta x=\left(Q_0\delta\left(x,y\right)-\frac{w_O^{n+1}-w_O^n}{\Delta t}\right)\Delta x\Delta y \tag{3.23}$$

where $Q_0$ is only a nonvanishing term at the injection elements. We incorporate Eq. (3.15) and Eq. (3.16) into the Eq. (3.23) and follow the method in Eq. (3.21), we can get

$$\left(\frac{\Gamma_E+\Gamma_O}{2}\right)\left(\frac{p_E-p_O}{\Delta x}\right)^{\frac{1}{n'}}\Delta y-\left(\frac{\Gamma_O+\Gamma_W}{2}\right)\left(\frac{p_O-p_W}{\Delta x}\right)^{\frac{1}{n'}}\Delta y+\left(\frac{\Gamma_N+\Gamma_O}{2}\right)\left(\frac{p_N-p_O}{\Delta y}\right)^{\frac{1}{n'}}\Delta x$$
$$-\left(\frac{\Gamma_O+\Gamma_S}{2}\right)\left(\frac{p_O-p_S}{\Delta y}\right)^{\frac{1}{n'}}\Delta x=\left(Q_0\delta(x,y)-\frac{w_O^{n+1}-w_O^n}{\Delta t}\right)\Delta x\Delta y \tag{3.24}$$

where $\Gamma_i=-\frac{n'}{2+4n'}\left(\frac{w_i^{2n'+1}}{2K'}\right)^{\frac{1}{n'}}$ and *i* denotes cell centers by E, W, N, S, O. For our convenience, Eq. (3.24) can be rearranged as

$$w_O^{n+1}=w_O^n-\left(\frac{\Gamma_E+\Gamma_O}{2}\right)\left(\frac{p_E-p_O}{\Delta x}\right)^{\frac{1}{n'}}\frac{\Delta t}{\Delta x}+\left(\frac{\Gamma_O+\Gamma_W}{2}\right)\left(\frac{p_O-p_W}{\Delta x}\right)^{\frac{1}{n'}}\frac{\Delta t}{\Delta x}$$
$$-\left(\frac{\Gamma_N+\Gamma_O}{2}\right)\left(\frac{p_N-p_O}{\Delta y}\right)^{\frac{1}{n'}}\frac{\Delta t}{\Delta y}+\left(\frac{\Gamma_O+\Gamma_S}{2}\right)\left(\frac{p_O-p_S}{\Delta y}\right)^{\frac{1}{n'}}\frac{\Delta t}{\Delta y}+Q_0\delta(x,y)\Delta t \tag{3.25}$$

Eq. (3.25) explicitly shows how fracture width in the next time step depends on fluid pressure and fracture width in the current time step. Alternatively, Eq. (3.24) can also be written by the width averages as

$$\Gamma_{EO}\left(\frac{p_E-p_O}{\Delta x}\right)^{\frac{1}{n'}}\Delta y-\Gamma_{OW}\left(\frac{p_O-p_W}{\Delta x}\right)^{\frac{1}{n'}}\Delta y$$
$$+\Gamma_{NO}\left(\frac{p_N-p_O}{\Delta y}\right)^{\frac{1}{n'}}\Delta x-\Gamma_{OS}\left(\frac{p_O-p_S}{\Delta y}\right)^{\frac{1}{n'}}\Delta x=\left(Q_0\delta(x,y)-\frac{w_O^{n+1}-w_O^n}{\Delta t}\right)\Delta x\Delta y \tag{3.26}$$

where $\Gamma_{ij}=-\frac{n'}{2+4n'}\left(\frac{1}{2K'}\right)^{\frac{1}{n'}}\left(\frac{w_i+w_j}{2}\right)^{\frac{2n'+1}{n'}}$ and *i* denotes cell centers by E, W, N, S, O.

As the same, Eq. (3.25) can be written as

$$w_O^{n+1} = w_O^n - \Gamma_{EO}\left(\frac{p_E - p_O}{\Delta x}\right)^{\frac{1}{n'}}\frac{\Delta t}{\Delta x} + \Gamma_{OW}\left(\frac{p_O - p_W}{\Delta x}\right)^{\frac{1}{n'}}\frac{\Delta t}{\Delta x}$$
$$-\Gamma_{NO}\left(\frac{p_N - p_O}{\Delta y}\right)^{\frac{1}{n'}}\frac{\Delta t}{\Delta y} + \Gamma_{OS}\left(\frac{p_O - p_S}{\Delta y}\right)^{\frac{1}{n'}}\frac{\Delta t}{\Delta y} + Q_0\delta(x,y)\Delta t \tag{3.27}$$

**Boundary conditions**

We restrict here to the case where the fluid and fracture fronts coincide. Thus, along the perimeter of the fracture $(\Omega(t))$, we specify a zero fluid flux boundary condition given by the Detournay and Peirce [44]

$$w(\boldsymbol{x}_\Omega, t) = 0, \quad \boldsymbol{q}(\boldsymbol{x}_\Omega, t) = 0, \quad \boldsymbol{x}_\Omega \in \Omega(t) \tag{3.28}$$

Let's only focus on the control volumes adjacent to the left boundary, the flow flux through the left edge of the cell equals to the zero according to the Eq. (3.28). Thus Eq. (3.23) can be expressed as

$$q_x\big|_e \Delta y + \left(q_y\big|_n - q_y\big|_s\right)\Delta x = \left(Q_0\delta(x,y) - \frac{w_O^{n+1} - w_O^n}{\Delta t}\right)\Delta x \Delta y \tag{3.29}$$

Then Eq. (3.25) and Eq. (3.27) can be rewritten by dropping the corresponding term. For Eq. (3.25), we can obtain

$$w_O^{n+1} = w_O^n - \left(\frac{\Gamma_E + \Gamma_O}{2}\right)\left(\frac{p_E - p_O}{\Delta x}\right)^{\frac{1}{n'}}\frac{\Delta t}{\Delta x} - \left(\frac{\Gamma_N + \Gamma_O}{2}\right)\left(\frac{p_N - p_O}{\Delta y}\right)^{\frac{1}{n'}}\frac{\Delta t}{\Delta y}$$
$$+\left(\frac{\Gamma_O + \Gamma_S}{2}\right)\left(\frac{p_O - p_S}{\Delta y}\right)^{\frac{1}{n'}}\frac{\Delta t}{\Delta y} + Q_0\delta(x,y)\Delta t \tag{3.30}$$

This strategy is applicable to all boundary elements. Even though some of elements are adjacent to multiple fracture boundaries, we only need to drop more terms which correspond to these boundary conditions.

## 3.5 Fracture propagation criterion

We use linear elastic fracture mechanics (LEFM) and energy-based fracturing criterion. The criterion states that a fracture extends if the energy release rate of the fracture front is greater than the critical energy release rate $G_c$ for creating a new material surface. The critical energy release is a property of the material that the fracture is propagating in.

### 3.5.1 Asymptotic solution in isotropic material

The critical stress intensity factor $K_{Ic}$ introduced by Irwin in 1948 [30], also known as fracture toughness, can be derived from $G_c$, For mode-I fractures in isotropic material, the relationship is

$$G_c = \frac{K_{Ic}^2}{E'} = K_{Ic}^2\left(\frac{1-\nu^2}{E}\right) \tag{3.31}$$

The stress intensity factor is a fundamental quantity that governs the stress field near the crack tip. According to the LEFM, the asymptotic stress field at the crack tip has a square-root singularity. For the mode-I fracture in isotropic material, it is given as [45]

$$\sigma_{xx} = \frac{K_I}{\sqrt{2\pi r}}\cos\left(\frac{\theta}{2}\right)\left[1-\sin\left(\frac{\theta}{2}\right)\sin\left(\frac{3\theta}{2}\right)\right] \tag{3.32a}$$

$$\sigma_{yy} = \frac{K_I}{\sqrt{2\pi r}} \cos\left(\frac{\theta}{2}\right)\left[1+\sin\left(\frac{\theta}{2}\right)\sin\left(\frac{3\theta}{2}\right)\right] \tag{3.32b}$$

$$\sigma_{xy} = \frac{K_I}{\sqrt{2\pi r}} \cos\left(\frac{\theta}{2}\right)\sin\left(\frac{\theta}{2}\right)\cos\left(\frac{3\theta}{2}\right) \tag{3.32c}$$

The associated displacement is

$$u_x = \frac{K_I}{2G}\left(\frac{r}{2\pi}\right)^{1/2} \cos\left(\frac{\theta}{2}\right)\left[\kappa - 1 + 2\sin^2\left(\frac{\theta}{2}\right)\right] \tag{3.33a}$$

$$u_y = \frac{K_I}{2G}\left(\frac{r}{2\pi}\right)^{1/2} \sin\left(\frac{\theta}{2}\right)\left[\kappa + 1 - 2\cos^2\left(\frac{\theta}{2}\right)\right] \tag{3.33b}$$

where $\kappa = (3-4\nu)$ for plane strain and $\kappa = (3-\nu)/(1+\nu)$ for plane stress. For isotropic material, the quasi-static linear elastic fracture mechanics propagation condition ($G = G_c$) can alternatively be written as equality of the stress intensity factor with the material fracture toughness ($K_I = K_{Ic}$). The asymptotic solution Eq. (3.33b) can be used as the fracture propagation criterion.

$$w = \sqrt{\frac{32}{\pi}}\frac{K_{Ic}}{E'} r^{1/2} \tag{3.34}$$

where *w* is the fracture width; *r* is the distance to the fracture front and $E' = E/(1-\nu^2)$ is the plane strain Young's modulus.

### 3.5.2 Asymptotic solution in the anisotropic solid

In the general case, the Irwin relation for the energy release rate per unit area of co-planar crack extension as function of the stress intensity factor $K_i$ ($i$ = 1, 2, 3) is given by Barnett and Asaro [30].

$$G_e = \frac{1}{2} K_i B_{ij}^{-1} K_j \qquad i, j = 1, 2, 3 \tag{3.31}$$

where $B_{ij}$ is the matrix of elastic moduli in anisotropic material that depends on the direction of the crack front and elastic tensor $C_{ijkl}$. However, $B_{ij}$ is not necessarily diagonal for an anisotropic solid. Its expression can be obtained by numerical integration or solving an eigenvalue problem which will be explained in **Chapter 4** (see **section 4.3** and **4.4**). The direction of stress intensity factor and corresponding fracture mode are shown in Figure 3.7. Especially, for isotropic case, $B_{11} = B_{22} = 2E'$, $B_{33} = G = \frac{E}{2(1+\nu)}$.

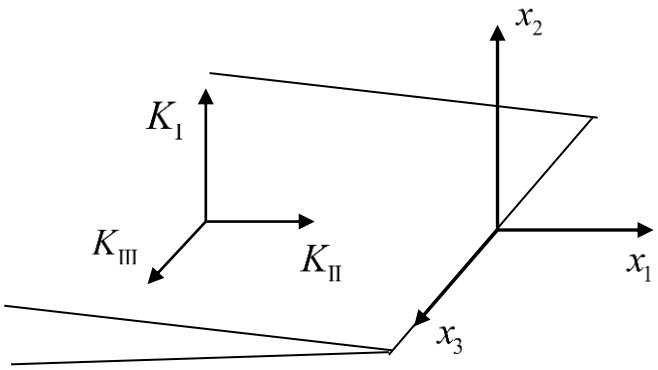


Figure 3.7: Fracture front in anisotropic medium

With reference to the Figure 3.7, the three stress intensity factors $K_i$ are defined as

$$\sigma_{i2}\big|_{x_1\to 0, x_2=0} = \frac{K_i}{(2\pi x)^{1/2}} + \text{non-singular terms} \tag{3.33}$$

where $K_1 = K_{\text{II}}$ (sliding mode), $K_2 = K_{\text{I}}$ (opening mode), $K_3 = K_{\text{III}}$ (tearing mode).

Similarly, the asymptotic displacement solution near the crack front can be expressed as [46]

$$u_i = 4B_{ij}^{-1}K_j\left(\frac{r}{2\pi}\right)^{1/2} \tag{3.34}$$

## 3.6 Simulation results on planar 3D model

### 3.6.1 Static solution for penny-shaped fracture

For the three-dimensional crack created in the infinite isotropic medium, it is called 'penny-shaped' with radius of *R*. the fracture is axially symmetry about the *z* axis, as shown in Figure 3.8. The exact solution to a static penny-shaped fracture without leakoff under the constant net pressure $p_0$ is given by the following equations [47]:

The fracture width:

$$w(r) = \frac{8p_0}{\pi E'}\sqrt{R^2 - r^2} \tag{3.35}$$

This static analysis can be carried out by setting a long-time shut-in period after the injection so that the fracture will not grow and fluid pressure becomes uniform.

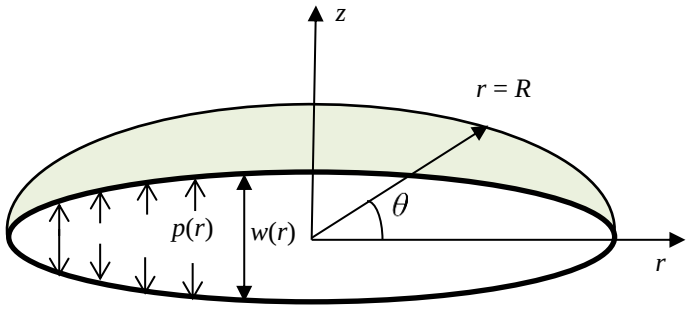


Figure 3.8: Penny-shaped fracture in cylindrical coordinates

**Test parameters:**

$E = 20\,\text{GPa}$ ; $v = 0.2$ ; $K_{Ic} = 1\,\text{MPa}\cdot\sqrt{\text{m}}$ ; $\mu = 0.005\,\text{Pa}\cdot\text{s}$ ; $Q_0 = 0.02\,\text{m}^3/\text{s}$ (injection rate); $t_{inj} = 10\,\text{s}$ (injection time); $t_{total} = 10000\text{s}$ (total time)

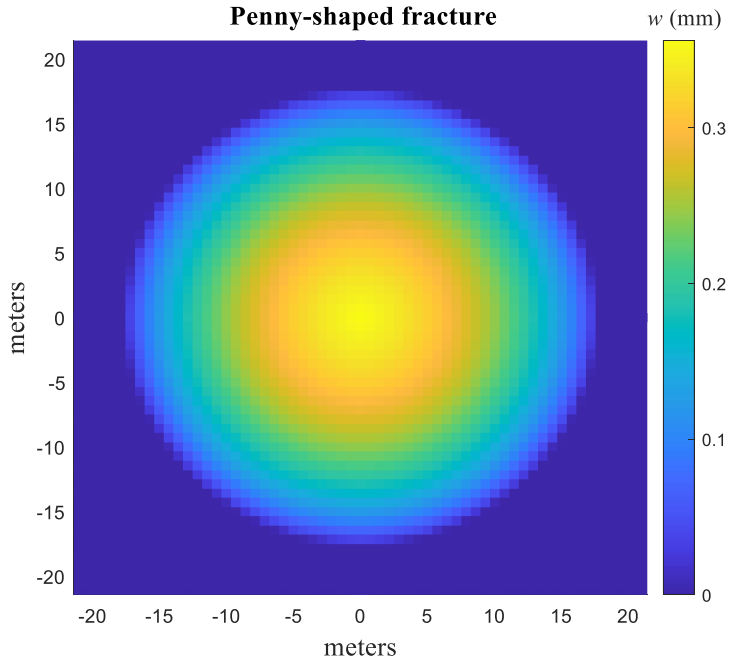


Figure 3.9: Geometry of the penny-shaped fracture

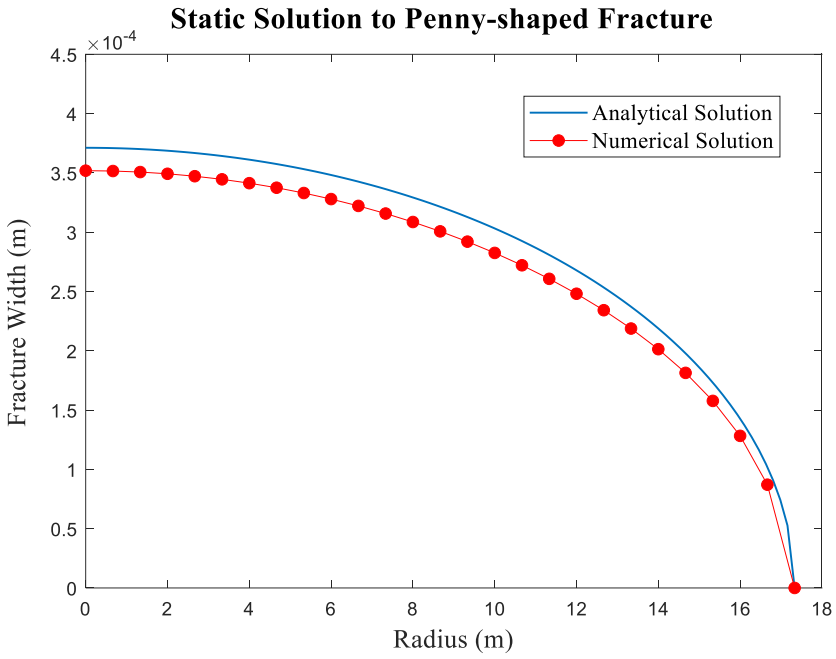


Figure 3.10: Comparison results of static penny-shaped fracture

Figure 3.9 shows the circular geometry of the penny-shaped fracture after a long shut-in period. The fracture width is demonstrated by color filling. Figure 3.10 gives the comparison results on fracture width between numerical solution and analytical solution. The maximum error at injection is about 4%.

### 3.6.2. Asymptotic solution for a penny-shaped fracture in an impermeable rock

An asymptotic solution to the fluid-driven penny-shaped fracture in an impermeable elastic rock is constructed rigorously by Savitski and Detournay [31]. This solution is applicable to the fracture model driven by an incompressible Newtonian fluid injected from a source at the center of the fracture. Asymptotic solution is differentiated by two propagating

regimes: toughness-dominated regime and viscosity-dominated regime which related with only one dimensionless parameter $\kappa$.The dimensionless toughness $\kappa$ is defined as

$$\kappa = K'_{Ic}\left(\frac{t^2}{\mu'^5 Q_0^3 E'^{13}}\right)^{\frac{1}{18}} \tag{3.35}$$

where $K'_{Ic} = 4\sqrt{\frac{2}{\pi}}K_{Ic}$, $\mu' = 12\mu$, $E' = \frac{E}{\left(1-\nu^2\right)}$ and *t* is the injection duration.

*Viscosity-dominated regime* ($\kappa = 0$): In this regime, the fracture toughness effect can be neglected. The energy is dissipated by viscous fluid flow and the fracture shape can be identified by fluid front.

*Toughness-dominated regime* ($\kappa = \infty$): In this regime, the fluid viscosity effect can be neglected. The energy is dissipated in the rock to create a new surface and the fracture shape can be determined by crack tip asymptotic solution.

In the real simulation, these two regimes can be distinguished by the specific value of the $\kappa$. As $\kappa < 1$, we can use the zero-toughness solution; $\kappa > 3.5$, we use the large-toughness solution. Two solutions are given in **Appendix A**.

I compare numerical results corresponding to small (viscosity-dominated regime) and large (toughness-dominated regime) values of dimensionless parameter $\kappa$ to the asymptotic solution. Figure 3.11 shows the dimensionless opening displacement and fluid pressure in the viscosity scaling for small values of $\kappa$. It is clear that while the parameter $\kappa$ is small the matching between the numerical solution and zero-toughness asymptotic solution is very good.

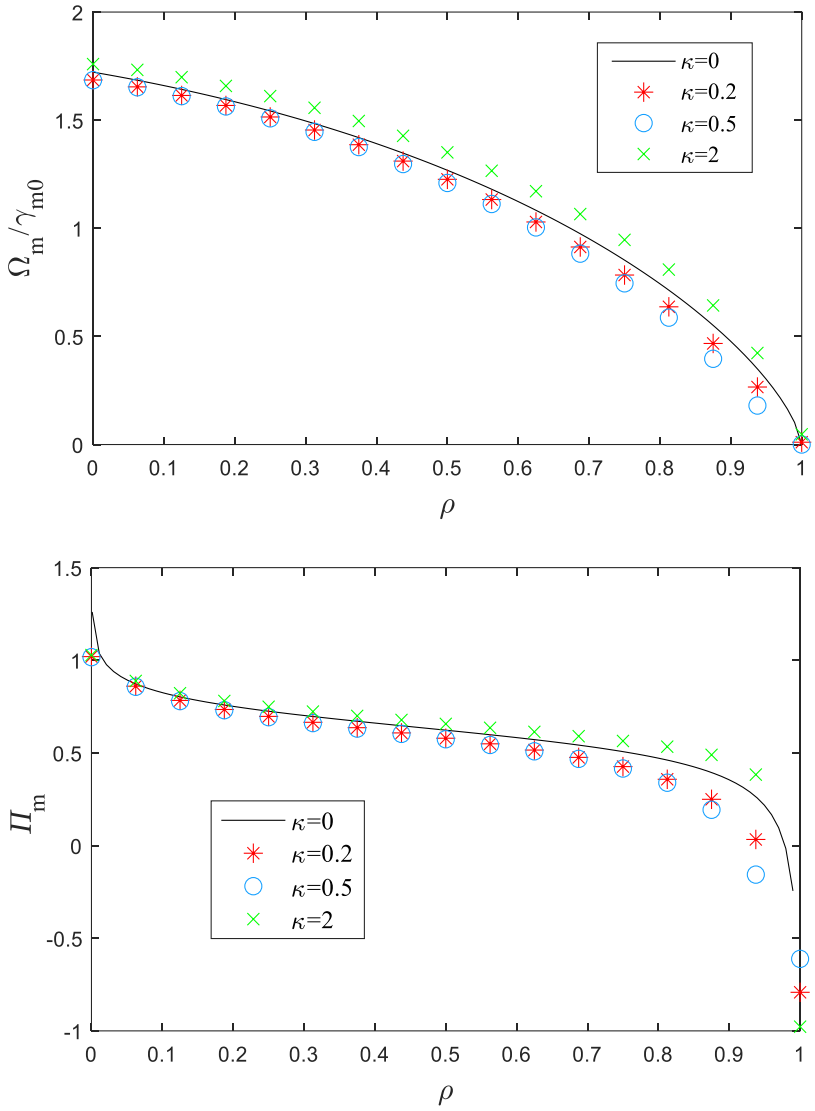


Figure 3.11: Comparison of the opening displacement and fluid pressure of analytical solution and numerical simulation given in the viscosity scaling for $\kappa = 0.2, 0.5, 2$

The results of the large-toughness comparison are given in Figure 3.12. The solid line corresponds to the asymptotic solution in toughness scaling. The error between the numerical result and analytical solution for large toughness cases is more significant than

the zero-toughness one. As the dimensionless parameter $\kappa$ decreases. The difference between them becomes more and more evident.

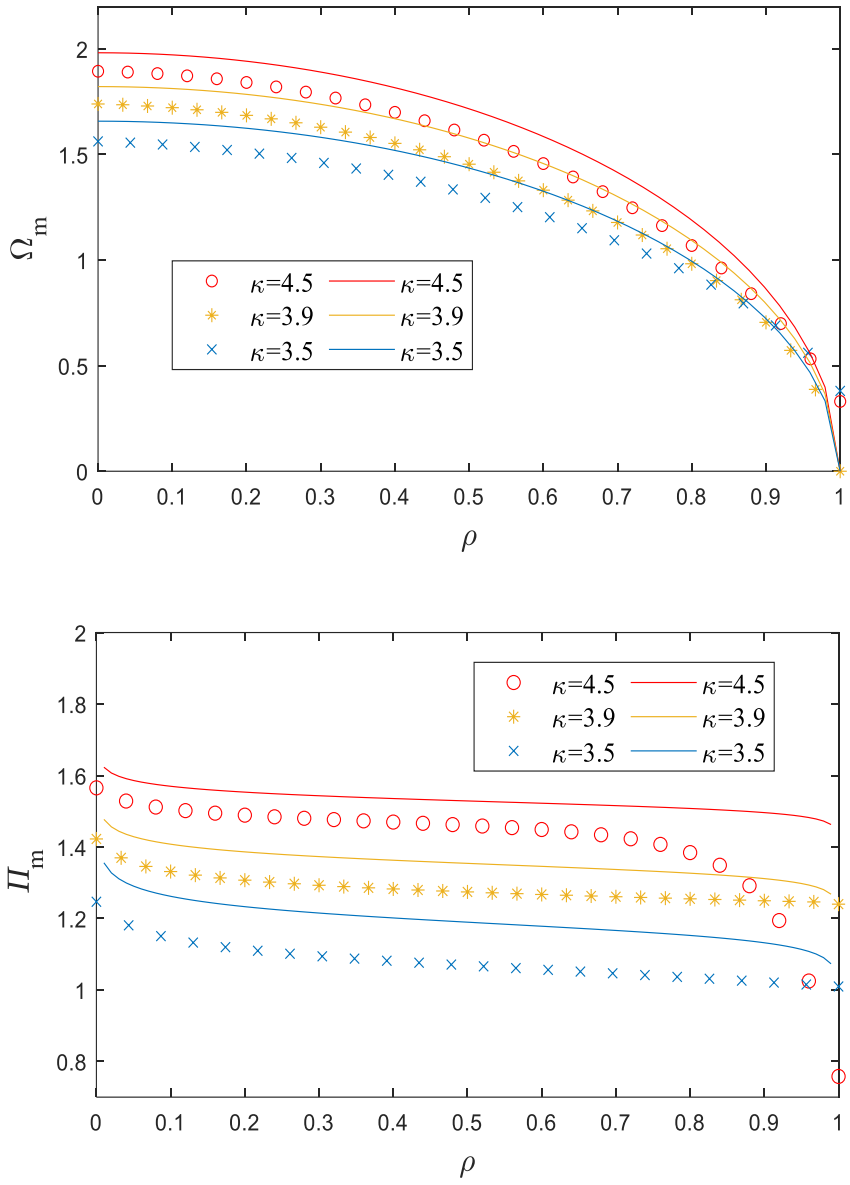


Figure 3.12: Comparison of the opening displacement and fluid pressure of analytical solution and numerical simulation given in the viscosity scaling for $\kappa = 3.5, 3.9, 4.5$

# Chapter 4

## Dislocation in anisotropic media

### 4.1 Introduction

The anisotropic elasticity theory of dislocations was developed several decades ago. Similar to the case of isotropic elasticity, the stress field of a dislocation line can be written as a line integral. Unfortunately, in general the explicit expression for the integrand does not exist, because there is no closed-form solution of the elastic Green function in generally anisotropic medium. In this chapter, we will focus on developing methods for actual calculations on the stress field of dislocations in anisotropic media. The emphasis will be on straight dislocation segment which is considered as the basic element in distributed dislocation technique.

Several methods are available for straight dislocations in anisotropic media. The classical theory is that of Eshelby et al. [48]. We will start with the work of Stroh [49], who reformulated and extended the classical theory to make it more convenient and powerful. On the basis of the Stroh eigenvector theory, one may develop an integral theory,

generalizing the work of Barnett and Swanger [50], which in some respects has advantages over the eigenvector theory. Then the stress field of dislocation segment and infinite dislocation line are given in the form of Brown [51] and Willis-steeds-Lothe formulae [52]. In the end of this chapter, the accuracy of the anisotropic formulas is compared with the analytical solution in isotropic case. Also, the analytical solution for penny-shaped fracture in the isotropy plane of TI material is used to verify the result of the planar fracture model incorporated with the anisotropic formula.

## 4.2 Statement of the problem

Consider an infinite homogeneous anisotropic linear elastic solid with elastic constants $C_{ijkl}$ relative to fixed crystal axes. Denote by $\boldsymbol{x}$ the position vector from the origin to a point in the medium and imbed a fixed triad of mutually orthogonal unit vectors $\boldsymbol{m}$, $\boldsymbol{n}$ and $\boldsymbol{t}$ in the solid (Figure 4.1). We seek displacement field solution $u_k$ to the equilibrium equations of elasticity which are independent of $\boldsymbol{t}$, i.e., we shall investigate a certain class of plane problem in which the elastic fields depend only on two orthogonal coordinates $\boldsymbol{m}$ and $\boldsymbol{n}$.

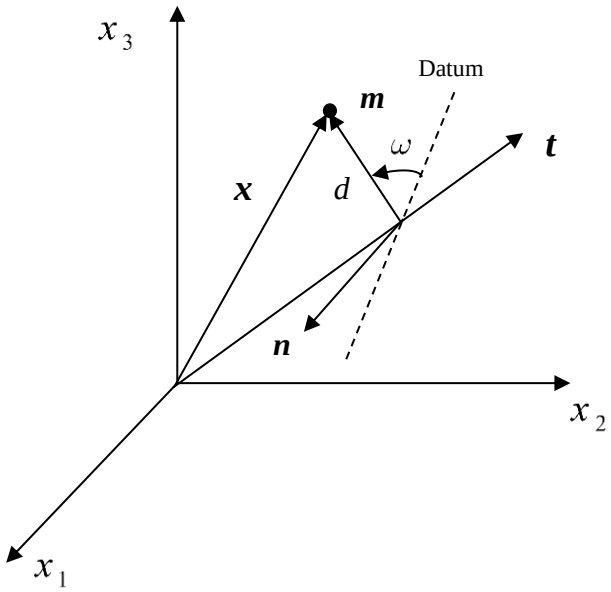


Figure 4.1: The relationship between ***m*-*n*-*t*** coordinate system

## 4.3 Stroh theory (The matrix formalism)

Infinite straight dislocations present a two-dimensional problem. Let ***m***, ***n*** and ***t*** be three mutually orthogonal unit vectors, and let ***t*** be the direction of the dislocation line perpendicular to the plane of the two-dimensional problem (see Figure 4.1).

In this problem, the displacements will not depend on the $\boldsymbol{t}\cdot\boldsymbol{x}$**,**

$$\boldsymbol{u}=\boldsymbol{u}\left(\boldsymbol{m}\cdot\boldsymbol{x},\boldsymbol{n}\cdot\boldsymbol{x}\right) \tag{4.1}$$

The displacement must satisfy the conditions of equilibrium:

$$\frac{\partial\sigma_{ij}}{\partial x_i}=0 \tag{4.2}$$

where $\sigma_{ij}=C_{ijkl}\dfrac{\partial u_k}{\partial x_l}$. (4.3)

Following Stroh [53] we assume a displacement field solution of the form:

$$\boldsymbol{u} = \boldsymbol{A}_\alpha f\left(\boldsymbol{m}\cdot\boldsymbol{x} + p_\alpha \boldsymbol{n}\cdot\boldsymbol{x}\right) \tag{4.4}$$

Where $\boldsymbol{A}_\alpha$ is a constant complex vector, $p_\alpha$ is a complex constant and $f$ is an analytic function of its argument. We seek conditions $\boldsymbol{A}_\alpha$ and $p_\alpha$ to ensure Eq. (4.4) is an admissible solution to Eq. (4.2). Thus, the secular equation

$$\left\{(mm) + p_\alpha\left[(mn)+(nm)\right] + p_\alpha^2(nn)\right\}\cdot\boldsymbol{A}_\alpha = 0 \tag{4.5}$$

must be fulfilled. Here, the matrices $(mm)$, $(mn)$, $(nn)$ etc. are defined as

$$(ab)_{jk} = a_i C_{ijkl} b_l \tag{4.6}$$

The requirements of a zero determinant in Eq. (4.5) gives six solutions for $p_\alpha$, in pairs of complex conjugates. Assuming for the moment that the six roots are distinct, corresponding to each $p_\alpha$ is an associated eigenvector $\boldsymbol{A}_\alpha$, apart from length, not yet specified. We can always arrange to order the eigenvalues $p_\alpha$ has a positive imaginary part for $\alpha = 1,2,3$ and a negative imaginary part for $\alpha = 4,5,6$ with

$$\left.\begin{aligned} p_{\alpha+3} &= p_\alpha^* \\ \boldsymbol{A}_{\alpha+3} &= \boldsymbol{A}_\alpha^* \end{aligned}\right\} \quad \alpha = 1,2,3 \tag{4.7}$$

Stroh [49] extended this three-dimensional formalism to a six-dimensional framework by introducing a second vector, related to $\boldsymbol{A}_\alpha$ as

$$\boldsymbol{L}_\alpha = -\left[(nm) + p_\alpha(nn)\right]\cdot\boldsymbol{A}_\alpha \tag{4.8}$$

which together with $\boldsymbol{A}_\alpha$ form a six-dimensional vector

$$\boldsymbol{\xi}_\alpha = \begin{pmatrix} \boldsymbol{A}_\alpha \\ \boldsymbol{L}_\alpha \end{pmatrix} \tag{4.9}$$

where $\boldsymbol{\xi}_\alpha$ is an eigenvector of the $6\times 6$ secular equation

$$N \cdot \boldsymbol{\xi}_\alpha = p_\alpha \boldsymbol{\xi}_\alpha \tag{4.10}$$

where *N* in block notation is

$$N = \begin{bmatrix} (nn)^{-1}(nm) & (nn)^{-1} \\ (mn)(nn)^{-1}(nm) - (mm) & (mn)(nn)^{-1} \end{bmatrix} \tag{4.11}$$

Since *N* is real, the six $p_\alpha$ and six $\boldsymbol{\xi}_\alpha$ each occur in three complex conjugate pairs. If the six $p_\alpha$ are distinct (as they are in the general case) then the six $\boldsymbol{\xi}_\alpha$ form a complete set of distinct eigenvectors. There do exist degenerate cases in which the $p_\alpha$ are not distinct: in isotropic media $p_\alpha = i\,(\alpha = 1,2,3)$ and $p_\alpha = -i\,(\alpha = 4,5,6)$ so that one must employ a mathematical extension in order to construct the appropriate complete set of eigenvector $\boldsymbol{\xi}_\alpha$. Such degeneracies shall not concern us here. These special cases may be treated by limiting the process described by Nishioka and Lothe [54]. In fact, in **Section 4.4** we shall develop an alternative formalism in which such degeneracies never appear.

$\boldsymbol{A}_\alpha$ and $\boldsymbol{L}_\alpha$ are selected to satisfy the following orthonormal relations:

$$\boldsymbol{A}_\alpha \cdot \boldsymbol{L}_\beta + \boldsymbol{A}_\beta \cdot \boldsymbol{L}_\alpha = \delta_{\alpha\beta} \tag{4.12}$$

The length of $\boldsymbol{A}_\alpha$ and the corresponding length of $\boldsymbol{L}_\alpha$ in Eq. (4.8) are normalized by

$$2\boldsymbol{A}_\alpha \cdot \boldsymbol{L}_\alpha = 1 \text{ (no summation over } \alpha) \tag{4.13}$$

Eq. (4.12) is the central result in the Stroh theory. The power of the Stroh scheme derives from this orthogonality relation.

In dislocation problems, and in line-force problems (an external force per unit length along an infinite straight line), the function *f* in Eq. (4.4) must be the logarithm. The multivalued of the logarithm is required for the Burgers circuit discontinuity and stresses inversely proportional with the distance from the line are what is required for line force. We seek a solution in the form of a superposition of partial solutions

$$\boldsymbol{u} = \frac{1}{2\pi i}\sum_{\alpha=1}^{6} D(\alpha)\boldsymbol{A}_{\alpha}\log\left(\boldsymbol{m}\cdot\boldsymbol{x} + p_{\alpha}\boldsymbol{n}\cdot\boldsymbol{x}\right) \tag{4.14}$$

Matching the many valued of $\boldsymbol{u}$ with the displacement discontinuity $\boldsymbol{b}$ in the Burger's circuit, we obtain the condition

$$\sum \pm D(\alpha)\boldsymbol{A}_{\alpha} = \boldsymbol{b} \tag{4.15}$$

And the requirement of balance with an external force f per unit length at the line leads to the condition

$$\sum \pm D(\alpha)\boldsymbol{L}_{\alpha} = -\boldsymbol{f} \tag{4.16}$$

where plus sign is used for $\alpha = 1, 2, 3$ and the minus sign is used for $\alpha = 4, 5, 6$, respectively. The six equations Eq. (4.15) and Eq. (4.16) determine $D(\alpha)$, and by means of the orthogonality relation, Eq. (4.12), the solution

$$D(\alpha) = \pm\boldsymbol{b}\cdot\boldsymbol{L}_{\alpha} - (\pm)\,\boldsymbol{f}\cdot\boldsymbol{A}_{\alpha} \tag{4.17}$$

is readily found. For a pure dislocation line, $\boldsymbol{f} = 0$ and $D(\alpha) = \pm\boldsymbol{b}\cdot\boldsymbol{L}_{\alpha}$. The dislocation solution must be

$$\boldsymbol{u} = \frac{1}{2\pi i}\sum_{\alpha=1}^{6}\left(\pm \boldsymbol{b}\cdot\boldsymbol{L}_{\alpha}\right)\boldsymbol{A}_{\alpha}\log(\boldsymbol{m}\cdot\boldsymbol{x} + p_{\alpha}\boldsymbol{n}\cdot\boldsymbol{x}) \tag{4.18}$$

From Eq. (4.18), the dislocation stress field is derived to be

$$\sigma_{ij} = \frac{1}{2\pi i}\sum_{\alpha=1}^{6}\pm A_{k\alpha}b_{m}L_{m\alpha}\frac{C_{ijkl}\left(m_{l} + p_{\alpha}n_{l}\right)}{\boldsymbol{m}\cdot\boldsymbol{x} + p_{\alpha}\boldsymbol{n}\cdot\boldsymbol{x}} \tag{4.19}$$

The ***Q***, ***B*** and ***S*** matrices can be expressed in terms of the normalized eigenvectors as

$$\begin{aligned} Q_{js} &= i\sum_{\alpha=1}^{6}\pm A_{j\alpha}A_{s\alpha} = 2i\sum_{\alpha=1}^{3}A_{j\alpha}A_{s\alpha} \\ B_{ij} &= i\sum_{\alpha=1}^{6}\pm L_{i\alpha}L_{j\alpha} = 2i\sum_{\alpha=1}^{3}L_{i\alpha}L_{j\alpha} \\ S_{ij} &= i\sum_{\alpha=1}^{6}\pm A_{i\alpha}L_{j\alpha} = i\left(2\sum_{\alpha=1}^{3}A_{i\alpha}L_{j\alpha} - \delta_{ij}\right) \end{aligned} \tag{4.20}$$

We shall show in the following section the matrices ***Q***, ***B*** and ***S*** can be calculated in a very simple way using numerical integration. It will turn out that most of the elastic solution of interest to us can be determined solely from a knowledge of ***Q***, ***B*** and ***S*,** so that we may entirely circumvent the need for solving the sextic eigenvalue problem originally posed by Stroh. The method of circumvention is termed 'the integral formalism' in order to distinguish it from Stroh technique.

## 4.4 The integral formalism

Because the matrix ***N*** given in Eq. (4.11) depends on the choice of the plane basis ***m*** and ***n***. For a two-dimensional problem, ***t*** is the only vector to be specified. We want to

determine the dependence of the $\boldsymbol{A}_\alpha$, $\boldsymbol{L}_\alpha$ and $p_\alpha$ on rotating the orthogonal vectors $\boldsymbol{m}$ and $\boldsymbol{n}$ by angle $\omega$ to the fixed datum $(\boldsymbol{m}_0, \boldsymbol{n}_0)$ in the plane (Figure 4.2).

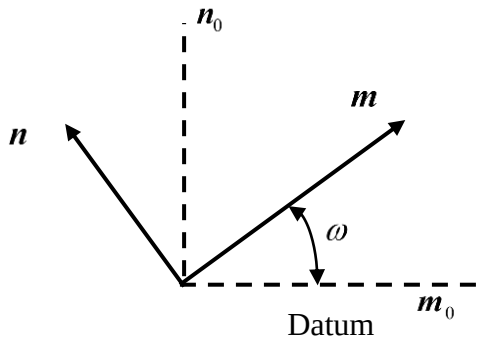


Figure 4.2: The angle $\omega$ defining $\boldsymbol{m}$ and $\boldsymbol{n}$ relative to the datum in the plane normal to $\boldsymbol{t}$

The matrices $\boldsymbol{Q}$, $\boldsymbol{B}$ and $\boldsymbol{S}$ can also be expressed in the integral formalism as [51,55]

$$Q_{js} = -\frac{1}{2\pi}\int_0^{2\pi} (nn)^{-1}_{js}\, d\omega$$

$$B_{ij} = \frac{1}{2\pi}\int_0^{2\pi} \left\{ (mm)_{ij} - (mn)_{ik} (nn)^{-1}_{kp} (nm)_{pj} \right\} d\omega \tag{4.21}$$

$$S_{ij} = \frac{1}{2\pi}\int_0^{2\pi} (nn)^{-1}_{ik} (nm)_{kj}\, d\omega$$

Thus, according to Eq. (4.21), direct integration of explicitly known $\omega$-dependent matrices is an alternative to finding the roots and eigenvectors of a sextic eigenvalue problem and the construction of matrices $\boldsymbol{Q}$, $\boldsymbol{B}$ and $\boldsymbol{S}$ by Stroh theory. Even though the matrix $\boldsymbol{N}$ and its eigenvectors $\boldsymbol{A}$ and $\boldsymbol{L}$ depend on the choices of $\boldsymbol{m}$ and $\boldsymbol{n}$, the matrices $\boldsymbol{Q}$, $\boldsymbol{B}$ and $\boldsymbol{S}$ only depend on the direction vector $\boldsymbol{t}$. This can be simply seen from the integral formalism.

## 4.5 Stress field of an infinite straight dislocation

Consider an infinitely long straight dislocation passing through the origin and parallel to the unit vector ***t*** (the dislocation direction vector), with Burgers vector ***b***. we are interested in its stress field at arbitrary field point ***x***. Choose two unit vectors ***m*** and ***n*** such that ***m***, ***n*** and ***t*** form a right-handed coordinate system and ***x*** is contained in the ***m***-***t*** plane, as shown in Figure 4.1. The stress field $\sigma_{ij}^{\infty}$ for an infinite straight dislocation line can be written as [55]

$$\sigma_{mn}^{\infty} = \frac{1}{d}\sum_{mn}\left(\boldsymbol{m},\boldsymbol{t},\boldsymbol{b}\right) \tag{4.22}$$

where the superscript $\infty$ indicates this is an infinite dislocation line, $\sum_{mn}$ is the angular stress factor and $d$ is the shortest distance from the field point ***x*** to the dislocation line. Following Barnett and Lothe [56], let $\boldsymbol{m}\cdot\boldsymbol{x} = d$ and $\boldsymbol{n}\cdot\boldsymbol{x} = 0$, the displacement gradients can be expressed as

$$\sum_{mn}\left(\boldsymbol{m},\boldsymbol{t},\boldsymbol{b}\right) = \frac{1}{2\pi}C_{mnip}b_s\left\{-m_pS_{ki} + n_p\left(nn\right)_{ik}^{-1}\left[B_{ks} + \left(nm\right)_{kr}S_{rs}\right]\right\} \tag{4.23}$$

***B*** and ***S*** are the matrices that can be evaluated using the matrix formalism and the integral formalism from **section 4.3** and **section 4.4**.

Alternatively, we can compute the stress field from the displacement gradient

$$\sigma_{ij}^{\infty}\left(\boldsymbol{x},\boldsymbol{t},\boldsymbol{b}\right) = C_{ijkl}u_{k,l}\left(\boldsymbol{x},\boldsymbol{t},\boldsymbol{b}\right) \tag{4.24}$$

Willis-Steed-Lothe [51] formula for displacement gradient of an infinitely long dislocation line is

$$\frac{\partial u_m}{\partial x_s} = \frac{1}{2\pi d}\varepsilon_{jsn} b_i C_{ijkl} t_n \left\{ -m_l Q_{mk} + n_l \left[ (nn)^{-1} (nm) Q \right]_{mk} + n_l \left[ (nn)^{-1} S^T \right]_{mk} \right\} \tag{4.25}$$

where $\varepsilon_{jsn}$ is permutation tensor. Eq. (4.22) with Eq. (4.23) and Eq. (4.24) with Eq. (4.25) are equivalent and give identical numerical results.

The stress field of isotropic material is used to test the accuracy of the anisotropic WSL formula for infinite dislocation line. The distribution of stress components calculated by anisotropic and isotropic equations (see **Appendix C** and [51]) in the plane perpendicular to the straight dislocation is shown in Figure 4.3 and Figure 4.4. All computations are performed for the stress field of an infinite dislocation line passing through the origin along ***t*** = [1 2 3] direction with the Burger vector ***b*** = [1 0.5 2] in isotropic material where $E = 30\text{GPa}$ and $\nu = 0.2$. The stress components have the singularity (infinite value) at the dislocation line.

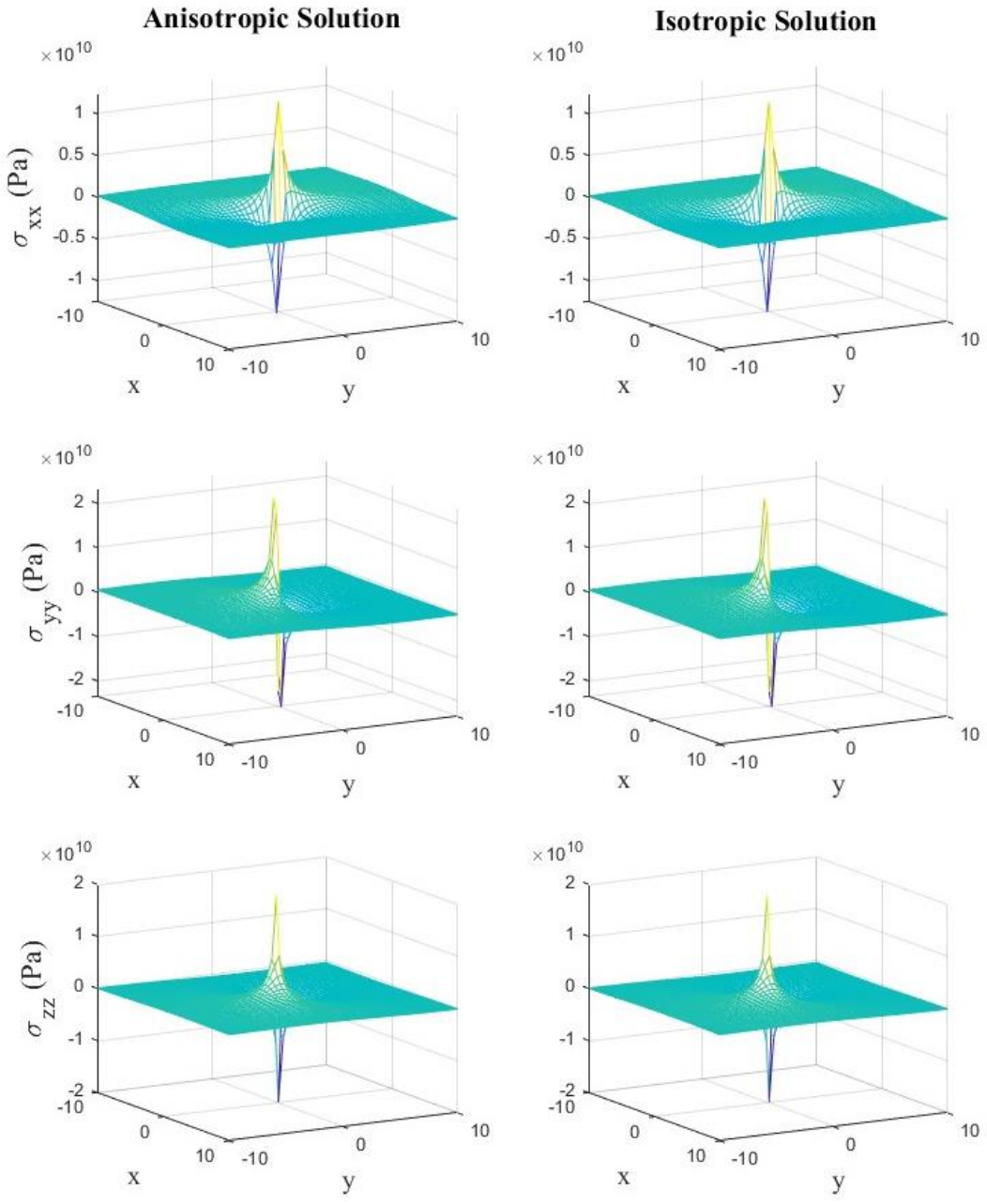


Figure 4.3: Comparison results of the stress components ($\sigma_{xx}, \sigma_{yy}, \sigma_{zz}$) in isotropic material ($E = 30\text{GPa}$ and $\nu = 0.2$) using isotropic and anisotropic equations

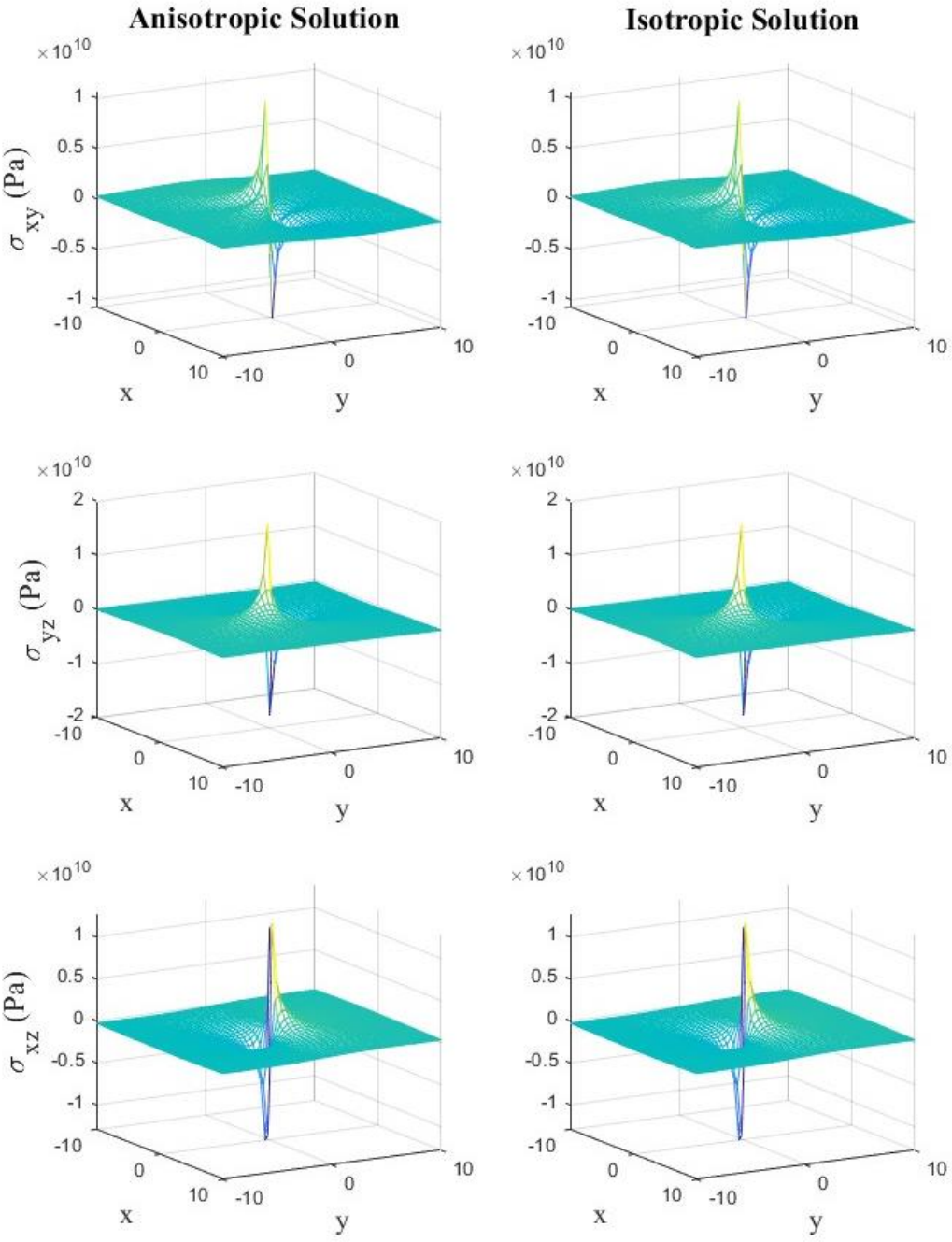


Figure 4.4: Comparison results of the stress components ($\sigma_{xy}, \sigma_{yz}, \sigma_{xz}$) in isotropic material ($E = 30\text{GPa}$ and $\nu = 0.2$) using isotropic and anisotropic equations

## 4.6 Stress field of a finite dislocation segment

**Brown's formula**

Brown developed a two-dimensional theorem to evaluate the stress field of an arbitrary dislocation configuration where the field point and the dislocation line are coplanar. Then the stress field of a general dislocation in three-dimension was first developed by Indenbom and Orlov [51]. Based on Brown-Indenbom-Orlov theory, an alternative derivation with simpler expressions was given by Asaro and Barnett where the resultant stress field for a given dislocation segment is expressed in terms of angular stress factor and its derivative for infinite dislocation line.

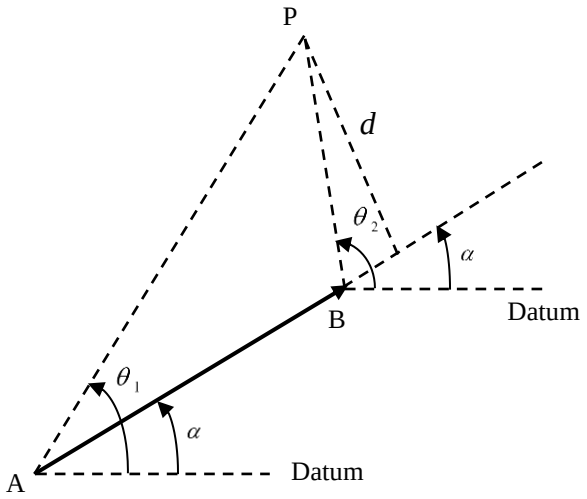


Figure 4.5: The geometry pertinent to Brown's formula. Consider a plane containing the straight segment AB and the field point P. $\alpha$ is the angle between the segment AB and an arbitrary datum in the same plane. $\theta_1$ and $\theta_2$ measure the orientations of line AP and line BP, relative to the datum, respectively.

The stress field of a finite and straight dislocation segment **AB** at point **P,** as specified in Figure 4.5 can be expressed as [57]

$$\sigma_{ij} = \frac{1}{2d}\left[-\cos(\theta-\alpha)\sum_{ij}(\theta) + \sin(\theta-\alpha)\sum'_{ij}(\theta)\right]\Big|_{\theta_1}^{\theta_2} \tag{4.26}$$

where $\sum_{ij}$ is the angular stress factor of an infinite straight along **AP** or **BP**. $\sum'_{ij}$ is its derivative with respect to the angle $\theta$ and can be expressed in terms of angular derivatives of $\boldsymbol{B}$ and $\boldsymbol{S}$.

$$\begin{aligned}\frac{\partial \sum_{mn}}{\partial\theta} = \frac{1}{2\pi} C_{mnip} b_s \Bigg\{ & t_p S_{is} - \frac{\partial t_p}{\partial\theta}\frac{\partial S_{is}}{\partial\theta} \\ & + n_p (nn)^{-1}_{ik}\left[\frac{\partial B_{ks}}{\partial\theta} + \left(n\frac{\partial t}{\partial\theta}\right)_{kr}\frac{\partial S_{rs}}{\partial\theta} - (nt)_{kr} S_{rs}\right]\Bigg\}\end{aligned} \tag{4.27}$$

Expressions for angular derivatives of matrices $\boldsymbol{Q}$, $\boldsymbol{B}$ and $\boldsymbol{S}$ are given in **Appendix B**. It is easy to show that as the length of the segment goes to infinity, $\theta_1 \to \alpha$ and $\theta_2 \to \alpha + \pi$, Eq. (4.26) reduces to the stress field of an infinite dislocation line given by Eq. (4.22). Unlike the stress field of an infinite dislocation line, the stress field of a finite dislocation segment is not unique. The case of P colinear with segment **AB** but not on **AB** requires special attention because $d = 0$ and Brown's formula gives zero in this case.

**Willis-Steed-Lothe formula**

The stress field of a finite segment can also be obtained through the Willis-Steeds-Lothe (WSL) formula for the displacement gradient (see Figure 4.6).

$$\frac{\partial u_m}{\partial x_s} = \frac{1}{4\pi d}\varepsilon_{jsn} b_i C_{ijkl} t_n \left\{ -m_l Q_{mk} + n_l \left[ (nn)^{-1} (nm) Q \right]_{mk} + n_l \left[ (nn)^{-1} S^T \right]_{mk} \right\}\Bigg|_{AP}^{BP} \tag{4.28}$$

As mentioned before, the WSL formula can give a different stress field from Brown's formula for a dislocation segment. But two formulas become equivalent for a complete dislocation loop or an infinite dislocation line. According to the work of the Yin and Barnett [57], the WSL formula is more convenient because it avoids the calculation of derivative of angular stress factor $\sum'$, which would require evaluation using a more cumbersome formula. It is easy to show that as the length of the segment goes to infinity, Eq. (4.28) reduces to the Eq. (4.25).

Unlike the case of Brown's formula, the stress field using the Willis-Steed-Lothe formula is non-zero in the colinear limit $d$ = 0 (with the field point not on the segment). The displacement gradient in the colinear limit is

$$\left.\frac{\partial u_m}{\partial x_s}\right|_{d\to 0} = \frac{1}{4\pi}\left(\frac{1}{r_2} - \frac{1}{r_1}\right)\varepsilon_{jsn} b_i C_{ijkl} t_n \left\{ t_l Q_{mk} - m_l \frac{\partial Q_{mk}}{\partial \theta} + n_l \left[ (nn)^{-1}(-nt) Q + (nn)^{-1}(nm)\frac{\partial Q}{\partial \theta} + (nn)^{-1}\frac{\partial S^T}{\partial \theta} \right]_{mk} \right\} \tag{4.29}$$

where $r_1 = |\boldsymbol{AP}|$ and $r_2 = |\boldsymbol{BP}|$, as $d \to 0$, the angular derivatives of the matrices $\boldsymbol{Q}$ and $\boldsymbol{S}$ are required and can be obtained from **Appendix B**.

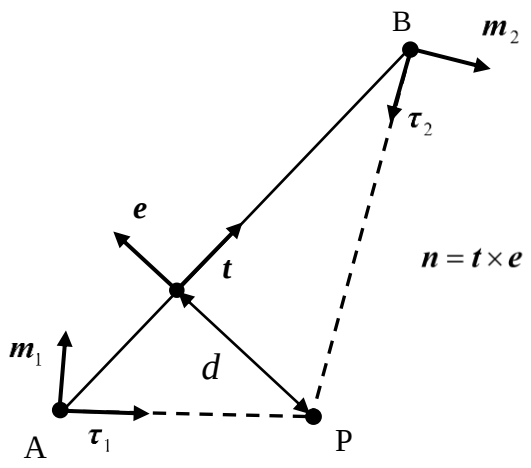


Figure 4.6: The geometry of the WSL formula

Since the stress field of a finite dislocation segment is not unique, it makes no sense for us to compare the stress field of a single dislocation segment. Thus, we add a sequence of dislocation segments along a specific direction ***t*** and compare it with an infinite dislocation line in transversely isotropic material (Opalinius Clay, see Table 2.1), which is given in Figure 4.7 and Figure 4.8. An infinite straight dislocation is along ***t*** = [1 2 3] with Burger's vector ***b*** = [1 0.5 2]. 100 dislocation segments are used to discretize this straight dislocation line and each of them are with 10 meters of length. Stress field of infinite straight dislocation and superposition of dislocation segments are compared in the plane perpendicular to the dislocation line. Also, in Figure 4.9, since our 3D planar hydraulic model is constructed by prismatic square dislocation loops, we will compare the result of the stress component $\sigma_{zz}$ by adding four dislocation segments of square elements with the isotropic solution, Eq. (3.11), in isotropic material.

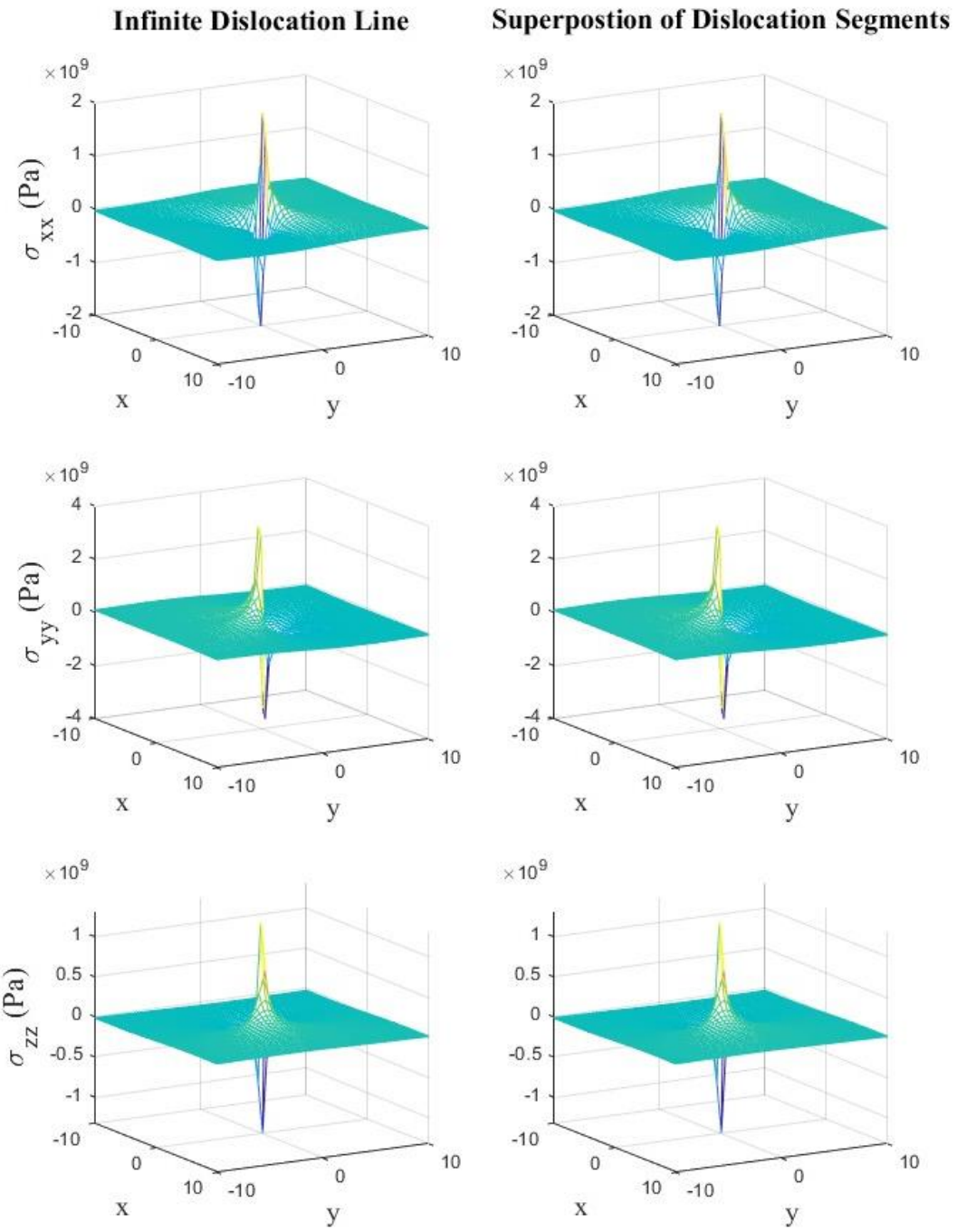


Figure 4.7: Comparison results of the stress components ( $\sigma_{xx}, \sigma_{yy}, \sigma_{zz}$ ) between an infinite dislocation line and superposition of dislocation segment in TI material (Opalinius Clay)

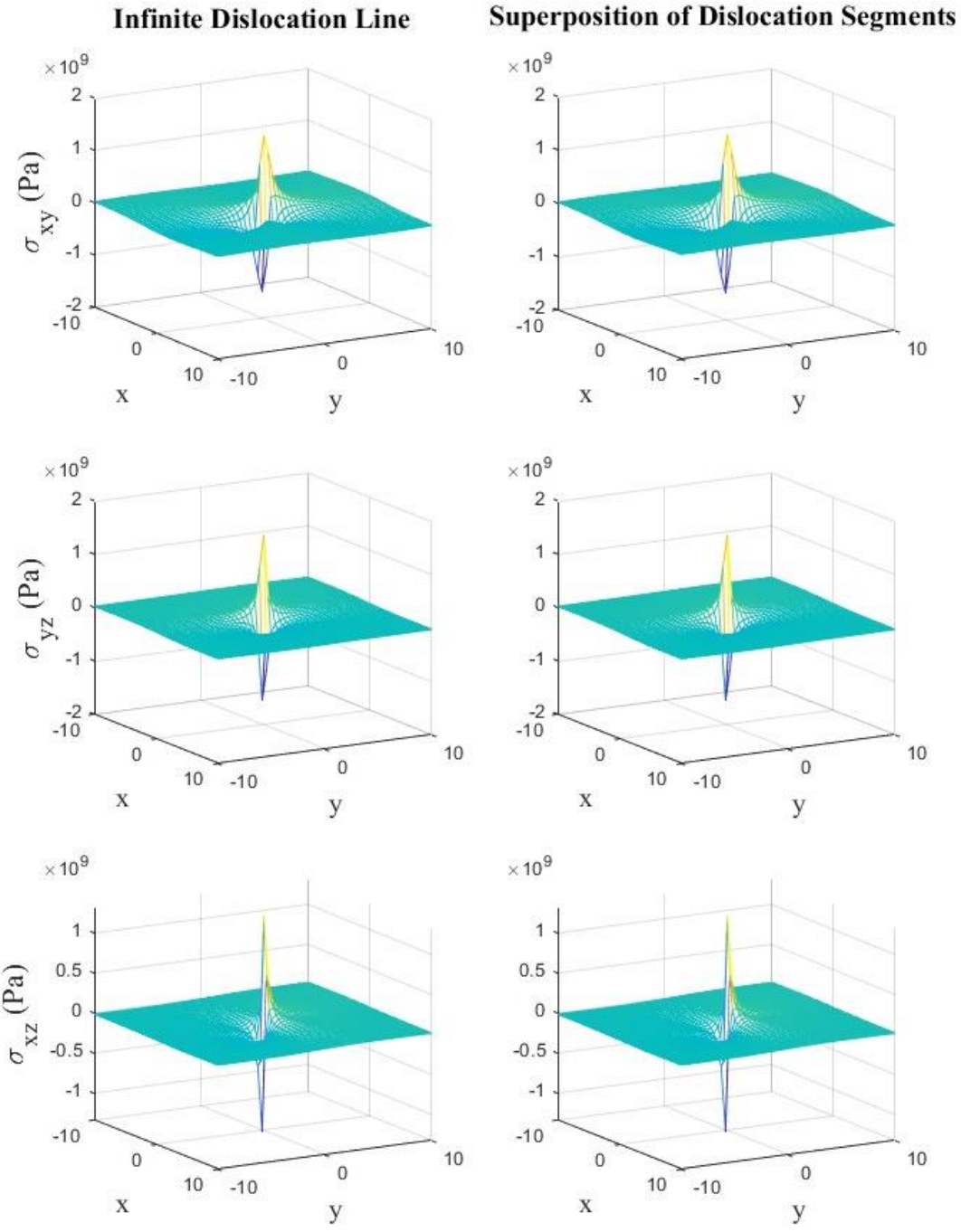


Figure 4.8: Comparison results of the stress components ( $\sigma_{xx}, \sigma_{yy}, \sigma_{zz}$ ) between an infinite dislocation line and superposition of dislocation segments in TI material (Opalinius Clay)

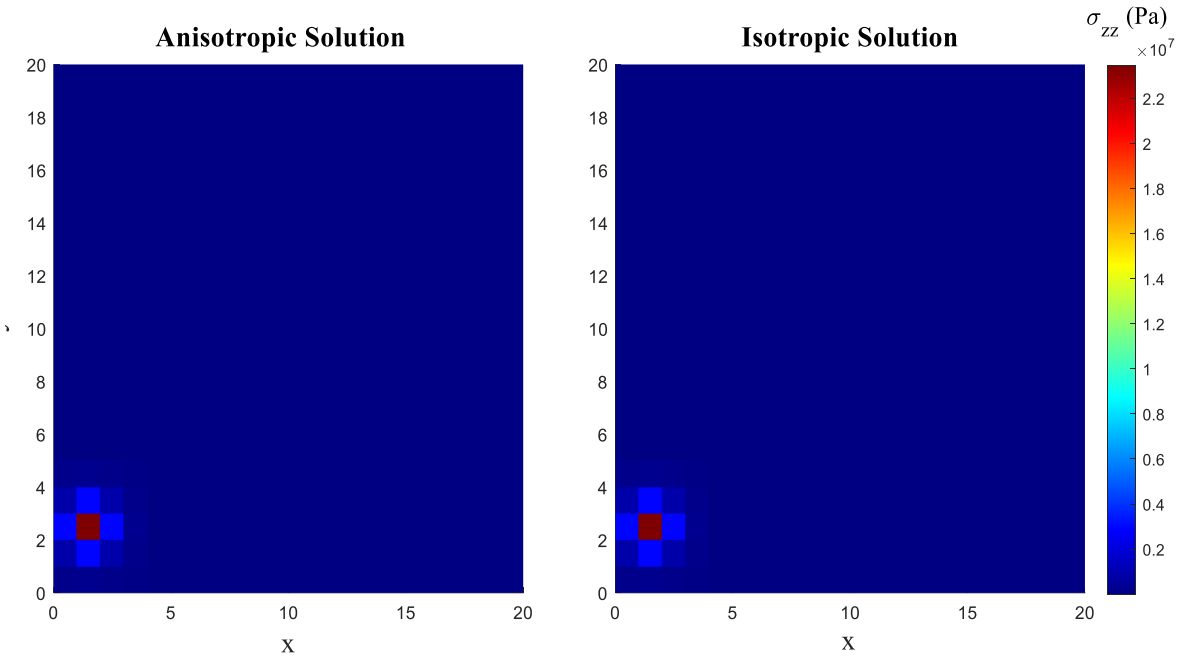


Figure 4.9: Stress field ( $\sigma_{zz}$ ) of a prismatic square dislocation loop using the anisotropic formula and isotropic solution

## 4.7 Penny-shaped crack in infinite transversely isotropic medium

The penny-shaped crack in the unbounded transversely isotropic solid is selected to demonstrate the accuracy of the anisotropic formula. In this configuration, the crack plane is located to coincide with the plane of isotropy ( $x_1 - x_2$ ) of the transversely isotropic material. Let $x_3$ be the axis of material symmetry (Figure 4.10). The crack surfaces are subjected to the uniform fluid pressure $p_0$ . The solution to this problem is summarized in the work of the Sih and Chen [58].

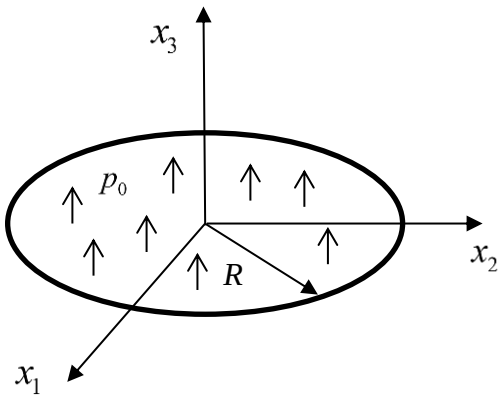


Figure 4.10: Penny-shaped fracture under uniform pressure in transversely isotropic medium

The opening displacement of the crack is

$$u_3 = \frac{4Ap_0}{\pi}\sqrt{R^2 - r^2} \tag{4.30}$$

Where $A = \mathrm{Re}\left\{\dfrac{c_{11}\left(c_{13}+c_{44}\right)\left(n_1^{1/2}+n_2^{1/2}\right)}{c_{44}\left(c_{13}+c_{11}n_1\right)\left(c_{13}+c_{11}n_2\right)}\right\}$; $n_1$ and $n_2$ are the roots of the quadratic equation:

$$c_{11}c_{44}n^2 + \left[c_{13}\left(c_{13}+2c_{44}\right) - c_{11}c_{33}\right]n + c_{33}c_{44} = 0 \tag{4.31}$$

The comparison of the fracture width between the analytical solution, in Eq. (4.30) and anisotropic result (WSL formula) is shown in Figure 4.11. The anisotropic equation can give a very accurate result on the fracture width in radial direction with only about 3% error at the crack center. This comparison displays an accurate result of the anisotropic formula implemented in the fracture model.

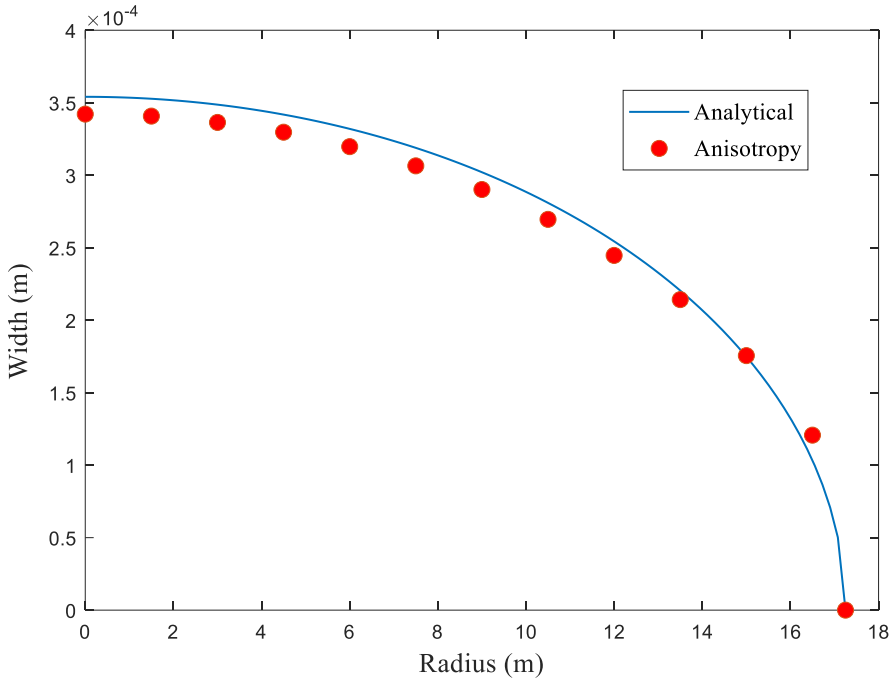


Figure 4.11: Comparison of the anisotropic solution and analytical solution for the penny-shaped fracture in isotropy plane of the Transversely isotropic material

# Chapter 5

## Propagation of a PL3D hydraulic fracture in transversely isotropic rock

### 5.1 Abstract

The configuration of a hydraulic fracture propagating perpendicular to the isotropy plane of a transversely isotropic material is encountered in many sedimentary rocks. We investigate fracture growth driven by the injection of a Newtonian fluid at a constant rate from a point source. Anisotropic distributed dislocation technique is used to compute the stress field in transversely isotropic (TI) material. The direction-dependent elastic modulus $B$ is used in fracture energy propagation criterion and the near- tip solution to compute the local stress intensity factor. The ratio $\beta$ of elastic modulus in horizontal direction and vertical direction is defined to quantify the elastic anisotropy in TI material. The evolution of the fracture in different TI rocks is displayed for showing the impact of the material anisotropy. Different ratios of the engineering elastic parameters ( $E_1/E_3$ , $G_1/G_3$ , $\nu_1/\nu_3$ ) in TI material are tested to capture the specific influence parameters in material anisotropy

and final fracture geometry (aspect ratio and fracture width). We also confirm that the fracture energy (material toughness) plays a crucial role in fracture propagation. The elongations of the fracture can be affected significantly by the energy release rate $G_c$. Moreover, different isotropic average algorithms are compared for the accuracy of the approximations on fracture shapes in TI material. Voigt scheme gives the best estimation in a broad range of the $\beta$ and horizontal parameters ($E_1$, $\nu_1$) work good in some particular cases.

## 5.2 Introduction

Hydraulic fracturing is a well-established technique to stimulate oil and gas. In this well stimulation technique, a high-pressure fluid is injected into a reservoir to fracture hydrocarbon-bear rocks. Thus, it increases the flow of oil or gas. [59].

Transverse isotropy is a common feature in sedimentary rocks due to the deposition and compacting processes. In particular, the reservoirs are composed of beds of metric and sub-metric scales. Such a lamination yields the layered structure, which is known as the transversely isotropic medium. Based on these characteristics of the formation, we model the growth of planar three-dimensional (PL3D) fluid-driven fracture (**Chapter 3**) perpendicular to the isotropic plane and minimum in-situ horizontal stress [60]. This configuration notably corresponds to the case where the rock layers are horizontal and fracture propagates vertically (see Figure 5.1). In the presence of weak bedding planes (isotropy plane), the fracture may deviate from the vertical direction resulting in T-shape

like geometries [61]. We don't account for this possibility and only focus on the case where fracture grows in single plane perpendicular to the material isotropy. The anisotropy effect is first investigated numerically on 2D plane strain hydraulic fracture by many publications [62, 63]. The aspect ratio of the 3D hydraulic fracture in TI material is studied in the work of Bessmertnykh and Dontsov [64] based on the Hoenig [65] solution assuming the elliptical crack. The impact of toughness anisotropy is accounted for fracture propagation in different dominated regimes by Zia [66]. And then Moukhtari [67] extended the previous model to quantify how these dimensionless anisotropic elastic parameters can influence the fracture shape in different propagation regimes.

In this chapter, we first briefly recall the formulation of the planar 3D hydraulic fracture and explain how the anisotropic effect can be incorporated in to the PL3D model. The elastic modulus $B$ is extracted from the Irving matrix which relates the fracture energy to the stress intensity factor. And as in previous discussion, this $B$ can be obtained from numerical integration or solving an eigenvalue problem. Particularly, in the configuration shown in Figure 5.1. The exact solution of the elastic modulus $B$ in horizontal and vertical direction is given in terms of the elastic constants. The engineering elastic parameters are used to represent the TI material and the effect of these parameters is analyzed by comparing the corresponding results of the fracture geometry. Then we investigate the impact of the fracture toughness (or fracture energy) on the elongation of the fracture. In the last part of this chapter, we introduce the average algorithm to approximate the fracture geometry in TI material. The validity and accuracy of different methods is discussed.

## 5.3 Problem Formulation

We consider a 3D planar hydraulic fracture in transverse isotropic impermeable media, propagating in a plane perpendicular to the isotropy plane and normal to direction of the minimum in-situ stress $\sigma_h$ (see Figure 5.1). We introduce an orthogonal coordinate $(x_1, x_2, x_3)$ where $x_3$ is the axis of symmetry and $(x_1, x_2)$ is the plane of material isotropy. The transversely isotropic elastic tensor $C_{ijkl}$ can be expressed in terms of five elastic parameters $(C_{11}, C_{12}, C_{13}, C_{33}, C_{44})$ in Voigt notation. We focus on the case of the vertical hydraulic fracture subjected to an internal fluid pressure $p_f$ by the injection of Newtonian fluid at a constant rate from a point source.

### 5.3.1 Elasticity Theory

Under the configuration of Figure 5.1, the planar fracture exhibits a pure opening mode (model I). The elasticity equation relates the displacement discontinuity (see **section 3.3**) across the fracture and the internal fluid pressure inside the fracture.

$$p_f(x_1, x_3, t) - \sigma_h = \int_{A(t)} T(x_1, x_3, \zeta, \eta) w(\zeta, \eta, t) d\zeta d\eta \tag{5.1}$$

Where $A(t)$ denotes the fracture footprint, $p_f$ is the fluid pressure inside the fracture, $\sigma_h$ is the minimum in-situ stress and *w* is the fracture width. Influence function $T(x_1, x_3, \zeta, \eta)$ represents the normal elastic stress at point $(x_1, x_3)$ due to a unit displacement discontinuity

at point $(\zeta, \eta)$ at given time *t*. *T* can be obtained by adding the stress field of dislocation segments discretized in the fracture domain in transversely isotropic material [51, 55].

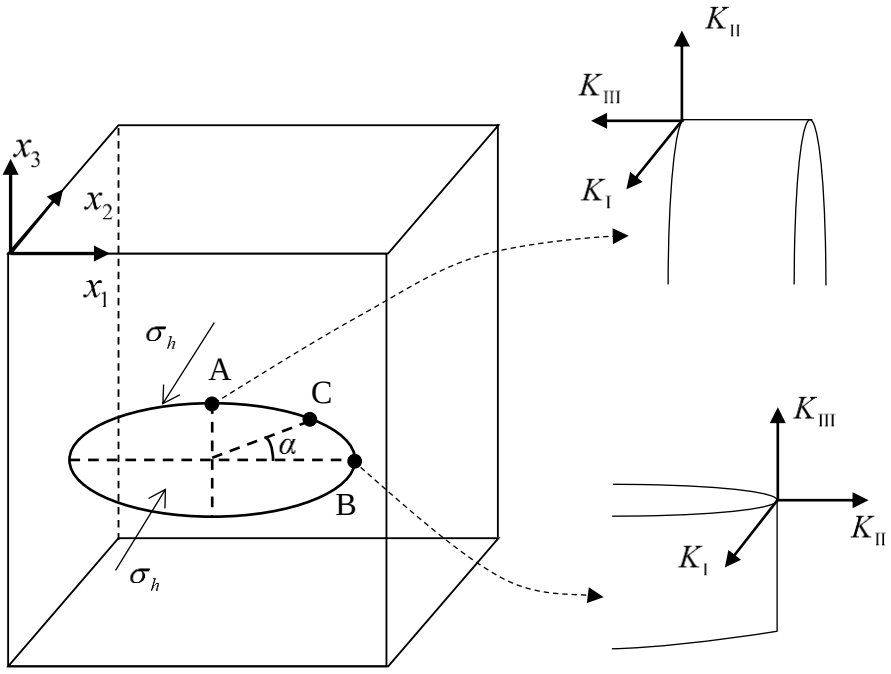


Figure 5.1: Schematic of a planar 3D hydraulic fracture propagating in a transverse isotropic medium perpendicular to the isotropy plane $(x_1, x_2)$ and normal to the direction of the minimum in-situ stress. Point A $(\alpha = \pi/2)$ and B $(\alpha = 0)$ are fracture fronts along vertical direction and horizontal direction. $K_i$ is the direction of the local stress intensity factor corresponding to different fracture mode

### 5.3.2 Fluid flow inside the fracture

The fluid flow inside the fracture follows lubrication theory which is explained in **section 3.4**. Under the assumption of Newtonian fluid flowing in the fracture plane ( $x_1 - x_3$ ), the width averaged fluid mass conservation equation reduces to following form:

$$\frac{\partial w}{\partial t} + \nabla \cdot \boldsymbol{q} = Q_0 \delta(x_1, x_3) \tag{5.2}$$

where $\nabla = \left(\partial/\partial x_1, \partial/\partial x_3\right)$, $Q_0$ denotes the constant injection rate located at the origin, the fluid flux $\boldsymbol{q}$ is related to the fluid pressure gradient and fracture opening via Poiseuille's law.

$$\boldsymbol{q} = -\frac{w^3}{12\mu_f} \nabla \cdot p_f \tag{5.3}$$

where $\mu_f$ is the fluid viscosity. Zero fluid flux at fracture front is implemented as boundary condition in Eq. (5.2).

### 5.3.3 Fracture propagation conditions

The fracture energy criterion is used as the fracture propagation condition (**section 3.5.2**), which is given in Eq. (5.4).

$$G_e = \frac{1}{2} K_i B_{ij}^{-1} K_j \qquad i, j = 1, 2, 3 \tag{5.4}$$

In the configuration we investigate here the planar fracture is perpendicular to the isotropy plane of a transversely isotropic material, the fracture mode decouples and as a result the $B_{22}$ is an only nonzero element in the matrix of elastic modulus $B_{ij}$. Thus, Eq. (5.4) can be rewritten as

$$G_e = \frac{K_2^2}{2B_{22}} = \frac{K_I^2}{2B(\alpha)} \tag{5.5}$$

where $B_{22} = B(\alpha)$ is a near-tip elastic modulus which depends on the angle $\alpha$ between the local direction of the fracture front and material axis $x_1$. The exact expressions of $B(\alpha)$ along the horizontal axis $x_1$ ($\alpha = 0$) and vertical axis $x_3$ ($\alpha = \pi/2$) can be derived as [68]

$$B^{-1}(\alpha = 0) = B_1^{-1} = \frac{2C_{11}}{C_{11}^2 - C_{12}^2} \tag{5.6}$$

$$B^{-1}(\alpha = \pi/2) = B_3^{-1} = \sqrt{\frac{C_{33}}{C_{11}C_{33} - C_{13}^2}\left(\frac{1}{C_{44}} + \frac{2}{C_{13} + \sqrt{C_{11}C_{33}}}\right)} \tag{5.7}$$

Alternatively, as we mentioned previously, for arbitrary direction of the fracture front, $B(\alpha)$ can be computed by numerical integral or solving an eigenvalue problem (see **section 4.3** and **4.4** for details). In order to quantify the degree of the elastic anisotropy, we use the ratio between the horizontal elastic modulus and vertical elastic modulus $\beta = B_1/B_3$. According to the Eq. (5.4), quasi-static linear elastic fracture mechanics propagation condition ($G_e = G_c$) can alternatively be written as the equality of mode I stress intensity factor with the material fracture toughness $K_{Ic}$. We will investigate the case where material shows elastic transverse isotropy but critical fracture energy $G_c$ is isotropic anywhere. In other words, the fracture toughness of the material may also vary depending on the local fracture front propagation direction. As a result, the propagation condition for a hydraulic fracture perpendicular to the isotropy plane of transversely isotropic material can be written as

$$K_I(\boldsymbol{x}_\Omega, t) = K_{Ic}(\alpha),\ \boldsymbol{x}_\Omega \in \Omega(t) \tag{5.8}$$

for all point $\boldsymbol{x}_{\Omega}$ along the fracture front $\Omega$ with a local propagation direction defined by the angle $\alpha$. The near-tip asymptotic solution in the anisotropic solid is implemented to capture the local stress intensity factor at the fracture front [46]

$$w = 4B^{-1}K_{\mathrm{I}}\left(\frac{r}{2\pi}\right)^{1/2} \tag{5.9}$$

where *r* is the closest distance to the fracture front in the propagation direction.

## 5.4 Numerical Solution

The fracture plane is discretized using a Cartesian grid consisting of uniform rectangular elements (see Figure 5.2). We discretize elasticity Eq. (5.1) based on rectangular displacement discontinuity elements. The distributed dislocation method is used to determine the stress field of a rectangular element by adding the stress field of each side of this element (see **section 4.6**). The fracture width is thus constant over a cell and the fluid pressure is evaluated at the cell center. The lubrication flow is discretized spatially with finite volume method and a forward Euler scheme for time integration. The propagation algorithm relies on the local stress intensity factor computed in the crack tip element using Eq. (5.9). In the case of a transversely isotropic material, the fracture toughness in different directions needs to be calculated by Eq. (5.5) for the given critical energy release rate as the propagation criterion.

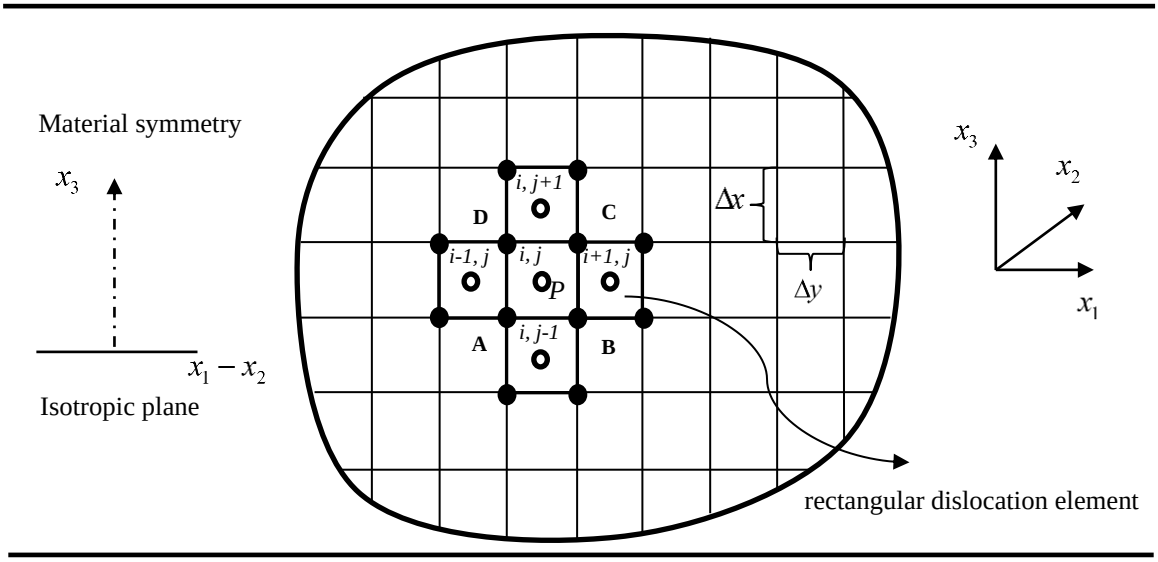


Figure 5.2: Schematics of the finite discretization of the fracture plane. The rectangular displacement discontinuity element is used. The piece-wise constant fracture width and fluid pressure are evaluated at element center

## 5.5 Anisotropic effect on fracture geometry

### 5.5.1 Anisotropic effect on the transversely isotropic rock

In this section, we select 6 different transversely isotropic rocks which can demonstrate different anisotropy (from weak to strong) from Table 2.1. The evolutions of PL3D fractures in different rocks are illustrated to show the anisotropic impact of the material. The ratio of elastic moduli $\beta$ for each rock is computed in Table 5.1. The corresponding engineering parameters of these rocks are given in Table 5.2 and the simulation parameters we use are as follows:

Critical energy release rate $G_c = 50\,\mathrm{J/m^2}$; $\mu_f = 0.02\ \mathrm{Pa \cdot s}$; $Q_0 = 0.05\,\mathrm{m^2/s}$; $\sigma_h = 10\ \mathrm{MPa}$ and injection time $t_{inj} = 3000\mathrm{s}$.

Table 5.1: Example of elastic stiffness coefficient (Voigt notation) of different transversely isotropic (TI) rocks (all values in GPa).

| | $C_{11}$ | $C_{33}$ | $C_{12}$ | $C_{13}$ | $C_{44}$ | $\beta$ |
|---|---|---|---|---|---|---|
| Olkiluoto mica gneiss | 89.7 | 65.9 | 22.2 | 23.5 | 24 | 1.16 |
| Gas-saturated Shaly Coal | 22.1 | 10.9 | 8.36 | 1.2 | 3.7 | 1.26 |
| Woodford53 shale | 28 | 17.3 | 7.5 | 8.3 | 5.6 | 1.31 |
| Opalinius Clay | 57.6 | 28.8 | 54.6 | 38.7 | 0.9 | 1.33 |
| Yeocheon schist | 91.4 | 27.6 | 33.7 | 20 | 13.7 | 1.43 |
| Calcareous mudstone | 90.4 | 35.1 | 51.6 | 39.8 | 6.5 | 1.9 |

Table 5.2: Values of engineering elastic parameters corresponding to the different rocks given in Table 5.1 ($E_1$, $E_3$, $G_3$ are in GPa)

| | $E_1$ | $E_3$ | $\nu_1$ | $\nu_3$ | $G_3$ |
|---|---|---|---|---|---|
| Olkiluoto mica gneiss | 78.9 | 56.0 | 0.17 | 0.21 | 24 |
| Gas-saturated Shaly Coal | 18.9 | 10.8 | 0.37 | 0.04 | 3.7 |
| Woodford53 shale | 23.5 | 13.4 | 0.15 | 0.23 | 5.6 |
| Opalinius Clay | 4.39 | 2.10 | 0.46 | 0.35 | 0.9 |
| Yeocheon schist | 72.1 | 21.2 | 0.25 | 0.16 | 13.7 |
| Calcareous mudstone | 44.3 | 12.8 | 0.14 | 0.28 | 6.5 |

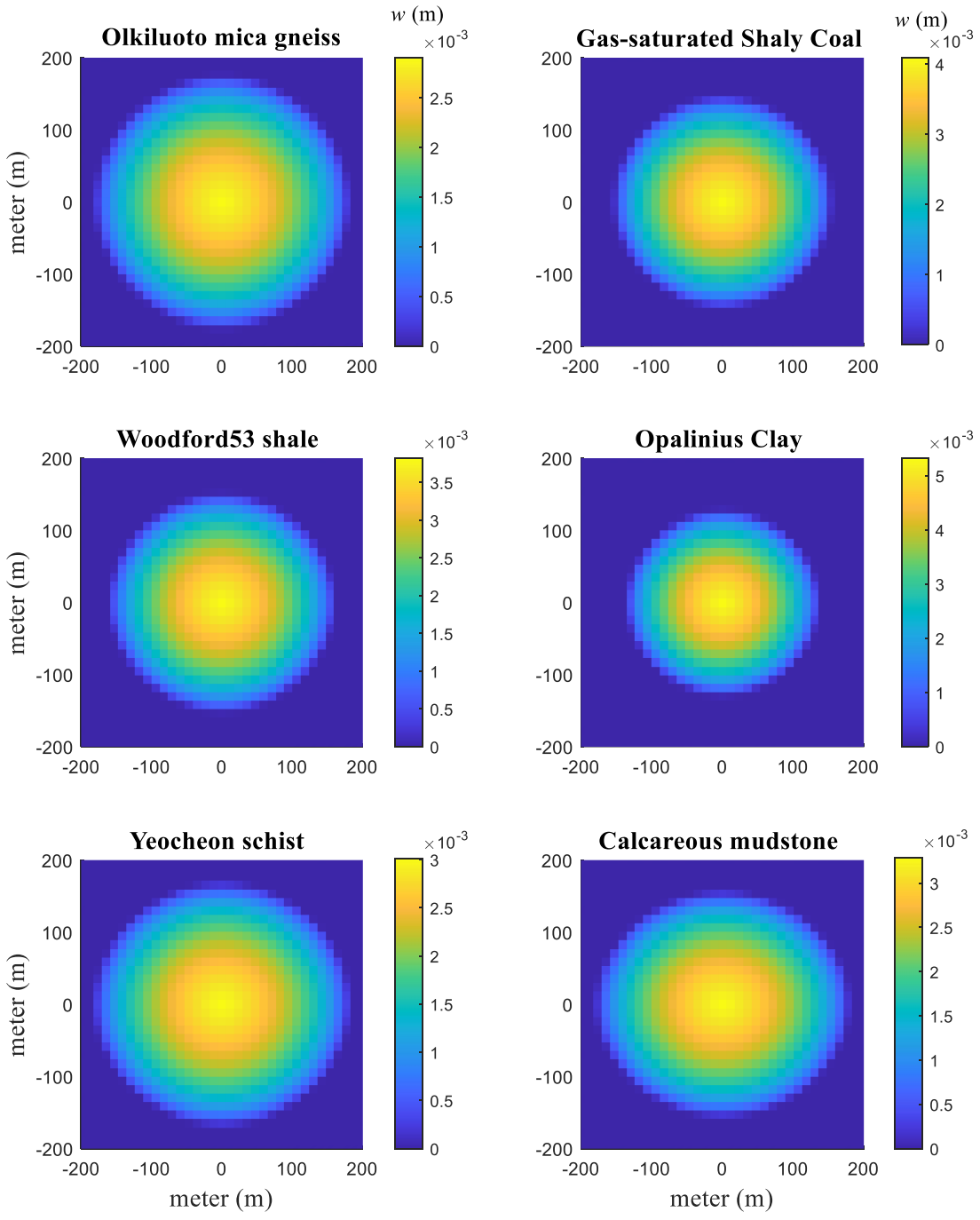


Figure 5.3: Fracture geometry in transversely isotropic rocks

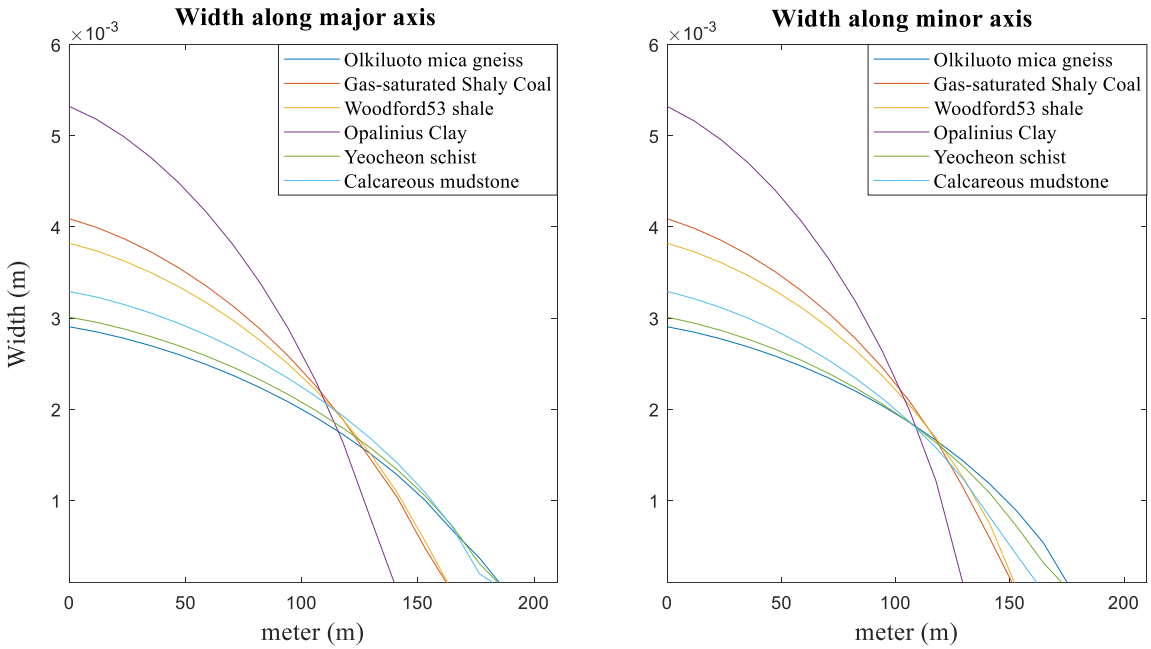


Figure 5.4: Fracture width along major axis (horizontal) and minor axis (vertical)

Figure 5.3 displays the planar fracture geometry in different transversely isotropic rock. The color filling is used to indicate the fracture width. As shown in this figure, for the increasing $\beta$, the elongation of the fracture in horizontal direction is more obvious than the vertical direction. The fracture in Calcareous mudstone ($\beta = 1.9$) demonstrates the minimum aspect ratio $b/a$ with a difference of 20% between the vertical extension and horizontal extension. In addition, according to Figure 5.3 and Figure 5.4**,** the fracture in Opalinius Clay exhibits the minimum fracture area but the maximum fracture width. It can be explained by Eq. (5.5) and Eq. (5.9). the asymptotic displacement solution of the fracture front can be found as $w \propto \sqrt{G_c / B}$ . The minimum value of the elastic modulus $B$ in Opalinius Clay can give the maximum value of the displacement. In the case of the same fluid injection, the fracture is supposed to show the minimum extension. Particularly, for

isotropic material, the elastic modulus $B = E/\left(1-\nu^2\right)$. Thus, the greater value of Young's modulus in the medium can give fracture larger propagation velocity and less fracture width. The engineering elastic constants of the rocks in Table 5.2 give the support to this fact in transversely isotropic material as well. The horizontal and vertical Young's moduli in Opalinius Clay show the minimum values among all the rocks.

In this section, we have a better understanding that the ratio of the elastic moduli $\beta$ could have some impacts on the fracture geometry (aspect ratio, fracture width, fracture area) in the case of the isotropic critical fracture energy. But we are still very curious about how the $\beta$ is relevant to the properties of the material. In other words, we are going to analyze the effect of the specific elastic constants on the fracture shape in transversely isotropic material.

### 5.5.2 Anisotropic effect due to the different engineering elastic constants

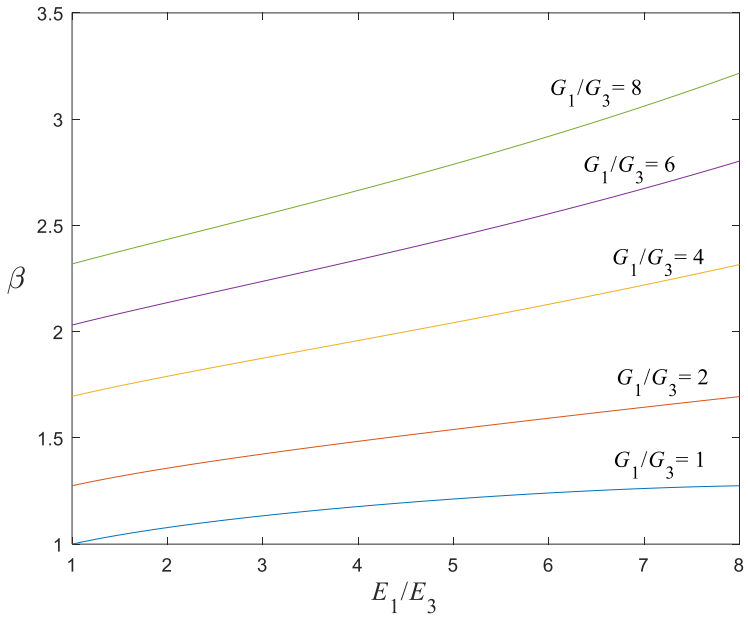


Figure 5.5: Ratio of the elastic moduli $\beta$ versus ratio of the Young's moduli $E_1/E_3$ in the cases of different ratio of shear moduli $G_1/G_3$. ($E_1 = 80\text{GPa}$; $\nu_1 = \nu_3 = 0.2$)

Figure 5.5 demonstrates the ratio between horizontal and vertical elastic moduli in different ratios of the Young's moduli and shear moduli in transversely isotropic material. It is shown clearly that as the ratio between the horizontal and vertical Young's moduli and shear moduli increase, the rock can display stronger elastic anisotropy ($\beta$ increases). In the case of $E_1/E_3 = 1$, the vertical axis shows that $\beta$ varies from 1 to 2.3 as the $G_1/G_3$ varies from 1 to 8. while in the case of $G_1/G_3 = 1$, the $\beta$ only changes from 1 to 1.3 as the $E_1/E_3$ from 1 to 8. This fact tells us the elastic modulus $\beta$ is more sensitive to the shear

moduli than the Young's moduli. And the effect of these elastic parameters can be observed from fracture geometry in Figure 5.6 as well.

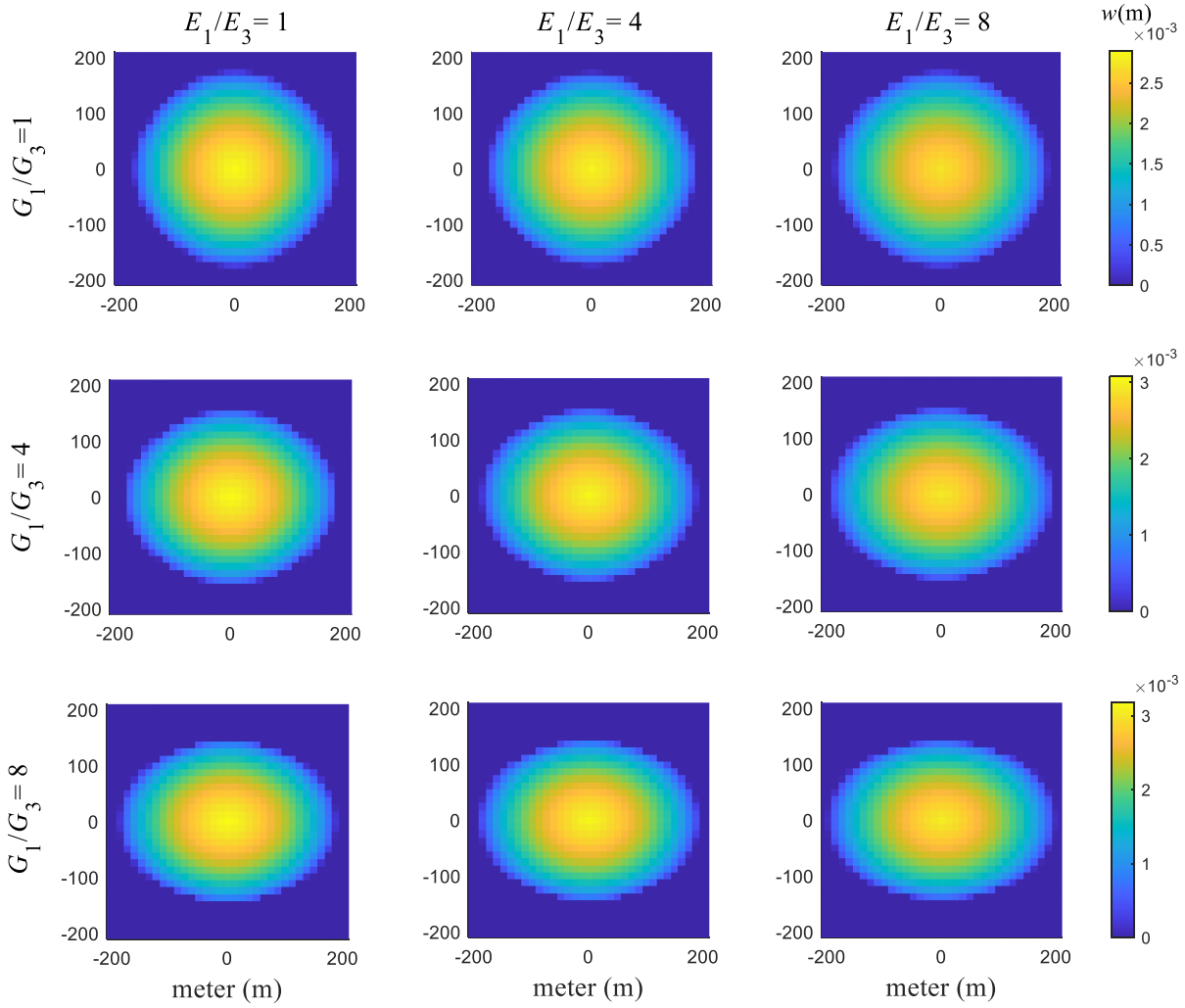


Figure 5.6: Fracture geometries in cases of different ratios of Young's moduli and shear moduli ($\nu_1 = \nu_3 = 0.2$)

Figure 5.6 gives us a visible result on the fracture geometry in different combinations of the ratios of Young's moduli and shear moduli. The first plot ($E_1/E_3 = 1$ and $G_1/G_3 = 1$) is the isotropic case where the fracture shows a circular shape (aspect ratio $b/a$ = 1). As the

ratio of the Young's moduli or shear moduli increases, the fracture starts to deviate from the circle more and more obviously. The aspect ratio *b*/*a* of the fracture is 0.6 in the case of $E_1/E_3 = 8$ and $G_1/G_3 = 8$. The fracture shapes in Figure 5.6 correspond to the values of $\beta$ in Figure 5.5. It agrees with our expectation that the greater value $\beta$ has, the stronger anisotropic effect rock displays. In addition, when comparing three plots in a row and column, we can conclude that the ratio of the shear moduli can have a more evident effect on the evolution of the fracture geometry than the Young's moduli.

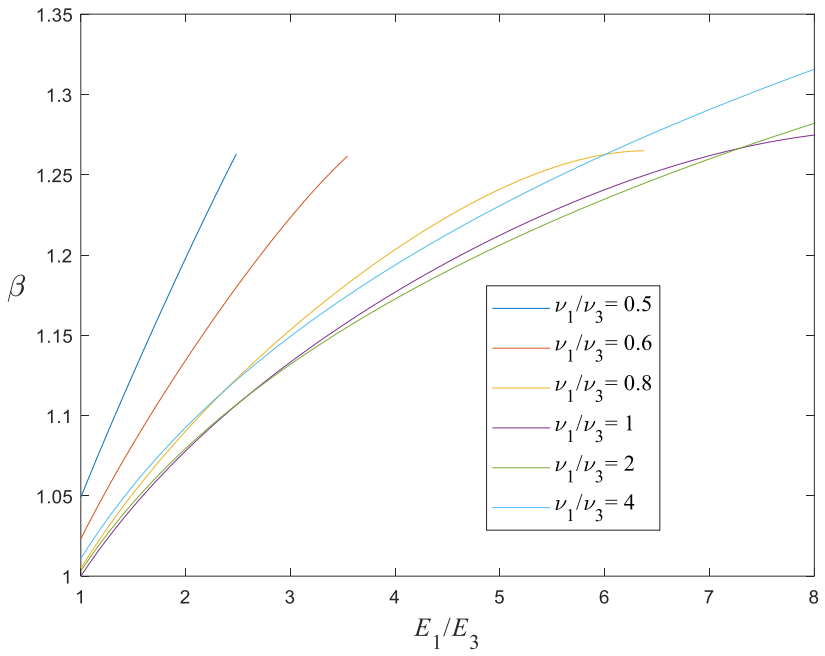


Figure 5.7: Ratio of the elastic moduli $\beta$ versus ratio of the Poisson's ratio $\nu_1/\nu_3$ in the cases of different ratio of Young's moduli $E_1/E_3$. ($E_1 = 80\text{GPa}$; $\nu_1 = 0.2$)

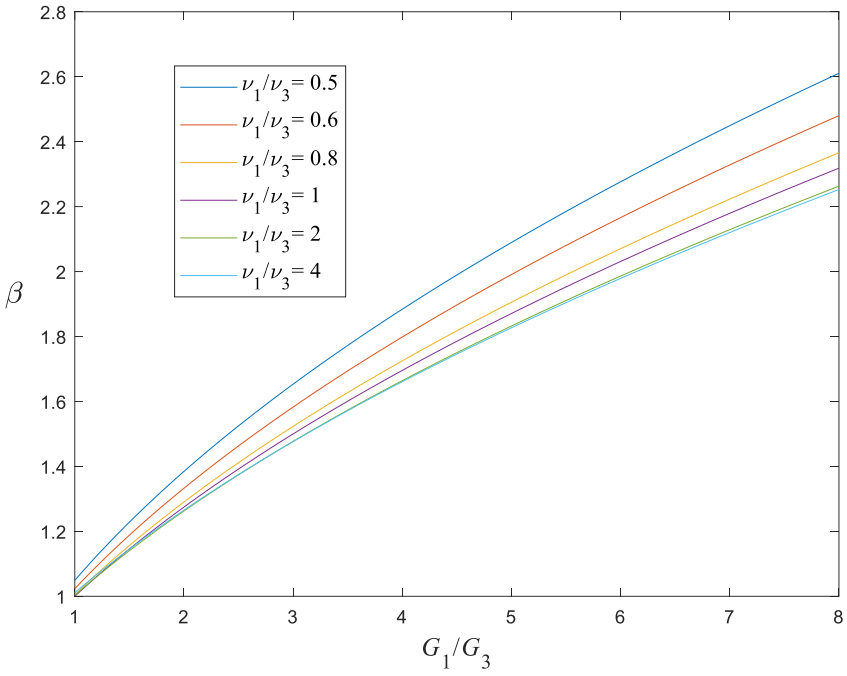


Figure 5.8: Ratio of the elastic moduli $\beta$ versus ratio of the Poisson's ratio $\nu_1/\nu_3$ in the cases of different ratio of shear moduli $G_1/G_3$ ( $E_1 = 80\text{GPa}$ ; $\nu_1 = 0.2$ )

Figure 5.7 and Figure 5.8 display the influence of the Poisson's ratio on the elastic parameter $\beta$ in different ratios of the Young's moduli and shear moduli. In Figure 5.7, the curves of $\nu_1/\nu_3 = 0.5, 0.6, 0.8$ cannot be plotted in all range of the $E_1/E_3 = 1$ to $8$ because of the restriction conditions on the engineering parameters mentioned in **section 2.2.2**. The value of the $\beta$ is less than 1.35 in full range of $E_1/E_3$ . This small $\beta$ cannot have observable influence on the fracture shape and thus the effect of the Poisson ratio can be neglected in the cases of different ratio of Young's moduli. Similar results can be found in Figure 5.8. The maximum difference of the $\beta$ between the curves of the Poisson' ratio occurs at $G_1/G_3 = 8$. In this case, $\beta$ varies from 2.2 to 2.6 and the corresponding fracture

geometry is plotted in Figure 5.9. According to the simulation results, the Poisson ratio does not appear to influence the fracture shape significantly. Young's moduli and shear moduli have more obvious effect on the anisotropic parameter $\beta$ and the fracture geometry.

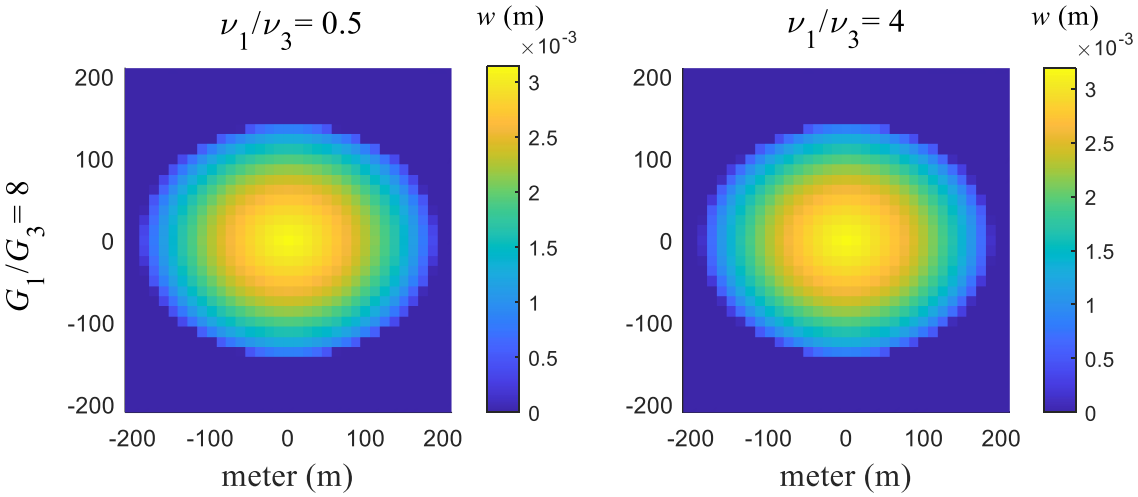


Figure 5.9: Fracture geometry in different ratio of the Poisson ratio in the case of $G_1/G_3 = 8$

### 5.5.2 Anisotropic effect of the energy release rate

In our simulation, we consider the isotropic fracture energy $G_c(\alpha) = G_c$, which gives $K_{Ic}(\alpha) = \sqrt{2G_c B(\alpha)}$ according to Eq. (5.5). Because fracture toughness is used as the fracture propagation criterion, the critical energy release rate $G_c$ may also be an influence factor on the fracture geometry in transversely isotropic material. In this section, we will compare the fracture shapes in the same transversely isotropic material with different

critical energy release rates. The corresponding fracture toughness in horizontal direction $K_{Ic}^{1}$ and vertical direction $K_{Ic}^{3}$ are given in Table 5.3.

Table 5.3: Horizontal and vertical fracture toughness ($K_{Ic}^{1}$ and $K_{Ic}^{3}$ are in $\mathrm{MPa}\cdot\sqrt{\mathrm{m}}$) in Calcareous mudstone ($\beta = 1.9$) in the cases of different critical energy release rate $G_c\,(\mathrm{J/m^2})$

| Calcareous mudstone | $K_{Ic}^{1}$ | $K_{Ic}^{3}$ |
|---|---|---|
| $G_c = 10$ | 0.8 | 0.6 |
| $G_c = 50$ | 1.7 | 1.3 |
| $G_c = 200$ | 3.5 | 2.5 |
| $G_c = 500$ | 5.5 | 4.0 |
| $G_c = 1000$ | 7.8 | 5.6 |
| $G_c = 1500$ | 9.5 | 6.9 |

The results for the different fracture energy cases are given in Figure 5.10. the toughness ratio here is a square root of the ratio of elastic moduli $K_{Ic}^{1}/K_{Ic}^{3} = \sqrt{B_1/B_3} = \sqrt{\beta}$. From $K_{Ic}(\alpha) = \sqrt{2G_c B(\alpha)}$, we know that as the energy release rate increases, the difference between the horizonal toughness and vertical toughness becomes larger, which can also affect the aspect ratio of the fracture and the fracture width. It is clearly depicted in Figure 5.10. For the small value of the $G_c$ ($G_c = 10\,\mathrm{J/m^2}$), the aspect ratio $b/a$ = 0.87 and fracture width at the injection $w_0$ is 3.3mm. While for the large $G_c$ ($G_c = 1500\,\mathrm{J/m^2}$), the aspect ratio decreases to the $b/a$ = 0.6 and $w_0 = 4.0\mathrm{mm}$. This indicates that for the large fracture energy case, the large variations of the fracture toughness can make fracture a significant

difference in the extension along the major axis and minor axis. Therefore, fracture geometry can be influenced a lot.

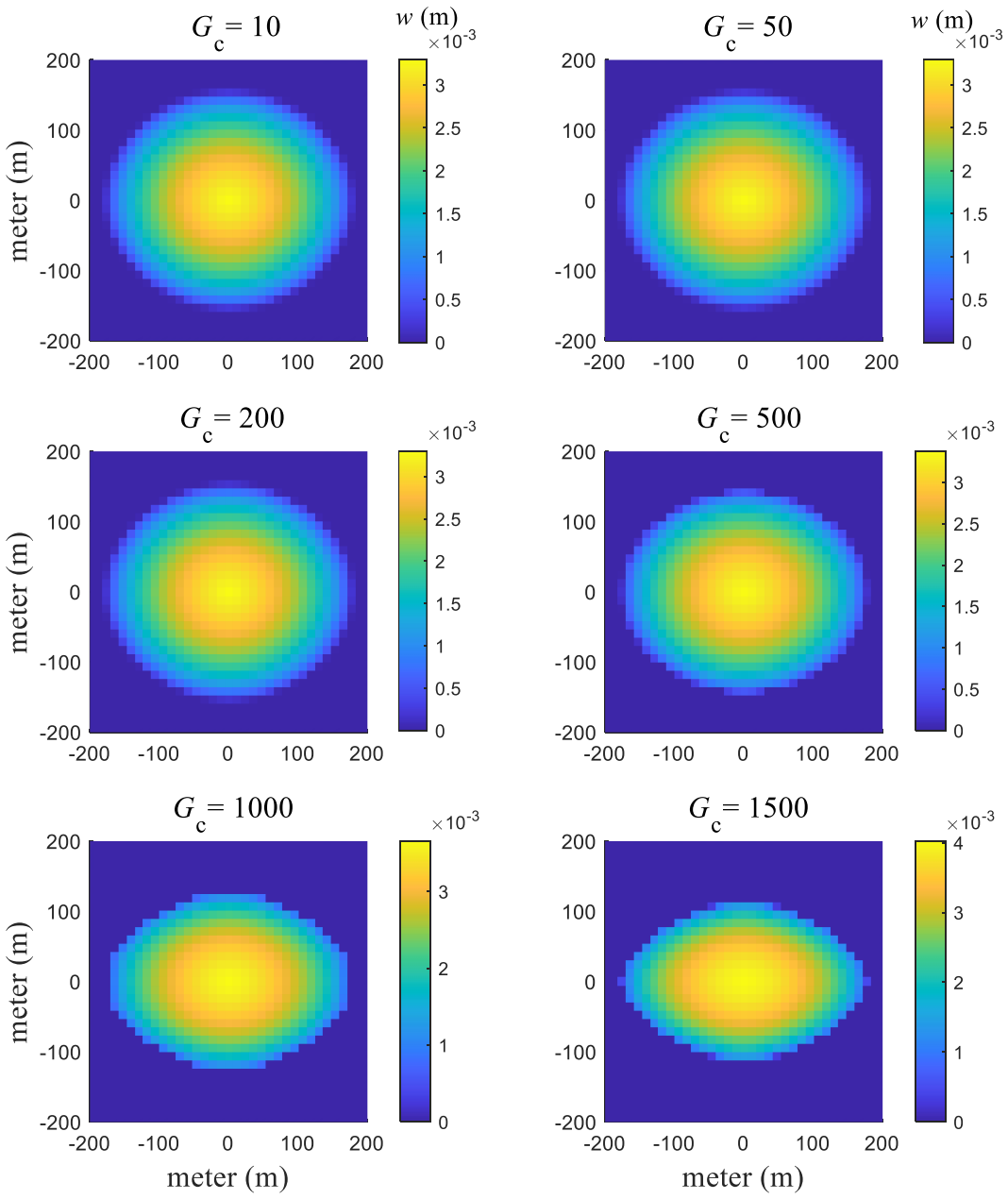


Figure 5.10: Fracture geometry in Calcareous mudstone with different critical energy release rate ($G_c = 10; 50; 200; 500; 1000; 1500\,\mathrm{J/m^2}$)

## 5.6 Average algorithms on Anisotropic material

In most problems involving dislocations of differing orientations and Burgers vectors, the anisotropic elasticity theory of dislocation is much computationally inefficient than the isotropic case because there is no closed-form solution of the Green function in anisotropic media. We have to do some extra calculations of the line integral on Green function or solving fundamental matrices to get the stress field of dislocation segment. The most convenient way is to average the anisotropic elastic constants $C_{ijkl}$ into the isotropic constants ( $E_{avg}$ , $v_{avg}$ ). For this purpose, the most appropriate averaged elastic constants can be found with the use of certain combinations of them which are invariant to rotation of the coordinate system. In this section, two average algorithms (Voigt scheme and Reuss scheme) [69] are introduced to compare with the anisotropic results. The detailed derivations of these two methods are explained in **Appendix D**. In addition to average methods, for simplicity, the horizontal Young's modulus ( $E_1$ ) and Poisson's ratio ( $v_1$ ) are selected as the dominated engineering elastic parameters in fracture extension. These two parameters are used to make the comparisons as well.

### 5.6.1 Average algorithms in different elastic anisotropy

In order to the capture the toughness anisotropic effect $K_{Ic}\left(\alpha\right)$ and solely compare the accuracy of the different average methods on elastic anisotropy of transversely isotropic

material, the fracture toughness anisotropy is still considered in different propagation directions but averaged isotropic parameters ($E_{avg}$, $v_{avg}$) are used in the material. Figure 5.11 shows the test points and corresponding domain used to make the comparisons. 9 points are selected in cases of $\beta = 2; 2.5; 3$. Three points for each value of $\beta$ are used to represent different combinations of the elastic parameters ( $E_1/E_3$ and $G_1/G_3$ ). For covering a large range of domain, the ratios of the Young's moduli are selected to equal to 2,5 and 8, and the corresponding $G_1/G_3$ can be found for the desired $\beta$. The comparison results of fracture geometries obtained by different algorithms in cases of $\beta = 2; 2.5; 3$ are displayed in Figure 5.12 to Figure 5.14, respectively.

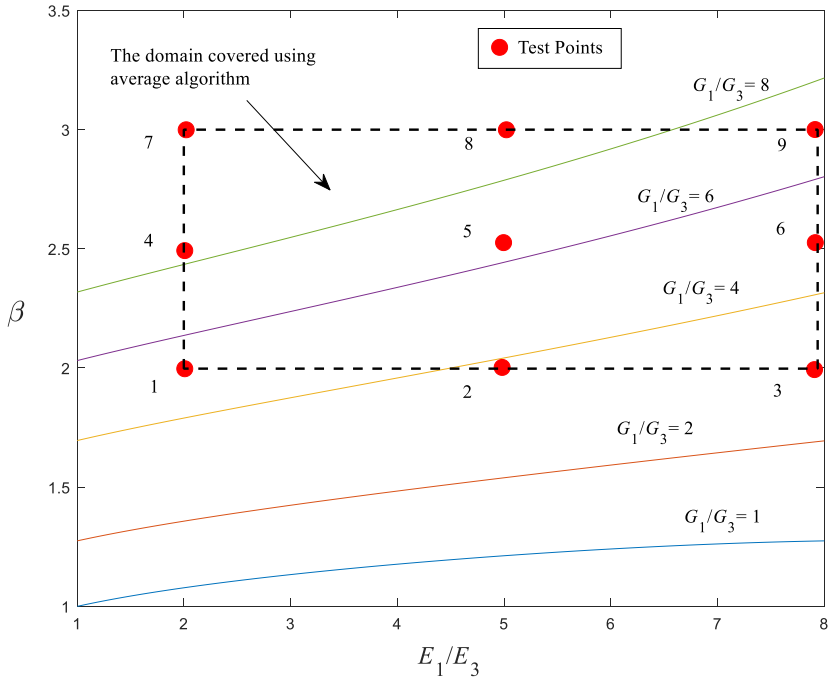


Figure 5.11: Test points used for average methods

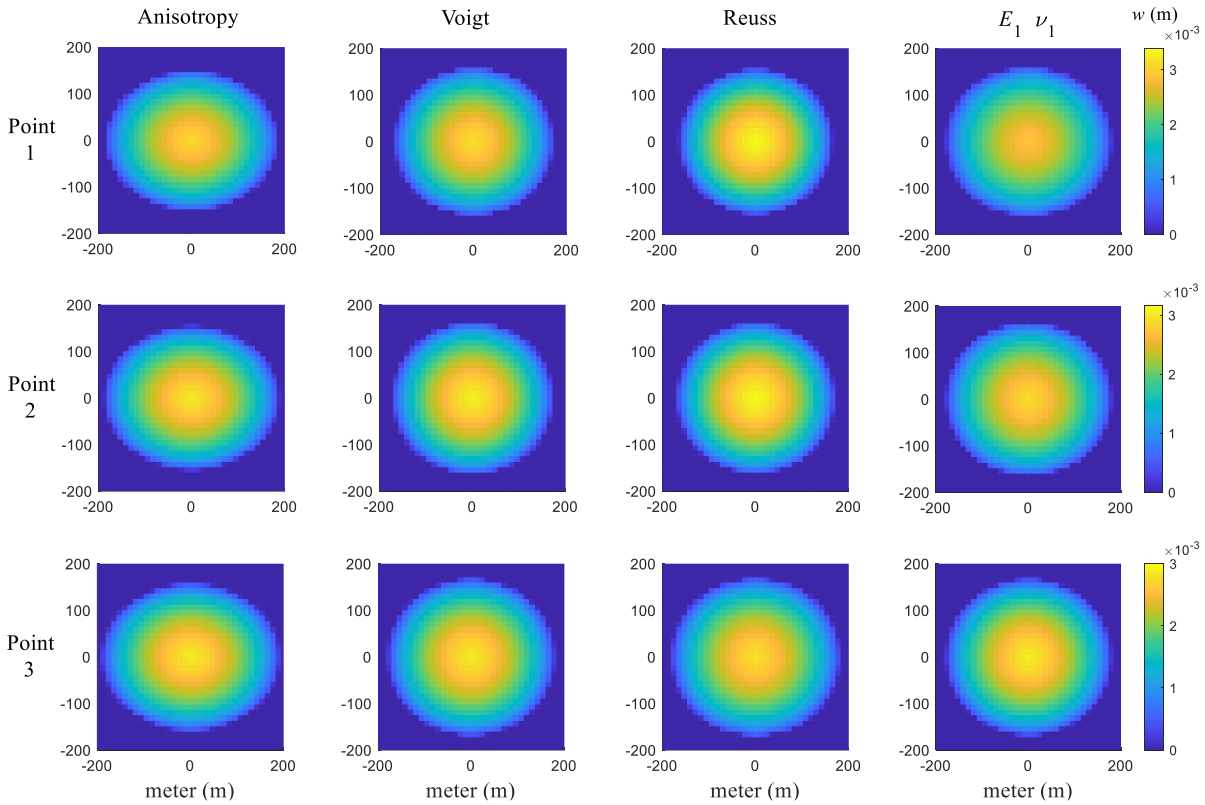


Figure 5.12: Fracture Geometries of anisotropic result and different average schemes in the case of $\beta = 2$ ($G_c = 500\,\mathrm{J/m^2}$)

Each row in Figure 5.12 to Figure 5.14 stands for the fracture shape comparison of one point shown in Figure 5.11 using different methods. For the weak anisotropy shown in Figure 5.12 ($\beta = 2$ or less), maximum errors of three different average algorithms occur at point 1 where $E_1/E_3 = 2$ and $G_1/G_3 = 5.2$. The anisotropic result shows the fracture aspect ratio *b/a* = 0.75 and width at injection $w_0 = 3.10$mm. the best approximation on aspect ratio is given by horizontal parameters ($E_1$ and $\nu_1$) with 15.5% error while 19.5% and 24.8% are given by Voigt and Reuss, respectively. However, the Voigt method has the

minimum error in fracture width at injection which is only 2%. The differences in horizontal parameters and the Reuss method are 5.2% and 9.4%. In the material with weak anisotropy, Voigt method and horizontal parameters can provide more accurate results than Reuss method. Errors in these two algorithms are in tolerance and both are acceptable average algorithms.

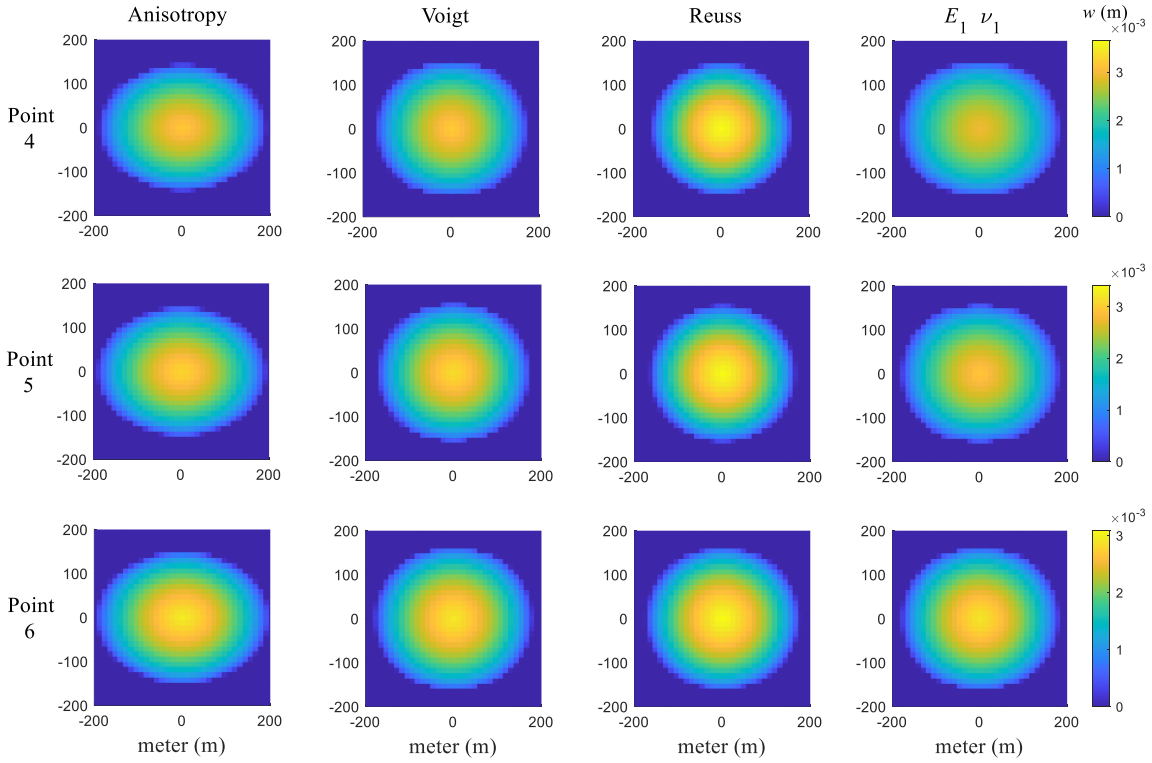


Figure 5.13: Fracture Geometries of anisotropic result and different average schemes in the case of $\beta = 2.5$ ($G_c = 500\,\mathrm{J/m^2}$)

In the case of the medium anisotropy ($\beta = 2.5$), the maximum errors of the fracture aspect ratio in Voigt method and horizontal parameters are 15.6% and 16.4% given at point 6 in

Figure 5.13. For the Reuss method, error reaches the largest value at point 5 which is 26.8%. In addition, Voigt method is still the best algorithm for fracture width with less than

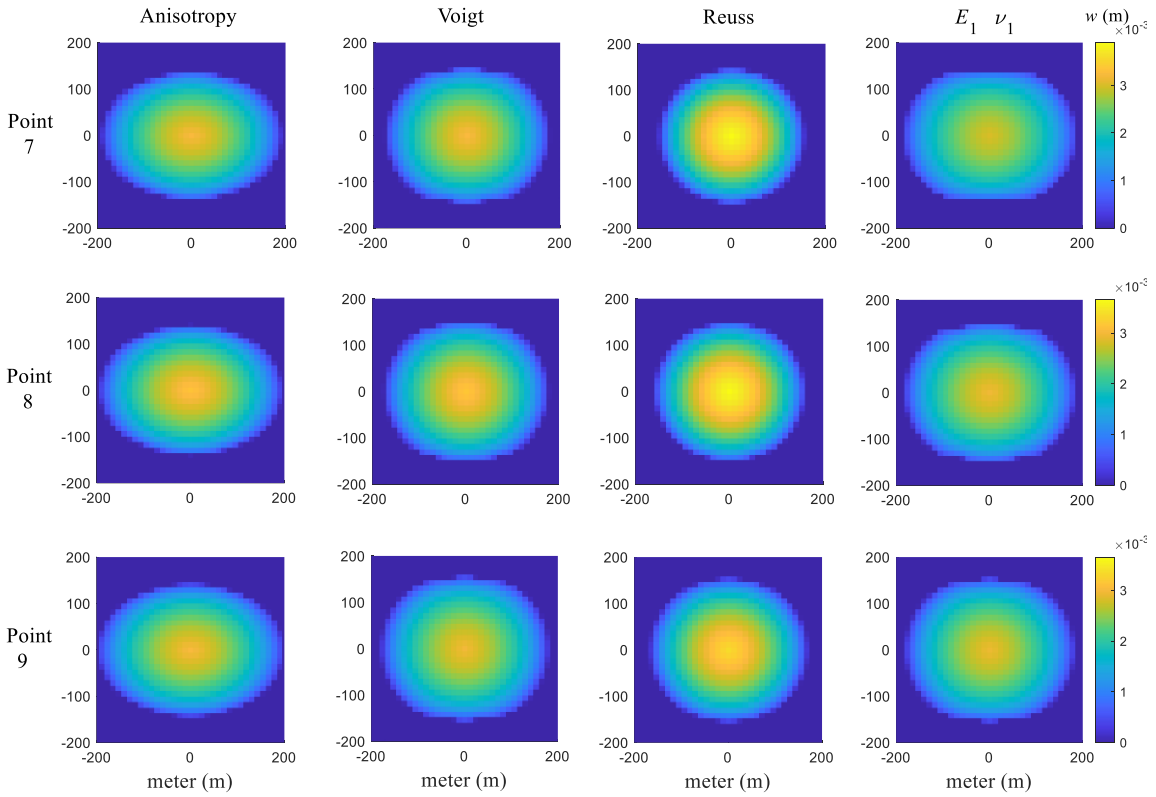


Figure 5.13: Fracture Geometries of anisotropic result and different average schemes in the case of $\beta = 3$ ($G_c = 500\,\mathrm{J/m^2}$)

3% error in all three points. Horizontal parameters are relatively accurate with 7.3% error at most compared with the 15.2% in Reuss scheme. For the large elastic anisotropy ( $\beta = 3$ or greater), the inaccuracy in Reuss method is more obvious which shows a difference of 34.3% in *b*/*a* and 20.9% in $w_0$ (Figure 5.14). However, the Voigt method and horizontal parameters can still provide a good estimation on the fracture geometry. The maximum

error in $b/a$ is 16.3% and in $w_0$ is 4.2% in Voigt scheme, and 10.4%, 6.9% for aspect ratio and width in horizontal parameters, respectively.

In summary, the Voigt method and horizontal parameters can give good approximation on the anisotropic material in a wide range of elastic anisotropy, although the Voigt is slightly better. In the case of weak anisotropy ($\beta < 2$), the result of Reuss method is acceptable. But the error is more and more significant for increasing $\beta$. For a strong anisotropic material, the Reuss method cannot provide an accurate estimation on the fracture shape and is not applicable in this case. On the contrary, the horizontal parameters work better as the anisotropic effect is more evident. In this case, the ratios of the Young's moduli and shear moduli both have a large value and thus horizontal parameters can dominate vertical parameters in transversely isotropic material.

### 5.6.2 Average method in different fracture energy

In above simulations, the critical energy release rate is select as $G_c = 500\,\mathrm{J/m^2}$ and we compare the accuracies of the different average algorithms in cases of different elastic anisotropy. But we still need to figure out whether there is any influence on the average algorithms by the fracture energy. Thus, we compare the results of anisotropic method and the Voigt average method in a medium anisotropic material ($\beta = 2.5$) with different critical energy release in Figure 5.15.

As shown in Figure 5.15, in the material with low fracture energy ($G_c = 50\,\mathrm{J/m^2}$), the aspect ratio *b*/*a* of the fracture solved by anisotropic result is 0.8 and fracture width at injection $w_0$ is 3.04mm. The Voigt solution gives an obvious different fracture aspect ratio which nearly equals to 1 (25% difference) but very accurate fracture width 3.05mm. In the case of $G_c = 500\,\mathrm{J/m^2}$, the error in *b*/*a* is 15.4% and in $w_0$ is 2%. For the material with a large critical energy release rate ($G_c = 1500\,\mathrm{J/m^2}$), the error of the fracture aspect ratio keeps decreasing, which is only 7.1% and fracture width is 1.5%. From these results, we can conclude that as the fracture energy increases, the average algorithm can give a better approximation on the fracture geometry. This fact can be deduced from the factors related to the fracture extension. In the case of small fracture energy $G_c$, the fracture shape is dominated by the elastic anisotropy (value of $\beta$). Thus, the average method is supposed to have large error in a strong anisotropic material. However, as the critical fracture energy increases, the fracture energy will have more evident effect on the propagation of the fracture. By contrast, the effect of the elastic anisotropy becomes less significant and the average algorithm can give a relatively accurate result.

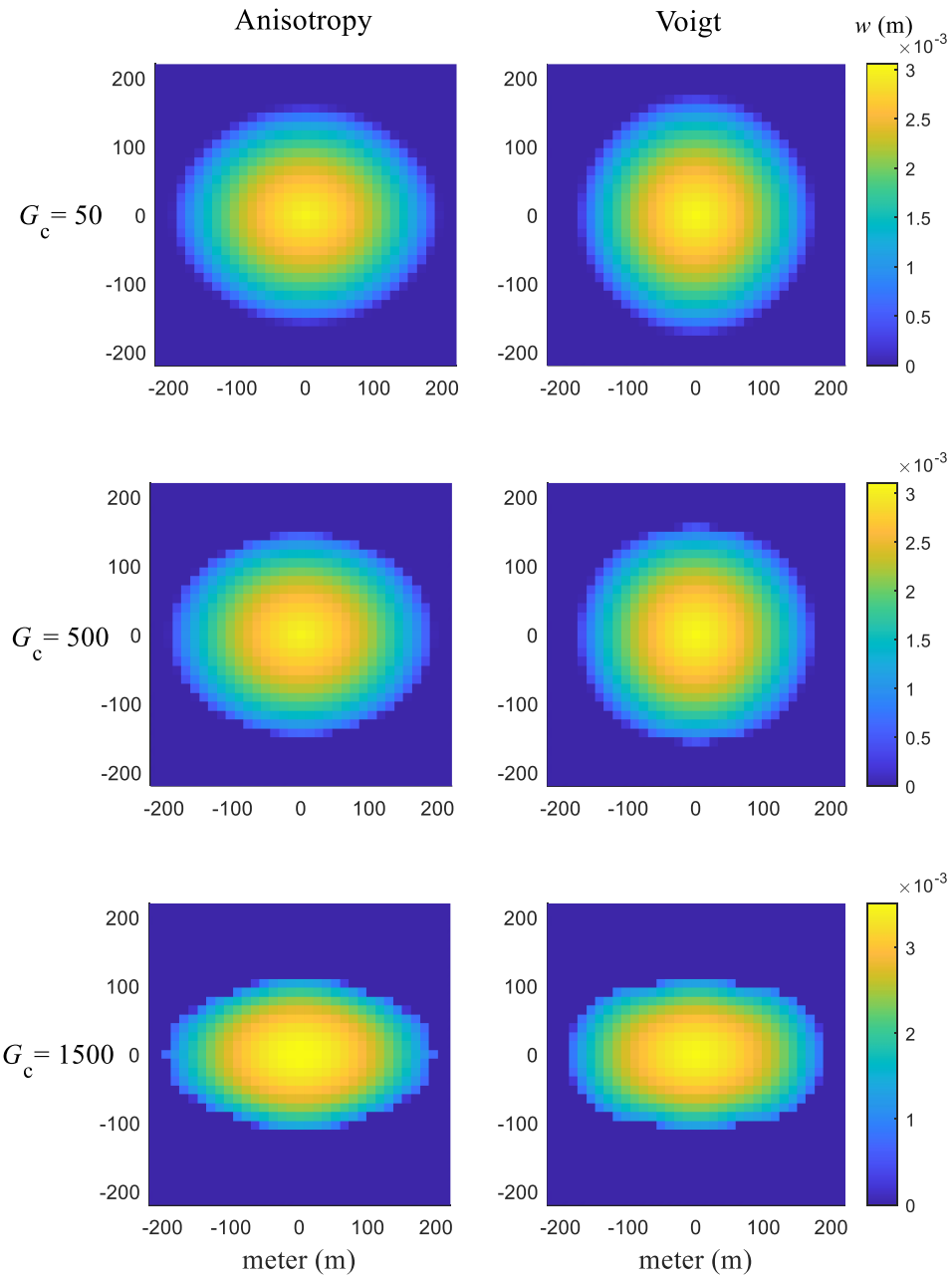


Figure 5.14: Comparison results of anisotropic method and Voigt average method in anisotropic material ( $\beta = 2.5$ ) with different fracture energy ( $G_c = 50; 500; 1500\,\mathrm{J/m^2}$ )

## 5.7 Conclusion

Propagation of a planar hydraulic fracture (HF) perpendicular to the isotropy plane is the most common configuration encountered during the stimulation of the unconventional reservoirs. Utilizing a planar 3D fracture model, we have investigated the impact of transverse isotropy on the growth of a hydraulic fracture. In addition, the average algorithm is analyzed to improve the efficiency of our numerical model.

Using the displacement discontinuity method combined with the anisotropic dislocation theory, the stress field of the planar fracture in transversely isotropic material can be solved numerically. An elastic modulus *B* is introduced in Irving matrix relating the energy release rate and stress intensity factor in our configuration. This parameter *B* is also a near-tip elastic operator as the function of the angle between the local fracture propagation direction and the isotropy plane. In addition, an exact solution to *B* is given in horizontal and vertical direction in transversely isotropic material. Fracture toughness is also a direction-dependent parameter which can be obtained from the near-tip asymptotic solution and used as the fracture propagation condition.

In the result part, we first analyze the anisotropic effect on the planar 3D fractures in some transversely isotropic rocks. The ratio of the elastic moduli between horizontal direction and vertical direction $\beta$ is used to quantify the elastic anisotropy in TI material. The material displays a stronger elastic anisotropy for increasing $\beta$ and thus the fracture shows an elongation in horizontal direction and shortening in vertical direction. Then $\beta$ is investigated for the relationship between the 5 engineering parameters ( $E_1, E_3, \nu_1, \nu_3, G_3$ ).

The ratios of the Young's moduli and shear moduli ( $E_1/E_3$ , $G_1/G_3$ ) have dominated effect on the $\beta$, even though the ratio of shear moduli is more significantly. The alternation of the fracture geometry is displayed in different sets of the engineering parameters. In the case of $E_1/E_3 = 8$ and $G_1/G_3 = 8$, $\beta$ reaches the maximum value 3.3 and aspect ratio *b*/*a* of the fracture reaches minimum value 0.6, which shows a strong anisotropic effect on the fracture geometry. Since the fracture toughness is implemented as the condition of the fracture propagation, the fracture energy $G_c$ is considered as another influence factor in anisotropic effect. As $G_c$ increase, the ratio of the toughness between horizontal and vertical direction does not change ( $K_{Ic}^1/K_{Ic}^3 = \sqrt{\beta}$ ) but variation between them is larger. It can cause a significant difference in fracture propagating speed along horizontal axis and vertical axis. The aspect ratio of the fracture decreases to the 0.6 for $G_c = 1500\,\mathrm{J/m^2}$.

In the last section, For the purpose of reducing the computational burden of the simulation, the average method is used to approximate the anisotropic material into isotropic one while the toughness anisotropy is still considered. In this averaging algorithm, we only need to compute the elastic modulus *B* in different propagation directions and use the isotropic formula to calculate the stress field of the fracture surface. Thus, the tedious computation of anisotropic equations can be eliminated. For a large range of the $\beta$ ($\beta = 1 \sim 3$), the Voigt scheme and horizontal engineering parameters can provide more accurate results than the Reuss scheme. Difference is more obvious in large values of $\beta$. However, horizontal engineering parameters can give better estimation in the strong anisotropic rocks where the horizontal elastic moduli dominate other parameters. The impact of the fracture

energy on average algorithm is tested in the end. For the material with small $G_c$ where elastic anisotropy has more significant effect on evolution of the fracture, the average algorithm is less accurate. As the $G_c$ increases, the fracture geometry is largely influenced by the fracture energy and elastic anisotropy effect is not obvious. The average algorithm works quite well in this case.

# Bibliography

[1] Smith, Michael Berry, and Carl Montgomery. Hydraulic fracturing. CRC press, 2015.

[2] Liang, Feng, et al. "A comprehensive review on proppant technologies." Adv. Res. Evolving Sci (2015).

[3] Montgomery, Carl T., and Michael B. Smith. "Hydraulic fracturing: History of an enduring technology." Journal of Petroleum Technology 62.12 (2010): 26-40.

[4] Li, Q., Xing, H., Liu, J., & Liu, X. (2015). A review on hydraulic fracturing of unconventional reservoir. Petroleum, 1(1), 8-15.

[5] Milliken, Kitty L., and Nicholas W. Hayman. "Mudrock components and the genesis of bulk rock properties: review of current advances and challenges." Shale: Subsurface Science and Engineering (2019): 1-25.

[6] Belyadi, Hoss, Ebrahim Fathi, and Fatemeh Belyadi. Hydraulic fracturing in unconventional reservoirs: theories, operations, and economic analysis. Gulf Professional Publishing, 2019.

[7] Daneshy, Ali. "Hydraulic fracturing of horizontal wells: Issues and insights." SPE Hydraulic Fracturing Technology Conference. OnePetro, 2011.

[8] Verisokin, A. E., V. A. Vasil'Yev, and T. A. Gun'Kina. "Packer design research used in hydraulic fracturing." IOP Conference Series: Earth and Environmental Science. Vol. 378. No. 1. IOP Publishing, 2019.

[9] Weller, J. Marvin. "Compaction of sediments." AAPG Bulletin 43.2 (1959): 273-310.

[10] Britt, Larry K., and Jerry Schoeffler. "The geomechanics of a shale play: What makes a shale prospective!." *SPE eastern regional meeting*. OnePetro, 2009.

[11] Serajian, V., and A. Ghassemi. "Hydraulic Fracture Initiation From a Wellbore In Transversely Isotropic Rock, American Rock Mechanics Association." (2011).

[12] Perkins, T. K, and L. Re Kern. "Widths of hydraulic fractures." *Journal of petroleum technology* 13.09 (1961): 937-949.

[13] Sneddon, I. N., and H. A. Elliot. "The opening of a Griffith crack under internal pressure." *Quarterly of Applied Mathematics* 4.3 (1946): 262-267.

[14] Nordgren, R. P. "Propagation of a vertical hydraulic fracture." *Society of petroleum engineers journal* 12.04 (1972): 306-314.

[15] Zheltov, A. Khristianovic. "3. Formation of vertical fractures by means of highly viscous liquid." *World petroleum congress*. WPC, 1955.

[16] Geertsma, J., and F. De Klerk. "A rapid method of predicting width and extent of hydraulically induced fractures." *Journal of petroleum technology* 21.12 (1969): 1571-1581.

[17] Sneddon, Ian Naismith. "The distribution of stress in the neighbourhood of a crack in an elastic solid." *Proceedings of the Royal Society of London. Series A. Mathematical and Physical Sciences* 187.1009 (1946): 229-260.

[18] Mack, Mark G., et al. "Mechanics of hydraulic fracturing." *Reservoir stimulation* (2000): 6-1.

[19] Clifton, Rodney J., and Ahmed S. Abou-Sayed. "A variational approach to the prediction of the three-dimensional geometry of hydraulic fractures." *SPE Rocky Mountain Petroleum Technology Conference/Low-Permeability Reservoirs Symposium*. SPE, 1981.

[20] Advani, S. H., T. S. Lee, and J. K. Lee. "Three-dimensional modeling of hydraulic fractures in layered media: part I—finite element formulations." (1990): 1-9.

[21] Carter, B. J., et al. "Simulating fully 3D hydraulic fracturing." *Modeling in geomechanics* 200 (2000): 525-557.

[22] Xu, Guanshui, and Sau-Wai Wong. "Interaction of multiple non-planar hydraulic fractures in horizontal wells." *IPTC 2013: International Petroleum Technology Conference*. European Association of Geoscientists & Engineers, 2013.

[23] Boresi, Arthur P., Ken Chong, and James D. Lee. *Elasticity in engineering mechanics*. John Wiley & Sons, 2010.

[24] Moukhtari, Fatima-Ezzahra. *Propagation of fluid driven fractures in transversely isotropic material*. No. 7470. EPFL, 2020.

[25] Exadaktylos, G. E. "On the constraints and relations of elastic constants of transversely isotropic geomaterials." *International Journal of Rock Mechanics and Mining Sciences* 38.7 (2001): 941-956.

[26] Bower, Allan F. *Applied mechanics of solids*. CRC press, 2009.

[27] Anderson, Peter M., John P. Hirth, and Jens Lothe. *Theory of dislocations*. Cambridge University Press, 2017.

[28] Crouch SL, Starfield AM. Boundary element methods in solid mechanics. London: Unwin & Hyman; 1990.

[29] Batchelor, Cx K., and George Keith Batchelor. An introduction to fluid dynamics. Cambridge University Press, 1967.

[30] Barnett, D. M., and R. J. Asaro. "The fracture mechanics of slit-like cracks in anisotropic elastic media." *Journal of the Mechanics and Physics of Solids* 20.6 (1972): 353-366.

[31] Savitski A A, Detournay E. Propagation of a penny-shaped fluid-driven fracture in an impermeable rock: asymptotic solutions[J]. International journal of solids and structures, 2002, 39(26): 6311-6337.

[32] Advani, S. H., T. S. Lee, and J. K. Lee. "Three-dimensional modeling of hydraulic fractures in layered media: part I—finite element formulations." (1990): 1-9.

[33] Barree, Robert D. "A practical numerical simulator for three-dimensional fracture propagation in heterogeneous media." SPE reservoir simulation symposium. OnePetro, 1983.

[34] Ben Naceur, Kamel, Marc Thiercelin, and Eric Touboul. "Simulation off Fluid Flow in Hydraulic Fracturing: Implications for 3D Propagation." SPE Production Engineering 5.02 (1990): 133-141.

[35] Vandamme, L., and J. H. Curran. "A three-dimensional hydraulic fracturing simulator." International Journal for Numerical Methods in Engineering 28.4 (1989): 909-927.

[36] Adachi, J., et al. "Computer simulation of hydraulic fractures." International Journal of Rock Mechanics and Mining Sciences 44.5 (2007): 739-757.

[37] Peirce, Anthony, and Emmanuel Detournay. "An implicit level set method for modeling hydraulically driven fractures." Computer Methods in Applied Mechanics and Engineering 197.33-40 (2008): 2858-2885.

[38] Dontsov, E. V., and A. P. Peirce. "A non-singular integral equation formulation to analyse multiscale behaviour in semi-infinite hydraulic fractures." Journal of Fluid Mechanics 781 (2015): R1.

[39] Dontsov, E. V., and A. P. Peirce. "A multiscale implicit level set algorithm (ILSA) to model hydraulic fracture propagation incorporating combined viscous, toughness, and leak-off asymptotics." Computer Methods in Applied Mechanics and Engineering 313 (2017): 53-84.

[40] Barber, James R. Elasticity. Dordrecht: Kluwer academic publishers, 2002.

[41] Hills, David Anthony, et al. *Solution of crack problems: the distributed dislocation technique*. Vol. 44. Springer Science & Business Media, 2013.

[42] Verecký, Š., J. Kratochvíl, and F. Kroupa. "The stress field of rectangular prismatic dislocation loops." physica status solidi (a) 191.2 (2002): 418-426.

[43] Hubbert, M. King, and David G. Willis. "Mechanics of hydraulic fracturing." *Transactions of the AIME* 210.01 (1957): 153-168.

[44] Detournay, Emmanuel, and Anthony Peirce. "On the moving boundary conditions for a hydraulic fracture." International Journal of Engineering Science 84 (2014): 147-155.

[45] Rice, James R. "Mathematical analysis in the mechanics of fracture." Fracture: an advanced treatise 2 (1968): 191-311.

[46] Xu, G., A. S. Argon, and M. Ortiz. "Critical configurations for dislocation nucleation from crack tips." Philosophical Magazine A 75.2 (1997): 341-367.

[47] Wang, HanYi, ShiTing Yi, and Mukul M. Sharma. "A computationally efficient approach to modeling contact problems and fracture closure using superposition method." Theoretical and Applied Fracture Mechanics 93 (2018): 276-287.

[48] Eshelby, J. D., W. T. Read, and W. Shockley. "Anisotropic elasticity with applications to dislocation theory." Acta metallurgica 1.3 (1953): 251-259.

[49] Stroh, AN139306. "Steady state problems in anisotropic elasticity." Journal of Mathematics and Physics 41.1-4 (1962): 77-103.

[50] Barnett, D. M., and L. A. Swasger. "The elastic energy of a straight dislocation in an infinite anisotropic elastic medium." Physica status solidi (b) 48.1 (1971): 419-428.

[51] Indenbom, Vladimir L., and Jens Lothe, eds. Elastic strain fields and dislocation mobility. Elsevier, 2012.

[52] Willis, J. R. "Stress fields produced by dislocations in anisotropic media." Philosophical Magazine 21.173 (1970): 931-949.

[53] Stroh A N. Dislocations and cracks in anisotropic elasticity[J]. Philosophical magazine, 1958, 3(30): 625-646.

[54] Nishioka, K., and J. Lothe. "Isotropic Limiting Behaviour of the Six-Dimensional Formalism of Anisotropic Dislocation Theory and Anisotropic Green's Function Theory. I. Sum Rules and Their Applications." physica status solidi (b) 51.2 (1972): 645-656.

[55] Bacon, D. J., D. M. Barnett, and Ronald Otto Scattergood. "Anisotropic continuum theory of lattice defects." Progress in Materials Science 23 (1980): 51-262.

[56] Barnett D M, Lothe J. Dislocations and line charges in anisotropic piezoelectric insulators[J]. physica status solidi (b), 1975, 67(1): 105-111.

[57] Yin, Jie, David M. Barnett, and Wei Cai. "Efficient computation of forces on dislocation segments in anisotropic elasticity." Modelling and Simulation in Materials Science and Engineering 18.4 (2010): 045013.

[58] Sih, George C., and E. P. Chen. Cracks in composite materials: a compilation of stress solutions for composite systems with cracks. Vol. 6. Springer Science & Business Media, 2012.

[59] Economides, Michael J., and Kenneth G. Nolte. Reservoir stimulation. Vol. 2. Englewood Cliffs, NJ: Prentice Hall, 1989.

[60] Hubbert M K, Willis D G. Mechanics of hydraulic fracturing[J]. Transactions of the AIME, 1957, 210(01): 153-168.

[61] Bunger A, Lecampion B. Four critical issues for successful hydraulic fracturing applications[J]. Rock mechanics and engineering, 2017 (BOOK_CHAP).

[62] Wang X L, Shi F, Liu H, et al. Numerical simulation of hydraulic fracturing in orthotropic formation based on the extended finite element method[J]. Journal of Natural Gas Science and Engineering, 2016, 33: 56-69.

[63] Zeng Q D, Yao J, Shao J. Numerical study of hydraulic fracture propagation accounting for rock anisotropy[J]. Journal of Petroleum Science and Engineering, 2018, 160: 422-432.

[64] Bessmertnykh A O, Dontsov E V. Aspect ratio of hydraulic fracture in homogeneous transversely isotropic material[C]//52nd US Rock Mechanics/Geomechanics Symposium. OnePetro, 2018.

[65] Hoenig A. The behavior of a flat elliptical crack in an anisotropic elastic body[J]. International Journal of Solids and Structures, 1978, 14(11): 925-934.

[66] Zia H, Lecampion B, Zhang W. Impact of the anisotropy of fracture toughness on the propagation of planar 3D hydraulic fracture[J]. International Journal of Fracture, 2018, 211: 103-123.

[67] Moukhtari F E, Lecampion B, Zia H. Planar hydraulic fracture growth perpendicular to the isotropy plane in a transversely isotropic material[J]. Journal of the Mechanics and Physics of Solids, 2020, 137: 103878.

[68] Laubie H, Ulm F J. Irwin′ s conjecture: Crack shape adaptability in transversely isotropic solids[J]. Journal of the Mechanics and Physics of Solids, 2014, 68: 1-13.

[69] Hirth, J. P., Lothe, J., & Mura, T. (1983). Theory of dislocations. Journal of Applied Mechanics, 50(2), 476.

# Appendix A

## Asymptotic solution for a penny-shaped fracture in an impermeable isotropic medium

Scaling analysis is applied to the governing equations of this problem by using following dimensionless quantities:

$$\begin{aligned} w(r,t) &= \varepsilon(t) L(t) \Omega\left(\rho, \lambda(t)\right) \\ p(r,t) &= \varepsilon(t) E' \Pi\left(\rho, \lambda(t)\right) \\ R(t) &= L(t) \gamma\left(\lambda(t)\right) \end{aligned} \tag{A.1}$$

Where $\rho = r/R$, $\Omega$, $\Pi$ and $\gamma$ are dimensionless crack opening, net pressure and fracture radius, respectively. $\varepsilon(t)$ is a small scaling number and $L(t)$ is a length scale of the same order of $R(t)$. $\lambda(t)$ is a dimensionless parameter depending monotonically on *t*.

Scaling analysis indicates that for two limiting cases: the viscosity-dominated regime ( $\kappa = 0$) and toughness-dominated regime ( $\kappa = \infty$), the solution is self-similar and thus does not depend on the initial conditions. The dimensionless parameter $\kappa$ used to distinguish two propagating regimes is defined as

$$\kappa = K'_{Ic}\left(\frac{t^2}{\mu'^5 Q_0^3 E'^{13}}\right)^{1/18} \tag{A.2}$$

where $K'_{Ic} = 4\sqrt{\frac{2}{\pi}}K_{Ic}$, $\mu' = 12\mu$, $E' = \frac{E}{\left(1-\nu^2\right)}$, $Q_0$ is the injection rate and $t$ is the injection duration.

**Viscosity-dominated regime**

As $\kappa < 1$, the zero-toughness solution can be used as the asymptotic solution for the viscosity-dominated regime, which is given as

$$\bar{\Omega}_{m0}^{(1)} = \left(\frac{\sqrt{70}}{3}C_1^{(1)} + \frac{4\sqrt{5}}{9}C_2^{(1)}\left(13\rho - 6\right)\right)\left(1-\rho\right)^{2/3} + B^{(1)}\left[\frac{8}{\pi}\left(1-\rho\right)^{1/2} - \frac{8}{\pi}\rho\arccos\rho\right] \tag{A.3}$$

$$\Pi_{m0}^{(1)} = A_1^{(1)}\left[\omega_1 - \frac{2}{3\left(1-\rho\right)^{1/3}}\right] - B^{(1)}\left(\ln\frac{\rho}{2} + 1\right) \tag{A.4}$$

where $A_1^{(1)} = 0.3581$, $B^{(1)} = 0.09269$, $C_1^{(1)} = 0.6846$, $C_2^{(1)} = 0.07098$, $\omega_1 = 2.479$, $\gamma_m^{(1)}\left(0\right) = 0.6955$ and $\bar{\Omega}_{m0}^{(1)} = \Omega_m^{(1)}\left(\rho,0\right)/\gamma_m^{(1)}\left(0\right)$, $\Pi_{m0}^{(1)} = \Pi_m^{(1)}\left(\rho,0\right)$. The superscript (1) means the first order solution and subscript *m* represents the viscosity scaling. Also, two viscosity scaling parameters are defined as

$$\varepsilon_m = \left(\frac{\mu'}{E't}\right)^{1/3},\ L_m = \left(\frac{E'Q_0^3t^4}{\mu'}\right)^{1/9} \tag{A.5}$$

**Toughness-dominated regime**

As $\kappa > 3.5$, the large-toughness solution is used for toughness-dominated regime and two toughness scaling parameters are

$$\varepsilon_k = \left( \frac{K_{Ic}'^{\,6}}{E'^{6} Q_0 t} \right)^{1/5}, \; L_k = \left( \frac{Q_0^2 E'^{2} t^2}{K_{Ic}'^{\,2}} \right)^{1/5} \tag{A.6}$$

The first order large-toughness solution is given by

$$\Omega_{k1} = B_k \left(1-\rho^2\right)^{1/2} - \frac{8}{3\pi} A_k \gamma_{k0} \left[ \left( \ln 2 - \frac{4}{5} \right) \left(1-\rho^2\right)^{1/2} + \rho \arccos \rho - \frac{6}{5} I^*(\rho) \right] \tag{A.7}$$

$$\Pi_{k1} = \Pi_{k1}^* - A_k \left[ \frac{1}{3} \ln \rho - \frac{1}{5} \ln\left(1-\rho^2\right) \right] \tag{A.8}$$

where subscript *k* represents toughness scaling. $\Pi_{k1}^* = 0.6380$, $A_k = 1.709$, $B_k = 0.8264$, $\gamma_{k0} = 0.8546$ and function $I^*(\rho) = \int_\rho^1 \sqrt{\frac{1-\xi^2}{\xi^2-\rho^2}} \arcsin\xi \, d\xi$ has to be evaluated numerically.

# Appendix B

## Angular derivatives of *Q*, *B* and *S*

In the matrix formalism, the angular derivatives of $\boldsymbol{Q}$, $\boldsymbol{B}$ and $\boldsymbol{S}$ can be obtained by studying the angular derivative of matrix $\boldsymbol{N}$. Referring to the Figure B.1, we know

$$\frac{\partial \boldsymbol{t}}{\partial \theta} = \boldsymbol{m} \qquad \frac{\partial^2 \boldsymbol{t}}{\partial \theta^2} = -\boldsymbol{t} \tag{B.1}$$

and

$$\frac{\partial \boldsymbol{N}}{\partial \theta} = \begin{bmatrix} (nn)^{-1}(nt) & 0 \\ \boldsymbol{q} & (tn)(nn)^{-1} \end{bmatrix} \tag{B.2}$$

where

$$\boldsymbol{q} = (tn)(nn)^{-1}(nm) + (mn)(nn)^{-1}(nt) - (tm) - (mt) \tag{B.3}$$

The derivatives of the Stroh eigenvectors can then be obtained

$$\frac{\partial \xi_\beta}{\partial \theta} = \sum_{\substack{\alpha=1 \\ \alpha \neq \beta}}^{6} \frac{N^1_{\alpha\beta}}{p_\beta - p_\alpha} \xi_\alpha \tag{B.4}$$

where

$$N^1_{\alpha\beta} = \left(\xi_\alpha\right)^T \boldsymbol{T} \frac{\partial N}{\partial \theta} \xi_\beta \tag{B.5}$$

$$\boldsymbol{T} = \begin{bmatrix} 0 & \boldsymbol{I} \\ \boldsymbol{I} & 0 \end{bmatrix} \tag{B.6}$$

where $\boldsymbol{I}$ is 3x3 identity matrix

Recall that $\boldsymbol{\xi_\alpha} = \begin{pmatrix} \boldsymbol{A}_\alpha \\ \boldsymbol{L}_\alpha \end{pmatrix}$, this gives us the angular derivatives of both $\boldsymbol{A}$ and $\boldsymbol{L}$. the angular derivatives of $\boldsymbol{Q}$, $\boldsymbol{B}$ and $\boldsymbol{S}$ can now be expressed as follows.

$$\begin{aligned}
\left(\frac{\partial Q}{\partial \theta}\right)_{ij} &= 2i\sum_{\alpha=1}^{3}\left(\frac{\partial A_i^\alpha}{\partial \theta} A_j^\alpha + A_i^\alpha \frac{\partial A_j^\alpha}{\partial \theta}\right) \\
\left(\frac{\partial B}{\partial \theta}\right)_{ij} &= 2i\sum_{\alpha=1}^{3}\left(\frac{\partial L_i^\alpha}{\partial \theta} L_j^\alpha + L_i^\alpha \frac{\partial L_j^\alpha}{\partial \theta}\right) \\
\left(\frac{\partial S}{\partial \theta}\right)_{ij} &= 2i\sum_{\alpha=1}^{3}\left(\frac{\partial A_i^\alpha}{\partial \theta} L_j^\alpha + A_i^\alpha \frac{\partial L_j^\alpha}{\partial \theta}\right)
\end{aligned} \tag{B.7}$$

Also, the angular derivatives of the $\boldsymbol{Q}$, $\boldsymbol{B}$ and $\boldsymbol{S}$ can be expressed in the integral formalism. using the geometry of Figure B.1, we can get

$$\begin{aligned}
\frac{\partial Q_{ij}}{\partial \theta} &= -\frac{1}{2\pi}\int_0^{2\pi} -\left(nn\right)^{-1}_{is}\left[\left(nt\right)_{sk} + \left(tn\right)_{sk}\right]\left(nn\right)^{-1}_{kj} \sin\omega d\omega \\
&= -\frac{1}{2\pi}\int_0^{2\pi} -F_{ij} \sin\omega d\omega
\end{aligned}$$

$$\begin{aligned}
\frac{\partial B_{ij}}{\partial \theta} = \frac{1}{2\pi}\int_0^{2\pi} \Big\{ & \left[\left(mt\right)_{ij} + \left(tm\right)_{ij}\right]\cos\omega + \left(mn\right)_{ir} F_{rk} \left(nm\right)_{kj} \sin\omega \\
& + \left[\left(tn\right)_{ir}\cos\omega - \left(mt\right)_{ir}\sin\omega\right]\left(nn\right)^{-1}_{rk}\left(nm\right)_{kj} \\
& - \left(mn\right)_{ir}\left(nn\right)^{-1}_{rk}\left[\left(tm\right)_{kj}\sin\omega - \left(nt\right)_{kj}\cos\omega\right]\Big\} d\omega
\end{aligned} \tag{B.8}$$

$$\frac{\partial S_{ij}}{\partial \theta} = -\frac{1}{2\pi}\int_0^{2\pi}\Big\{-F_{is}\,(nm)_{sj}\,\sin\omega + (nn)^{-1}_{is}\Big[(tm)_{sj}\,\sin\omega - (nt)_{sj}\,\cos\omega\Big]\Big\}\,d\omega$$

where $F_{ij} = (nn)^{-1}_{is}\Big[(nt)_{sk} + (tn)_{sk}\Big](nn)^{-1}_{kj}$

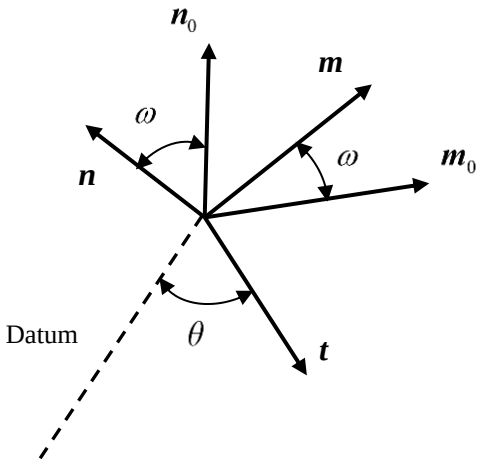


Figure B.1: The geometry used to compute angular derivatives of the line dislocation in a plane whose unit normal is $\boldsymbol{n}_0$

# Appendix C

## Elastic field of infinite dislocation line in isotropic medium

### The edge dislocation

The edge dislocation is characterized by a Burgers vector $\boldsymbol{b} \perp \boldsymbol{\xi}$, where $\xi$ is the direction of straight dislocation. It can be described as due to the insertion of a half infinite slab of thickness *b* perpendicular to the glide plane (Figure C.1).

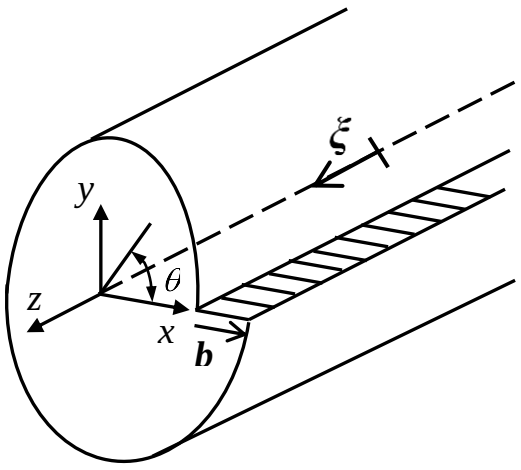


Figure C.1: The coordinate system of edge dislocation. The dislocation line $\xi$ is along *z*-axis and Burger's vector is along *x*-axis

Referred to the coordinate system in Figure C.1, the displacements are

$$u_x = \frac{b}{2\pi}\left[\tan^{-1}\frac{y}{x} + \frac{xy}{2(1-\nu)(x^2+y^2)}\right]$$

$$u_y = -\frac{b}{2\pi}\left[\frac{1-2\nu}{4(1-\nu)}\ln(x^2+y^2) + \frac{x^2-y^2}{4(1-\nu)(x^2+y^2)}\right] \qquad \text{(C.1)}$$

or in cylindrical coordinates

$$u_r = \frac{b}{2\pi}\left[-\frac{1-2\nu}{2(1-\nu)}\sin\theta\,\ln r + \frac{\sin\theta}{4(1-\nu)} + \theta\cos\theta\right]$$

$$u_\theta = \frac{b}{2\pi}\left[-\frac{1-2\nu}{2(1-\nu)}\cos\theta\ln r + \frac{\cos\theta}{4(1-\nu)} - \theta\sin\theta\right] \qquad \text{(C.2)}$$

$u_z = 0$; The edge dislocation is a case of plane strain. In cartesian coordinates, the formulae for the stress components are

$$\sigma_{xx} = -\frac{Gb}{2\pi(1-\nu)}\frac{y(3x^2+y^2)}{(x^2+y^2)^2}$$

$$\sigma_{yy} = \frac{Gb}{2\pi(1-\nu)}\frac{y(x^2-y^2)}{(x^2+y^2)^2}$$

$$\sigma_{xy} = \frac{Gb}{2\pi(1-\nu)}\frac{x(x^2-y^2)}{(x^2+y^2)^2} \qquad \text{(C.3)}$$

$$\sigma_{zz} = \nu(\sigma_{xx}+\sigma_{yy}) = -\frac{Gb\nu}{\pi(1-\nu)}\frac{y}{x^2+y^2}$$

$$\sigma_{xz} = \sigma_{yz} = 0$$

and, in cylindrical coordinates, more simply

$$\sigma_{rr} = \sigma_{\theta\theta} = -\frac{Gb\sin\theta}{2\pi(1-\nu)r}$$

$$\sigma_{r\theta} = \frac{Gb\cos\theta}{2\pi(1-\nu)r} \tag{C.4}$$

$$\sigma_{zz} = \nu(\sigma_{rr} + \sigma_{\theta\theta}) = -\frac{Gb\nu\sin\theta}{\pi(1-\nu)r}$$

$$\sigma_{rz} = \sigma_{\theta z} = 0$$

**The screw dislocation**

A straight dislocation with $\boldsymbol{b} \parallel \boldsymbol{\xi}$ is a screw dislocation, right-handed when $\boldsymbol{b}$ and $\xi$ point in the same direction and left-handed in the opposite case (Figure C.2). For a right-handed screw dislocation along the z-axis in an infinite medium, the displacement is simply

$$u_z = b\frac{\theta}{2\pi} = \frac{b}{2\pi}\tan^{-1}\left(\frac{y}{x}\right) \tag{C.5}$$

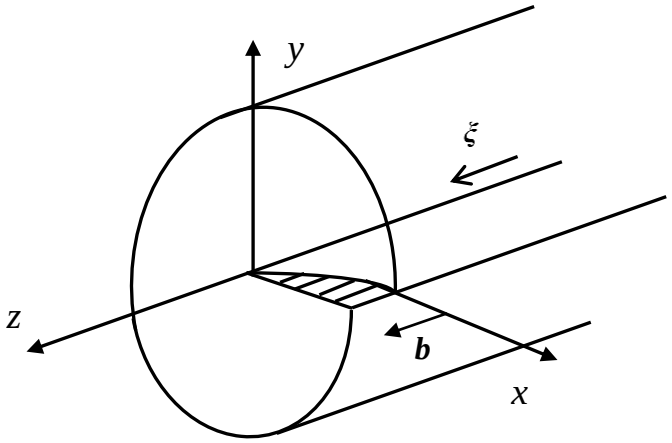


Figure C.2: A right-handed screw dislocation along the axis of a cylinder

when we choose the surface $y = 0$, $x > 0$ as the discontinuity surface. From Eq. (C.5), one obtains the stresses

$$\sigma_{xz} = -\frac{Gb}{2\pi}\frac{y}{x^2 + y^2}$$

$$\sigma_{yz} = \frac{Gb}{2\pi}\frac{x}{x^2 + y^2} \tag{C.6}$$

$$\sigma_{xy} = \sigma_{xx} = \sigma_{yy} = \sigma_{zz} = 0$$

or, in cylindrical coordinates

$$\sigma_{\theta z} = \frac{Gb}{2\pi r}$$

$$\sigma_{rz} = \sigma_{r\theta} = \sigma_{rr} = \sigma_{\theta\theta} = \sigma_{zz} = 0 \tag{C.7}$$

# Appendix D

## Average elastic constants

The most appropriate values of the averaged elastic constants are those averaged over all possible orientations of the coordinate system relative to the crystal axes. The question remains of whether to average over the elastic constants $C_{ijkl}$ or over the elastic compliances $S_{ijkl}$. The former is appropriate for the material in which grains have the same state of strain, as in Figure D.1a and the Voigt averages over $C_{ijkl}$ are applicable; the latter for the case when they have the same stress, as in Figure D.1b and Reuss averages are appropriate.

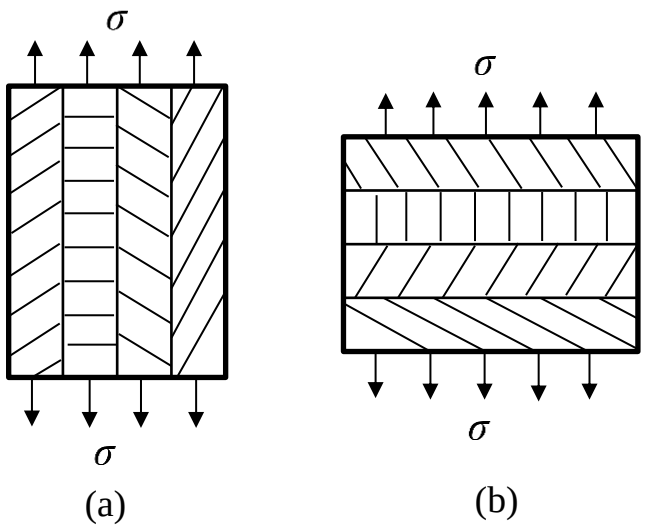


Figure D.1: material under simple tension. (a) Grain boundaries parallel to the tensile axis (uniform strain) (b) Grain boundaries perpendicular to the tensile axis (uniform stress)

**The Voigt Averages**

The 6x6 matrix for the elastic constant $C_{ijkl}$ undergoes an orthogonal unitary transformation when the reference coordinate system is rotated. The trace of a matrix is invariant to this transformation, so that

$$I_1 = C_{ijij} = \text{const} \tag{D.1}$$

A second invariant follows from the invariance of the strain-energy density. For the special case of homogeneous expansion, $\varepsilon_{11} = \varepsilon_{22} = \varepsilon_{33} = \frac{1}{3}\varepsilon_{ii}$ and $\varepsilon_{ij} = 0$ for $i \neq j$, Eq. (2.14) gives

$$I_2 = C_{iijj} = \text{const} \tag{D.2}$$

Especially, we can find that the two invariants for isotropic solid are

$$I_1 = 3\lambda + 12G \tag{D.3}$$

$$I_2 = 9\lambda + 6G \tag{D.4}$$

where $\lambda$ is the Lame Modulus and $G$ is the shear modulus. Incorporate Eq. (D.1) into Eq. (D.3) and Eq. (D.2) into Eq. (D.4) and then solving for the $G$ and $\lambda$ gives the average values

$$G_V = \frac{1}{30}\left(3C_{ijij} - C_{iijj}\right) \qquad \lambda_V = \frac{1}{30}\left(2C_{iijj} - C_{ijij}\right) \tag{D.5}$$

where subscript $v$ indicates the Voigt averages. And averaged Young's modulus and Poisson's ratio can be expressed by these two parameters as

$$E_V = \frac{G_V\left(3\lambda_V + 2G_V\right)}{\lambda_V + G_V} \qquad v_V = \frac{\lambda_V}{2\left(\lambda_V + G_V\right)} \tag{D.6}$$

**The Reuss Averages**

The compliance tensor $S_{ijkl}$ relates strain to the stress as

$$\varepsilon_{ij} = S_{ijkl}\sigma_{kl} \tag{D.7}$$

Thus, the 6x6 compliance matrix $S$ can be written as

$$\begin{Bmatrix} \varepsilon_{11} \\ \varepsilon_{22} \\ \varepsilon_{33} \\ \varepsilon_{23} \\ \varepsilon_{31} \\ \varepsilon_{12} \end{Bmatrix} = \begin{bmatrix} S_{11} & S_{12} & S_{13} & S_{14} & S_{15} & S_{16} \\ S_{21} & S_{22} & S_{23} & S_{24} & S_{25} & S_{26} \\ S_{31} & S_{32} & S_{33} & S_{34} & S_{35} & S_{36} \\ S_{41} & S_{42} & S_{43} & S_{44} & S_{45} & S_{46} \\ S_{51} & S_{52} & S_{53} & S_{54} & S_{55} & S_{56} \\ S_{61} & S_{62} & S_{63} & S_{64} & S_{65} & S_{66} \end{bmatrix} \begin{Bmatrix} \sigma_{11} \\ \sigma_{22} \\ \sigma_{33} \\ 2\sigma_{23} \\ 2\sigma_{31} \\ 2\sigma_{12} \end{Bmatrix} \tag{D.8}$$

In analogy to Eq, (D.1), the trace of $S$ is invariant and in analogy to Eq. (D.2), a second invariant is found by considering the invariance of strain energy under the case of stress $\sigma_{11} = \sigma_{22} = \sigma_{33} = \frac{1}{3}\sigma_{ii}$ and $\sigma_{ij} = 0$ for $i \neq j$, giving

$$I_1 = S_{ijij} = \text{const} \tag{D.9}$$

$$I_2 = S_{iijj} = \text{const} \tag{D.10}$$

The averaged Young's modulus and Poisson' ratio can be expressed by these two invariances as

$$\frac{1}{E_R} = \frac{1}{15}\left(2S_{ijij} + S_{iijj}\right), \qquad \frac{\nu_R}{E_R} = \frac{1}{15}\left(S_{ijij} - 2S_{iijj}\right) \tag{D.11}$$

where the subscript $R$ indicates the Reuss averages